TECHNISCHE UNIVERSITÄT MÜNCHEN
Lehrstuhl für experimentelle Halbleiterphysik E25
Walter Schottky Institut

Broadband electrically detected magnetic resonance using adiabatic and optimal control pulses

Florian Martin Hrubesch

Vollständiger Abdruck der von der Fakultät für Physik der Technischen Universität München zur Erlangung des akademischen Grades eines

Doktors der Naturwissenschaften

genehmigten Dissertation.

Vorsitzender: Prof. Dr. Frank Pollman

Prüfer der Dissertation:
1. apl. Prof. Dr. Martin S. Brandt
2. Priv.-Doz. Dr. Hans-Gregor Hübl

Die Dissertation wurde am 28.03.2018 bei der Technischen Universität München eingereicht und durch die Fakultät für Physik am 17.07.2018 angenommen.

Zusammenfassung

Die elektrisch detektierte magnetische Resonanz (EDMR) ist eine vielseitige Messmethode, welche es erlaubt, den Ladungsträgertransport in organischen und anorganischen Halbleitern zu untersuchen. Durch ihre hohe Sensitivität eignet sie sich besonders für die Charakterisierung von dünnen Schichten, die in herkömmlichen Spinresonanzmessungen nicht genug Signal-zu-Rausch-Abstand aufweisen. Durch die hohe Empfindlichkeit zur Untersuchung dünner Schichten ist es möglich, neben den in der Magnetresonanz gebräuchlichen Hohlraum- und dielektrischen Resonatoren planare Strukturen für die Anregung der Spinresonanz zu verwenden.

Solche Strukturen können entweder planare Resonatoren oder ebenfalls planare, breitbandige Mikrowellenleiter sein, welche über einen weiten Frequenzbereich funktionieren. Beide erlauben aufgrund ihrer Dimensionen die Erzeugung von Mikrowellenfeldern, die die Intensität der Felder in einem herkömmlichen Mikrowellenresonator bei weitem übersteigen. Zusätzlich bieten breitbandige Strukturen den Vorzug, dass die Mikrowellenfrequenz und damit die in der Messung verwendeten Magnetfelder frei gewählt werden können. Durch geschickte Wahl der Frequenz, beziehungsweise des Resonanzmagnetfeldes, ist es möglich, überlappende Resonanzen zu trennen, falls sich deren g-Faktoren unterscheiden und sie deswegen eine abweichende Skalierung mit dem externen Magnetfeld aufweisen.

Allerdings haben planare Strukturen nicht nur Vorteile. So ist die Homogenität des von den planaren Strukturen erzeugten Mikrowellenmagnetfeldes deutlich schlechter als von herkömmlichen Mikrowellenresonatoren, was sich auf die Qualität der durch die Mikrowellenpulse induzierten Spinrotationen auswirkt. Je nach

Homogenität des Feldes weisen bereits nominelle Rotationen um 180° eine so breite Verteilung der effektiven Drehwinkel innerhalb des studierten Spin-Ensembles auf, dass der Kontrast des Experiments auf wenige Prozent einbricht.

Aus der Kernspinresonanz sind adiabatische und numerisch optimierte Pulse (sog. optimal control-Pulse, kurz oc-Pulse) bekannt, die Inhomogenitäten des dort verwendeten Radiofrequenzmagnetfeldes kompensieren. Entsprechend optimierte Mikrowellenpulse sollten es somit ermöglichen, mit planare Mikrowellenstrukturen trotz ihrer Inhomogenität Experimente mit hohen Drehwinkeln und gleichzeitig hohen Fidelitäten durchzuführen. Um adiabatische und oc-Pulse für die EDMR einsetzen zu können, wurde zunächst ein Messaufbau konstruiert, der es erlaubt, diese beiden Pulstypen sowohl für Mikrowellen- als auch Radiofrequenzpulse zu verwenden. Dieser Aufbau gestattet die Durchführung breitbandiger EDMR-Experimente (2 GHz bis 18 GHz) und elektrisch detektierte Kernspinresonanzexperimente für Radiofrequenzen um 4 MHz unter Verwendung dieser adiabatischen und oc-Pulse. Dabei verbessern diese Pulse die Signalintensität um das bis zu 1,7-Fache für Proben, die eine hohe Mikrowellenmagnetfeldinhomogenität aufweisen. Im Fall einer niedrigeren Inhomogenität zeigt sich die Überlegenheit dieser Pulse bei Experimenten mit hohen Drehwinkeln oder mit komplizierteren Pulssequenzen, wie zum Beispiel dem Hahn-Echo. In dieser Arbeit konnte durch die Anwendung von oc-Pulsen eine um 38 % höhere Signalintensität erreicht werden.

Diese Verbesserungen ermöglichen die Modifikation des Messaufbaus für ortsabhängige EDMR-Experimente, wobei sowohl die Anregung der Spinresonanz als auch die Erzeugung des nötigen Feldgradienten über die planaren Mikrowellenstrukturen erfolgt. Mit für die EDMR typischen Proben wird eine probenabhängige Auflösung von 1.5 µm erreicht. Dies erlaubt es die grundlegenden physikalischen Prozesse in der verwendeten Metall-Halbleiter-Metall Struktur nachzuvollziehen und darauf aufbauend Hinweise für die Optimierung der Kontaktstruktur für EDMR Messungen abzugeben. Basierend auf der erreichten Auflösung wird gezeigt, wie ortsaufgelöste EDMR für die Messung der Elektronenwellenfunktion von Phosphor-Donatorelektronen in Silizium mit einer Auflösung von 0.5 Å verwendet werden könnte.

In einem kurzen Exkurs wird die elektrische Detektion des Stickstoff-Fehlzellen-Komplexes (NV) in Diamant untersucht. Hier ist es uns möglich, die elektrische Detektion mit der kohärenten Manipulation des NV-Spins zu kombinieren und an kleinen Ensemblen zu demonstrieren. Mit Hilfe einer Monte-Carlo-Simulation wird gezeigt, dass diese Methode mindestens die Sensitivität der bisher üblichen optischen Detektionsmethoden erreicht und damit die elektrische Detektion eines einzelnen NV-Spins ermöglichen sollte. Damit stellt die elektrische Detektion einen vollwertigen Ersatz der optischen Detektion dar. Dies sollte den Bau kompakter NV-basierter Messgeräte ermöglichen, die nicht auf komplexe konfokale Messmethoden zurückgreifen müssen.

Contents

1

Introduction

Electrically detected magnetic resonance (EDMR) [1] is a versatile method to characterize point defects and charge transport in inorganic and organic semiconductors [2–9]. Due to its high sensitivity it allows for the detection of ensembles with as few as 50 spins in spin-pair-based readout processes [10] and of single electron or nuclear spins when single electron transistors are used for readout [11]. The prototype spin pair investigated in the present work is formed by an unsaturated paramagnetic silicon dangling bond at the Si/SiO_2 interface between Si and its native surface oxide together with a ^{31}P donor electron in close vicinity to the interface [3]. The characteristic signature of the dangling bond spin is the P_{b0} center with an anisotropic g-factor of $g_{\|} = 2.0018$ and $g_{\perp} = 2.0081$ [12]. The g-factor of the phosphorus donor is $g_{\mathrm{e}} = 1.9985$ with a hyperfine interaction with the ^{31}P nucleus of $A = 117.53\,\mathrm{MHz}$ and a nuclear g-factor $g_{\mathrm{n}} = 2.2601$ [13]. This leads to an overlap of one of the hyperfine-split phosphorus resonances and the dangling bond resonances at X-band frequencies which hampers experiments performed on these resonances.

The use of broadband microwave delivery structures can mitigate e.g. the problems caused by this overlap and allows for multi-frequency or frequency-swept spin resonance experiments which

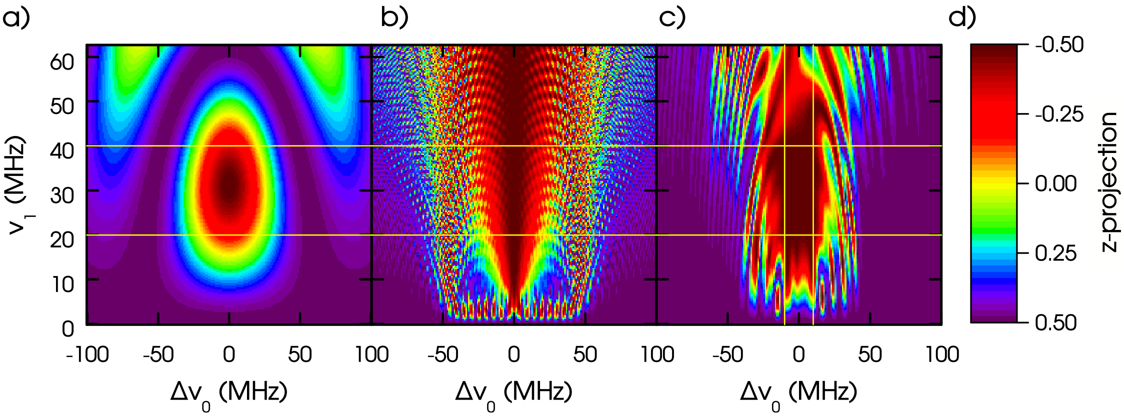

Figure 1.1: Spin projection onto the z-axis as a function of the off-resonance $\Delta\nu_0$ and the Rabi frequency ν_1 for a rectangular pulse (panel a)), an adiabatic pulse (panel b)) and an optimal control pulse (panel c)) for a single spin 1/2. The horizontal yellow lines mark the variation in ν_1 acting on a spin ensemble under a microwave stripline. The vertical yellow lines depict the optimization goal of the optimal control pulse in $\Delta\nu_0$. d) Color code of the z-projection.

would otherwise require the use of several resonators and multiple cool-down cycles. Broadband microwave striplines have been used successfully for continuous wave (cw) EDMR experiments [14–16] and for pulsed experiments on single spin devices [17, 18]. However, in contrast to resonator-based EDMR experiments these structures exhibit significant inhomogeneities of the microwave magnetic field B_1, which are relevant for pulsed EDMR (pEDMR) experiments on ensembles as can be seen in the effect of a rectangular 16-ns-long microwave π-pulse on a single spin 1/2. Figure 1.1 a) plots the spin projection onto the z-axis after such a pulse as a function of its off-resonance $\Delta\nu_0$ and its Rabi frequency ν_1. Here, the yellow horizontal lines mark the variation in ν_1 acting on an ensemble under a typical microwave antenna used during this work. Especially at the borders of this variation the fidelity of the pulse is significantly reduced. This situation quickly deteriorates if more than one pulse is used in an experiment.

Nuclear magnetic resonance (NMR) experiments with surface coils [19–22] and recent experiments on superconducting coplanar waveguide resonators [23], to name but a few, have demonstrated the capability of adiabatic pulses to correct such B_1-inhomogeneities. Figure 1.1 b) depicts the spin projection onto the z-axis after an adiabatic BIR-4 π-pulse [22]. Compared to the rectangular pulse, this pulse has a huge region along the ν_1-axis in which it shows a good fidelity, but this improvement is the result of a very significant increase of the length of the pulse. It has a pulse length of 1.6 µs, which is longer than the 16-ns-long rectangular pulse by a factor of 100. Depending on the lifetime of the particular spin ensemble, this may or may not be a problem. In the case of the spin pair used in this work, it is already too long, since the coherence time T_2 of the ^{31}P ensemble is on the order of 10 µs when the illumination is switched off [24], which means that, independent of the fidelity of the pulses, the signal has decayed to $1/e$ already after about six pulses.

Optimal control pulses [25–41], which are basically pulse sequences formed by concatenating rectangular pulses with varying amplitude and phase, can improve this situation by limiting the optimization region to the particular linewidth and Rabi frequency distribution of the ensemble (horizontal and vertical yellow lines in figure 1.1 c)). The resulting optimized pulses are much shorter (pulse length in this example: 300 ns) than adiabatic pulses and show a very good fidelity across the optimization region (c.f. figure 1.1 c)). Apart from this, optimal control pulses can also be tweaked to perform operations at very high control fields B_1, which is difficult with conventional microwave pulses, due to the break-down of the rotating wave approximation [38], or to enforce a specific spin movement, e.g. as if unwanted spin-spin interactions are switched off [30].

To gain access to these pulses and the wealth of applications which they offer, we designed a broadband microwave setup with the ability to use arbitrarily shaped microwave and radio frequency pulses and tested both adiabatic and optimal control pulses for the use in pulsed EDMR experiments. We show that our setup and the broadband antennas designed for it work as intended over the desired microwave frequency range from 2 GHz to 18 GHz and for typical NMR frequencies at a few megahertz. We are able to generate adiabatic and optimal control pulses and successfully implement them in more complicated pulse sequences like those used in electron nuclear double resonance measurements (ENDOR). These pulses improve the signal intensity in our experiments by a factor of up to 1.7 for samples with a high B_1-inhomogeneity. For samples with lower B_1-inhomogeneity the advantages of optimal control pulses come into play for large rotation angles, e.g. 16π. We find that they provide an up to 25 % better signal than adiabatic pulses long after the signal generated by rectangular pulses has completely decayed.

We then use these optimal pulses and a slightly modified broadband antenna to implement position-dependent EDMR measurements, which allow us to pinpoint the source of the EDMR signal in the investigated devices with an accuracy of at least 1.5 µm. Using this information, we suggest optimizations to the finger structure, which is currently used in EDMR experiments for the electrical contacts, and estimate the maximal possible resolution for position-dependent EDMR measurements.

In a small digression, we finally look into the electrical read-out of the NV^- center in diamond and expand the method of electrical read-out to coherent pulsed microwave excitation on ensembles as small as 130 spins. Using a Monte-Carlo simulation we show that single spin read-out should be possible with at least the sensitivity of the optical detection which is normally used.

This thesis is structured as follows. In chapter 2 we discuss the theoretical basics of the time-dependent evolution of spin states, our read-out process, the pulse sequences used in our experiments, the principles of magnetic resonance imaging and adiabatic and optimal control pulses. We introduce our setup in chapter 3. The discussion includes the design of the microwave hardware, a short overview of the stripline structures and the calibration of the setup. We demonstrate in chapter 4 that the constructed spectrometer works as intended over the microwave frequency range from 2 GHz to 18 GHz and for radio frequency pulses, before we turn to the comparison of rectangular, adiabatic and optimal control pulses in chapter 5. Afterwards, we use these pulses for magnetic resonance imaging experiments (chapter 6). We compare the performance of rectangular and optimal control echoes for imaging, determine the spatial resolution of our setup and estimate the maximal resolution possible with such an imaging setup. Finally, in chapter 7, we explore the electrical read-out of NV^- centers in diamond and summarize this thesis in chapter 8.

2

Electrically detected magnetic resonance in a nutshell

In this chapter we discuss the theoretical basis of electrically detected magnetic resonance (EDMR) measurements. Section 2.1 introduces the spin Hamiltonian and the spin-dependent recombination mechanism. Afterwards, section 2.2 deals with the description of the evolution of the spin state on the Bloch sphere in the lab and in the rotating frame. We employ this picture to describe the effects of the pulse sequences primarily utilized in this work (section 2.3) before we apply the Hahn echo sequence (section 2.3.3) to magnetic resonance imaging (section 2.4). Finally, we introduce the concepts behind adiabatic and optimal control pulses, and how they improve the fidelity of each pulse in a sequence (section 2.5).

2.1 EDMR on the ^{31}P-Pb_0 spin pair

EDMR employs a spin-dependent recombination mechanism to detect the microwave-induced transitions between two Zeeman-split energy levels of a spin in an external magnetic field. If the incident microwave radiation meets the resonance condition, a photon changes the state of the spin and the spin-dependent recombination leads to a quenching of the current through the semiconductor. This change is detected e.g. by a fast analog-to-digital converter. For the phosphorus donors in silicon which are studied in this work, the energy levels corresponding to its spin Hamiltonian in an external magnetic field are discussed in section 2.1.1. Afterwards, we treat the spin-dependent recombination mechanism used in this work in more detail (section 2.1.2).

2.1.1 Phosphorus donor spin Hamiltonian

Following reference 42 the spin Hamiltonian that describes phosphorus donors in silicon subjected to an external magnetic field $\vec{B}_0 = B_0\vec{e}_z$ is

$$\mathcal{H} = g_{\mathrm{e}}\mu_{\mathrm{e}}S_zB_0 - g_n\mu_nI_zB_0 + A\vec{S}\cdot\vec{I}. \tag{2.1}$$

The first two terms are caused by the Zeeman interaction of the electron spin $\vec{S}$ and the nuclear spin $\vec{I}$ with the external magnetic field $\vec{B}_0$. Their respective g-factors and the electron or nuclear magnetons are $g_{\mathrm{e}} = 1.9985$ [13], $g_{\mathrm{n}} = 2.2632$ [43], $\mu_{\mathrm{e}} = 9.274 \cdot 10^{-24}\,\mathrm{J\,T^{-1}}$ and $\mu_{\mathrm{n}} = 5.0508 \cdot 10^{-27}\,\mathrm{J\,T^{-1}}$. In the third term the Fermi contact interaction is represented by the isotropic hyperfine constant $\frac{A}{\hbar} = 117.5\,\mathrm{MHz}$ [44]. In this description, the weak interaction between the phosphorus donor electron spin and the readout partner of the spin pair (coupling strength between 25 kHz and 3 MHz [45]) as well as the weak interaction of the electron spin with the ^{29}Si spin bath (coupling strength smaller than 4 MHz [13, 46]) are neglected. Due to the random distribution of coupling strengths in these two cases, which are caused by the random distribution of distances between the donor and both dangling bond electron as well as ^{29}Si nuclear spins, their contribution results in a broadening of the phosphorus donor resonance.

To solve the Hamiltonian 2.1, it is written in the product basis of the electron and the nuclear spins $|s, m_s, i, m_i\rangle = |s, m_s\rangle \times |i, m_i\rangle$ and the eigenstates $\left|E_j\right\rangle$ with their corresponding eigenvalues E_j are calculated. Here, s and i are the spin quantum numbers for the electron and the nuclear spin, respectively. m_s and m_i are the

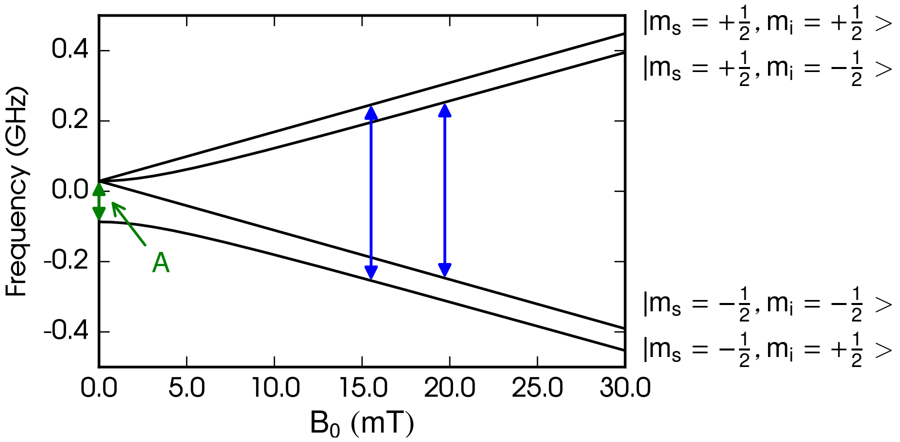

Figure 2.1: Numerically calculated eigenenergies (in frequency units) as a function of the external magnetic field B_0. The allowed electron spin-flip transitions are depicted by two blue arrows and the green arrow represents the zero-field splitting A. On the right hand side the eigenenergies are labeled with the corresponding eigenstates in the high field limit.

corresponding secondary spin quantum numbers. In general, the eigenstates are a mixture between the different basis vectors

$$\left|E_j\right\rangle = \sum_{m_s=-s}^{s} \sum_{m_i=-i}^{i} c^j_{m_s,m_i} |s, m_s\rangle \times |i, m_i\rangle \tag{2.2}$$

with the mixing constant $c^j_{m_s,m_i}$. Figure 2.1 plots the numerically calculated eigenenergies (in frequency units) as a function of the external magnetic field B_0. The two allowed electron spin-flip transitions ($\Delta m_s = \pm 1$) are depicted by the two blue arrows. For low magnetic fields, the eigenstates split into a triplet state and a singlet state which are separated in energy by A (green arrow). In the limit of high magnetic fields, when the energy due to the Zeeman interaction is much greater than the energy due to the hyperfine interaction, the eigenstates are approximately equal to the basis states as indicated by the labels on the right of figure 2.1. This is true for the microwave frequencies which our setup generates (2 GHz to 18 GHz) and allows us to treat the evolution of the electron spin state independently from the evolution of the nuclear spin.

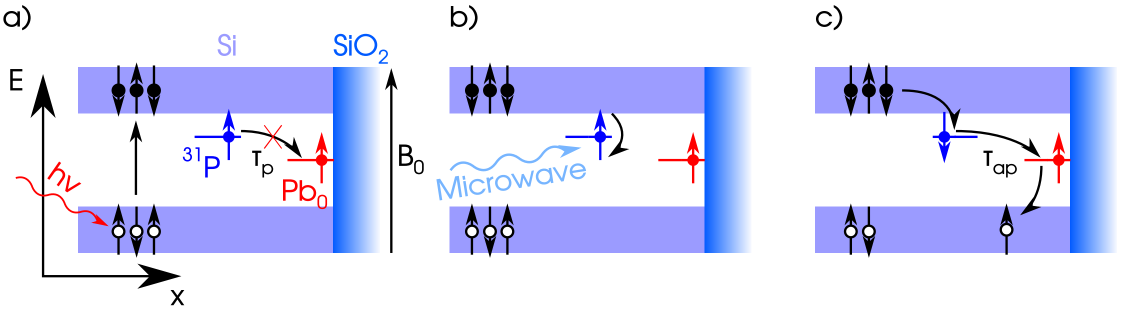

Figure 2.2: Position space band structure of phosphorus-doped silicon close to the silicon-dioxide-covered surface. The phosphorus and dangling bond states are colored blue and red, respectively. a) Above band gap illumination (red arrow) excites valence band electrons into the conduction band. If the phosphorus-dangling bond spin pair is in a parallel configuration, the phosphorus electron is forbidden to enter the dangling bond due to the Pauli principle until a (random) spin flip happens. This configuration has a lifetime of τ_p. b) Resonant microwave irradiation (turquoise arrow) lifts the Pauli blockade. c) Phosphorus-dangling bond spin pair in an antiparallel configuration. This state decays on a timescale of τ_{ap} after which the empty phosphorus state catches an electron from the conduction band and the dangling bond state catches a hole from the valence band.

2.1.2 Spin-dependent recombination

The spin-dependent recombination used in this work employs the spin pair formed by a phosphorus electron spin in the vicinity of a dangling bond at the surface. The spin pair is sketched in the band structure in figure 2.2. If it is in a parallel spin configuration, recombination of the electron from the donor to the dangling bond is Pauli forbidden and can only take place after the spin is flipped. This leads to two distinct rates for the transition of the electron from the phosphorus to the dangling bond because a random spin flip has to precede the recombination for parallel spin pairs. These rates are $1/\tau_\mathrm{ap}$ and $1/\tau_\mathrm{p}$ for spin pairs in an antiparallel and a parallel configuration, respectively [5] and we will call τ_ap and τ_p the antiparallel and parallel recombination times from here on. Using resonant microwave (MW) excitation the Pauli blockade can be lifted by flipping one of the spins involved (c.f. figure 2.2 b)) which leads to increased recombination (c.f. figure 2.2 c)) and a quenching of the (photo-)current through the sample which in turn can be detected electrically.

In order to achieve a good signal-to-noise ratio, the temperature T should be below 12 K [47]. At this temperature, the timescale for random phosphorus donor electron spin flips approaches microseconds [48] which is close to the antiparallel recombination time $\tau_{\mathrm{ap}} = 16\,\mu\mathrm{s}$ [5] in our samples. This diminishes the difference between τ_{ap} and τ_{p}, which we use for the EDMR detection and consequently reduces the signal intensity until the signal is virtually gone at $T = 18\,\mathrm{K}$ [47]. To measure a current at these temperatures it is necessary to illuminate the sample with above band gap light to generate electrons and holes in the conduction and the valence band, respectively (c.f. figure 2.2 a)). During illumination, electrons from the conduction band enter empty phosphorus donor states. Depending on the state of the spin pair the donor electron will either recombine on a time scale of τ_{ap} for antiparallel spins or live for a time of about $\tau_{\mathrm{p}} = 1\,\mathrm{ms}$ ($T = 5\,\mathrm{K}$) [5]. This difference in recombination times leads to spin pairs predominantly in the parallel state after a time of 400 µs [5] for the typically used illumination powers. This sets the minimal illumination time to initialize the spin pairs.

In the case of constant illumination a resonant ESR pulse transforms the parallel spin pair into an antiparallel one, which recombines on the timescale of 16 µs and the empty donors refill from the conduction band. The resulting current transient is then proportional to the spin state after the pulse [49].

For pulsed illumination, dark-times T_{dark} of suitable length ($\tau_{\mathrm{p}} \gg T_{\mathrm{dark}} \geq 3\tau_{\mathrm{ap}}$) are inserted after the light pulse and the microwave pulse, respectively. This is illustrated in figure 2.3 a), where light pulses are colored red and microwave pulses are depicted by a black square. After the first light pulse, which initializes the spin pairs, all remaining antiparallel spin pairs (figure 2.3 c)) recombine ($T_{\mathrm{dark}} \geq 3\tau_{\mathrm{ap}}$) and all electrons in the conduction band decay into the valence band. Due to the much longer lifetime of parallel spin pairs $\tau_{\mathrm{p}} \gg T_{\mathrm{dark}}$ (figure 2.3 b)) most of the parallel spin pairs remain intact. A microwave pulse then transforms those remaining parallel spin pairs. During the following waiting time T_{dark}, all the spin pairs which became antiparallel after the microwave pulse, will recombine.

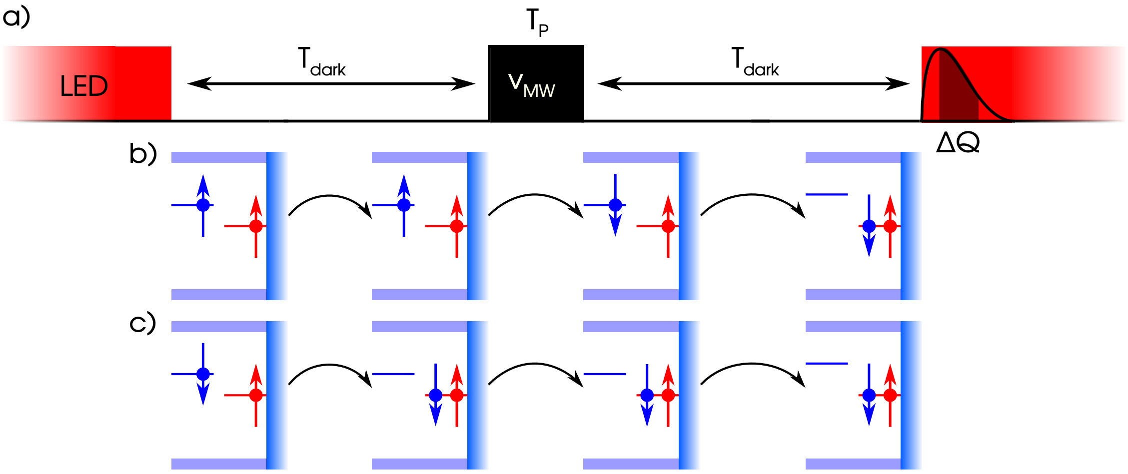

Figure 2.3: a) Basic EDMR pulse sequence using pulsed light illumination. LED pulses are colored red and (rectangular) microwave pulses are depicted by the black rectangle. The pictogram at the beginning of the second light pulse illustrates the current transient due to the light pulse. Panel b) shows the temporal development of spin pairs with parallel spins after the first light pulse, panel c) that of antiparallel pairs.

Since there are no electrons left in the conduction band, ionized states will not be refilled. This results in ionized donors proportional to the amount of antiparallel spin pairs after the first light pulse and after the ESR pulse. During the readout light pulse, these empty states are filled with conduction band electrons resulting in the desired quenching of the current through the sample. This slightly changes the current transient due to the light pulse, which is depicted in the pictogram at the beginning of the second light pulse.

Irrespective of the method of illumination, the EDMR signal ΔQ is extracted from the current transient through boxcar integration over this transient.

2.2 The rotating frame

The time evolution of any quantum object is governed by the time-dependent Schrödinger equation [50]. However, to describe the

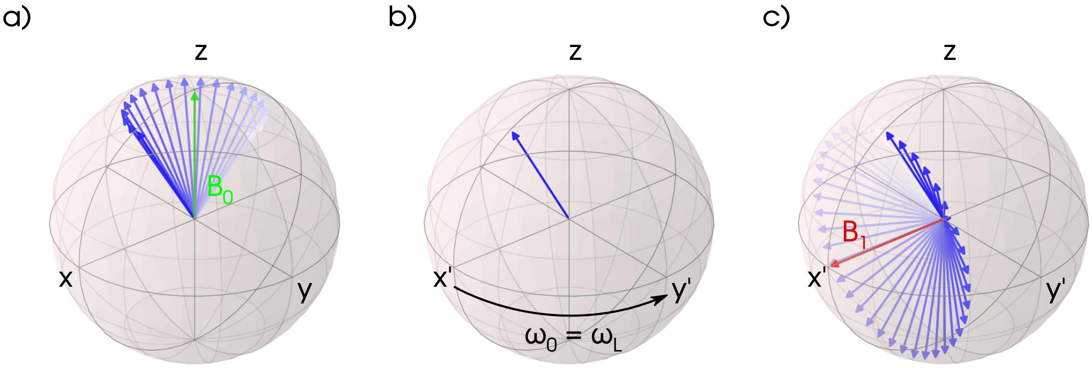

Figure 2.4: a) Magnetization (blue arrow) precessing around $\vec{B}_0$ (green arrow) on the Bloch sphere. b) Magnetization (blue arrow) in a rotating frame which rotates with the Larmor frequency of the spin ($\omega_0 = \omega_L$). c) Magnetization (blue arrow) precessing around a resonant $\vec{B}_1$ (red arrow) in the rotating frame.

behavior of an ensemble of spins, the Bloch equations [51], which describe the motion of the magnetization $\vec{M}$ caused by the magnetic moments $\vec{\mu}$ of the spins in the ensemble in a classical picture, can be used, too.

In this section, we give a brief introduction to the motion of $\vec{M}$ caused by constant and oscillatory magnetic fields which is visualized on the Bloch sphere. The north pole of the Bloch sphere represents the state spin up or a magnetization parallel to the external field while the south pole describes the state spin down or a magnetization antiparallel to the field. Magnetizations in the x-y-plane or coherent superpositions of the spin states up and down lie on the x-y-plane of the Bloch sphere.

The Bloch equation to describe the spin movement in vector notation as first written down in reference 51 is

$$\frac{\mathrm{d}\vec{M}}{\mathrm{d}t} = \gamma \vec{M} \times \vec{B} - \frac{M_x \vec{e}_x + M_y \vec{e}_y}{T_2} + \frac{(M_0 - M_z)\,\vec{e}_z}{T_1}. \tag{2.3}$$

In this equation $\gamma = \frac{g\mu_e}{\hbar}$ is the gyromagnetic ratio of the spin, where $\vec{B}$ is the time-dependent three-dimensional external magnetic field, M_0 is the equilibrium magnetization along z and the decay times T_2 and T_1 describe the decay of the magnetization in the x-y-plane and along $\vec{e}_z$, respectively.

For the following treatment we will ignore the decay terms. A constant magnetic field $\vec{B}_0 = B_0\vec{e}_z$ results in

$$\frac{\mathrm{d}}{\mathrm{d}t}\begin{pmatrix} M_x \\ M_y \\ M_z \end{pmatrix} = \gamma B_0 \begin{pmatrix} M_y \\ -M_x \\ 0 \end{pmatrix}. \tag{2.4}$$

This describes a precession around the z-axis with a rotation frequency of $\omega_\mathrm{L} = \gamma B_0$ which is also called the Larmor frequency of the spin (c.f. figure 2.4 a)). To simplify the mathematical treatment of more complex time-dependent magnetic fields, we change the reference frame from the laboratory frame (denoted by x, y and z) to a rotating frame (denoted by x', y' and z') which rotates with a frequency ω_0 around $\vec{e}_z$, so that

$$\vec{e}_{x'} = \cos(\omega_0 t)\,\vec{e}_x + \sin(\omega_0 t)\,\vec{e}_y, \tag{2.5}$$

$$\vec{e}_{y'} = -\sin(\omega_0 t)\,\vec{e}_x + \cos(\omega_0 t)\,\vec{e}_y \tag{2.6}$$

$$\text{and} \quad \vec{e}_{z'} = \vec{e}_z. \tag{2.7}$$

The movement of $\vec{M}$ in the rotating frame is then described by [52]

$$\left(\frac{\mathrm{d}\vec{M}}{\mathrm{d}t}\right)_\mathrm{rot} = \left(\frac{\mathrm{d}\vec{M}}{\mathrm{d}t}\right)_\mathrm{lab} - \vec{M}\times\vec{\Omega}, \tag{2.8}$$

with $\vec{\Omega} = \omega_0\vec{e}_z$. In the case of the static magnetic field this yields

$$\left(\frac{\mathrm{d}\vec{M}}{\mathrm{d}t}\right)_\mathrm{rot} = (\omega_\mathrm{L} - \omega_0)\cdot\left(\vec{M}\times\vec{e}_z\right), \tag{2.9}$$

which results in a constant magnetization $\vec{M}_\mathrm{rot}$ in the rotating frame if $\omega_\mathrm{L} = \omega_0$ (c.f. figure 2.4 b)). If the rotating frame does not match the Larmor frequency, the movement of the spin in the rotating frame appears to be due to a reduced magnetic field $\frac{\Delta\omega}{\gamma}$ along $\vec{e}_z$ which can be seen by rewriting equation 2.9 as

$$\left(\frac{\mathrm{d}\vec{M}}{\mathrm{d}t}\right)_\mathrm{rot} = \gamma\vec{M}\times\left(\frac{\Delta\omega}{\gamma}\vec{e}_z\right) \tag{2.10}$$

with $\Delta\omega = \omega_\mathrm{L} - \omega_0$. In the rotating frame, a constant magnetic field $\vec{B}_1$ in the x'-y'-plane leads to a precession in the same way as the magnetization precesses around the external magnetic field in the laboratory frame (c.f. figure 2.4 c)). The precession frequency or Rabi frequency therefore is $\omega_\mathrm{R} = \gamma B_1$ and a certain rotation angle Θ is achieved by turning on this field for a specific time T_P. The resulting angle for resonant spins is calculated through

$$\Theta = \int\limits_{t=0}^{T_\mathrm{p}} \omega_\mathrm{R}\left(t\right) \mathrm{d}t. \tag{2.11}$$

In the laboratory frame, this magnetic field corresponds to a circularly polarized oscillating magnetic field which follows directly from applying the three-dimensional rotation matrix (e.g. [53])

$$\left(\vec{B}_1\right)_\mathrm{lab} = B_1 \left(\cos\left(\omega_0 t + \varphi\right)\vec{e}_x + \sin\left(\omega_0 t + \varphi\right)\vec{e}_y\right). \tag{2.12}$$

A change in the phase φ of this oscillating magnetic field is equal to a rotation of $\vec{B}_1$ in the rotating frame and therefore allows to set the angle of $\vec{B}_1$ in the x'-y'-plane.

Finally, apart from a few experiments [54–56], the microwaves, which are used for spin resonance experiments, are typically linearly polarized. Since every linearly polarized wave can be expressed by two circularly polarized waves this leads to one component which can be expressed as in equation 2.12 and one component with the opposite rotation direction (counter-rotating). This component rotates with two times ω_0 in the rotating frame. If the precession frequency of $\vec{M}$ due to this field is small compared to ω_0, small changes caused by this rotating field will be reversed when the direction of the field is inverted after a π-rotation and the counter-rotating field can be neglected (rotating wave approximation). For large $\vec{B}_1$-amplitudes, this no longer holds true and the effects of the counter-rotating field have to be considered [57].

2.3 Pulse sequences

Through changes in the amplitude, phase and length of a microwave pulse spin rotations can reach any point on the Bloch sphere. By using a combination of different pulses, it is possible to measure

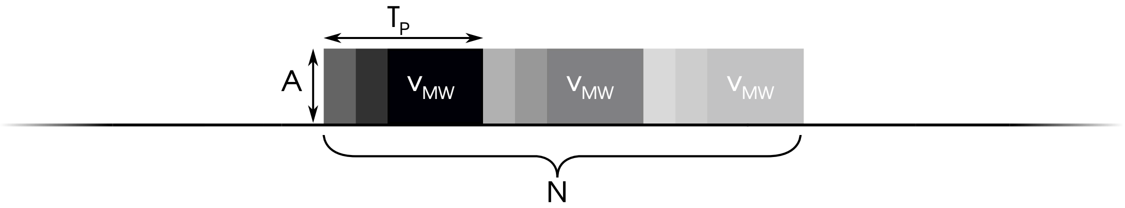

Figure 2.5: Basic pulse sequence, where either the pulse frequency ν_{MW}, the pulse length T_{P}, the pulse amplitude A or the number of pulse repetitions N is changed during an experiment. The lightness differences of the pulse depict either a changing pulse length or the varying number of repetitions.

the intrinsic width of a resonance [58], the lifetime of a spin state [47], the coupling between different spin species [45] and many more properties of the spin system at hand.

In this section we give a brief overview over the sequences which are employed most frequently in this thesis, namely the sequence utilized for Rabi oscillation measurements and magnetic field sweeps (section 2.3.1), the Ramsey sequence (section 2.3.2) and the Hahn echo sequence (section 2.3.3). All sequences in this section can be used with and without pulsed illumination. Since the only difference between sequences using pulsed and continuous illumination is the addition of light pulses and the shift of the current detection from following the final microwave pulse to following the readout light pulse we concentrate on the spin evolution and ignore the light pulsing scheme to simplify the discussion.

2.3.1 Basic pulse sequence

The basic pulse sequence is composed of only one microwave pulse of which either the pulse frequency ν_{MW} (or the static magnetic field B_0), the pulse length T_{P}, the pulse amplitude A or the number of times the pulse is repeated N (which corresponds to the total length of all microwave pulses) is changed during an experiment. This sequence is employed for magnetic field (c.f. section 4.1) and frequency sweeps (c.f. section 5.1) to measure the ESR spectrum of a given sample and for pulse length sweeps to obtain Rabi oscillations (c.f. sections 4.2, 5.1 and 6). Figure 2.5 plots this sequence.

There exist at least four different ways to implement a lock-in procedure [59] to increase the signal-to-noise-ratio with this sequence.

Firstly, the microwave pulse can be switched off during every other sequence (amplitude cycling) so that subtracting the transients of the different sequences yields the difference between the effect of the pulse and the unmanipulated system.

Secondly, by shifting the pulse frequency to a far off-resonant frequency for every other sequence (frequency cycling), the same effect is achieved. This has the advantage that heating effects during both sequences are roughly the same, but effects due to microwave crosstalk might not be filtered out completely because they may depend on the microwave frequency.

Thirdly, instead of shifting the frequency a shift of the external magnetic field in every other sequence (e.g. with the help of modulation coils) also achieves that the microwave pulse is or is not in resonance [60]. This procedure is able to filter out possible microwave crosstalk, but might be influenced by induction effects from the magnetic field modulation. This approach was not tested in this work.

Lastly, the rotation angle of some pulses (e.g. BIR-4, c.f. section 2.5.1.2) can be switched by changing e.g. the phase φ during the pulse. A lock-in method based on such pulses is able to effectively filter the microwave-induced crosstalk, does not suffer from induction and is therefore employed whenever possible.

Apart from that, lock-in methods based on amplitude or frequency cycling work satisfactorily if pulsed illumination is used, because the readout is separated in time from the microwave pulse. This is not true for continuous illumination where the crosstalk severely changes the current transient and only phase cycling methods yield adequate results.

2.3.2 Ramsey pulse sequence

The Ramsey sequence is the EDMR equivalent to the measurement of a free induction decay (FID) in NMR and ESR [58]. It can be employed to measure the dephasing time T_2^* due to interactions both

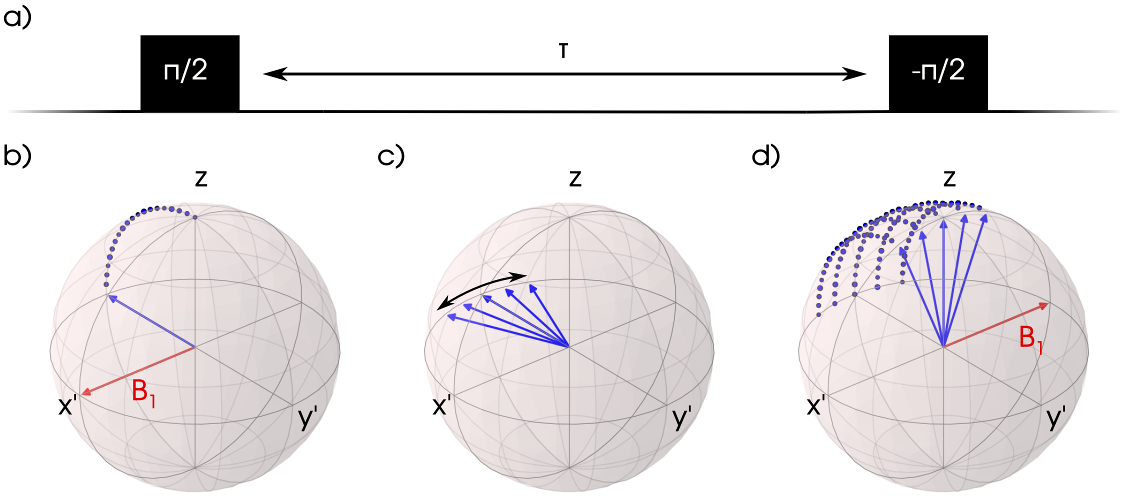

Figure 2.6: a) Sketch of the Ramsey sequence. Two π/2-pulses are separated by a evolution time τ. b) The first π/2-pulse excites the spins from $\vec{e}_z$ onto $\vec{e}_{y'}$. c) During the time τ the spins dephase due to local B_0-inhomogeneities. d) The second π/2-pulse projects the spins from the x'-y'-plane back onto $\vec{e}_z$ for readout.

from ^{29}Si and the dangling bond readout partner [58] or to obtain the true linewidth through Fourier transform spectroscopy [61].

The Ramsey sequence consists of two π/2-pulses separated by an evolution time τ (figure 2.6 a)). The first π/2-pulse excites the spin state into the x'-y'-plane (figure 2.6 b)). During the evolution time, the spins in the sample precess according to their resonance frequency, which varies due to e.g. local inhomogeneities of the external magnetic field caused by the microscopic surroundings of the spin. This leads to a spreading (so-called dephasing) of the spins in the x'-y'-plane (figure 2.6 c)). Since EDMR is only sensitive to polarizations, a second π/2-pulse projects the spins in the x'-y'-plane back onto the z-axis [58] (figure 2.6 c)) similar to optically detected magnetic resonance (ODMR) experiments [62, 63] and other pEDMR [47] experiments.

By sweeping τ during the Ramsey experiment the dephasing of the signal during the evolution time is reconstructed and a Fourier transform will yield the true linewidth if the excitation and projection pulse have a bandwidth which exceeds the linewidth.

Due to the two pulse nature of the experiment the phase of the second pulse can be switched by π at every other sequence (phase cycling), which reverses the rotation direction of the projection pulse. This yields a total rotation by π or by 0 for successive sequences which can be employed as a lock-in [59] to increase the signal-to-noise ratio.

Due to this simple lock-in implementation, a variation of this sequence is used to benchmark the performance of $\pi/2$-pulses in this work (c.f. section 5). In this sequence, τ is set to zero and the excitation pulse is replaced by the pulse being evaluated. By sweeping the number of duplicates N of this pulse, rotations with an angle $\Theta = N \cdot \pi/2$ are achieved while the lock-in technique guarantees a flat baseline simplifying the analysis of the pulse performance.

2.3.3 Hahn echo sequence

The Hahn echo sequence [64] is the basic building block of many pulse sequences. Apart from decay measurements determining T_2 (e.g. [47, 63]), it is utilized in magnetic resonance imaging [52], to measure the coupling strength between spins in the electron spin echo envelope modulation (ESEEM) experiment (e.g. [45] and [65]), as a building block of the Davies ENDOR sequence [66] and in a swap gate, which transfers coherences between two coupled spins [67].

The Hahn echo sequence adds a refocusing π-pulse, which performs a π-rotation around $\vec{e}_{x'}$, between the excitation and projection pulse of the Ramsey sequence (figure 2.7 a)). The effect of this pulse is to reverse the relative position of the spins in the x'-y'-plane with respect to $\vec{e}_{y'}$ (figure 2.7 d)). Therefore, the phase gained by each spin during the first evolution time τ_1 (figure 2.7 c)) is rewound during the second evolution time τ_2 (figure 2.7 e)).

If τ_1 and τ_2 are equal, this leads to collinear spins at the beginning of the projection pulse (figure 2.7 f)) and a total rotation angle of 2π of the experiment. This results in a minimum of the signal, because the phosphorus-dangling bond spin pair is left in its initial parallel state. For unequal evolution times, the rewinding effect is not complete which results in dephased spins at the beginning of the projection pulse. In the case of hugely different τ_1 and τ_2, the dephasing results in a uniform distribution of the spins on the x'-y'-plane and therefore half the spin pairs are in an antiparallel

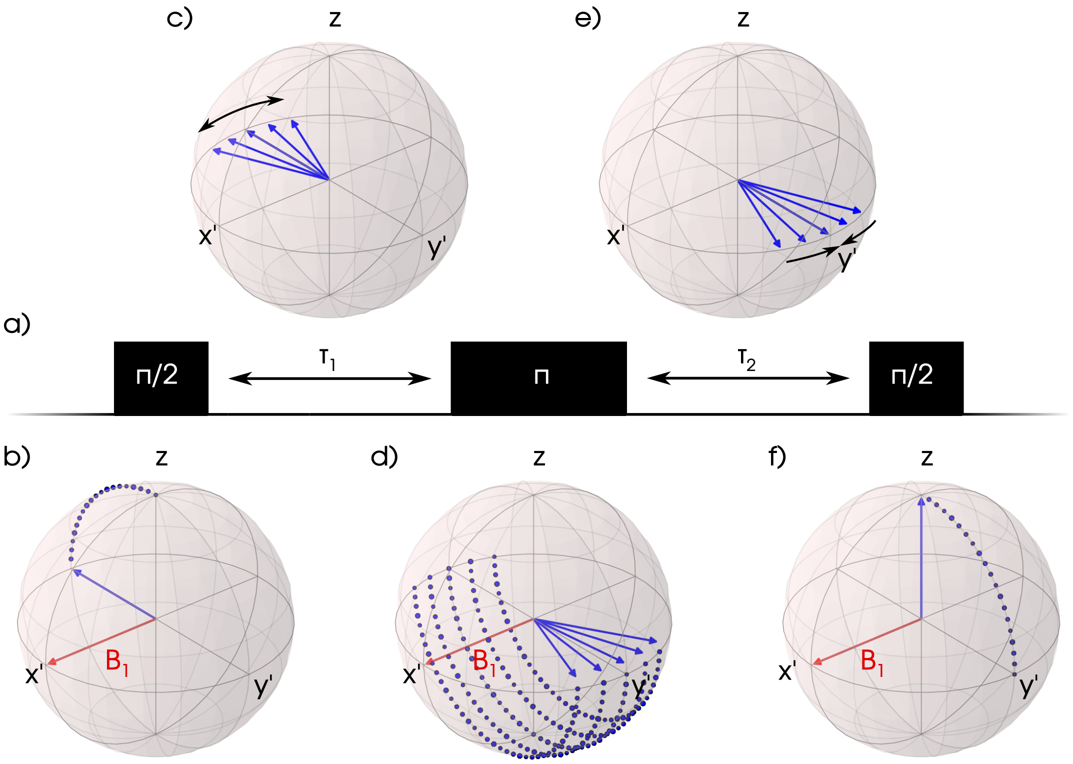

Figure 2.7: a) Sketch of the echo sequence. The echo sequence inserts a π-pulse between the two π/2-pulses of the Ramsey sequence separating the evolution time τ into two evolution times τ_1 and τ_2. b) The first π/2-pulse excites the spins from $\vec{e}_z$ onto $\vec{e}_{y'}$. c) During the first evolution time τ_1 the spins dephase due to local B_0-inhomogeneities. d) The refocusing π-pulse rotates the spins around $\vec{e}_{x'}$ by π and therefore reverses the spins relative position to $\vec{e}_{y'}$. e) During the second evolution time τ_2 the spins precess around $\vec{e}_z$ due to local B_0-inhomogeneities. Since their relative positions to $\vec{e}_{y'}$ are reversed, this compensates the dephasing during τ_1 if $\tau_1 = \tau_2$. f) The second π/2-pulse projects the spins from the x'-y'-plane back onto $\vec{e}_z$ for read-out.

state after the projection pulse, which results in an increased signal compared to the case $\tau_1 = \tau_2$.

Phase cycling works in a similar fashion to the Ramsey sequence with the only difference being the total rotation angle which alternates between 0 and 2π. Since this sequence is widely used in ESR, we employ it to benchmark the performance of different pulses in a sequence.

2.4 Magnetic resonance imaging

Magnetic resonance imaging (MRI) [68, 69] has revolutionized the imaging of the human body for medical applications (e.g. [70, 71]). The same method can be applied to ESR [72, 73], EDMR [60] and ODMR [74, 75] with a resolution of up to 3 nm [74].

MRI uses the dependence of the Larmor frequency ω_L on the external magnetic field B_0 together with a spatially constant magnetic field gradient $\vec{G} = G\vec{e}_z$ to encode the position of a certain spin in the sample in a phase Φ which is then measured with either inductive, electrical or optical detection. The following one-dimensional derivation follows the discussion in reference 52 and describes the method of phase encoding for a gradient $\vec{G}_x = G_x\vec{e}_z$ along $\vec{e}_x$. It is easily adjusted to two or three dimensions by applying additional gradients $\vec{G}_y = G_y\vec{e}_z$ and $\vec{G}_z = G_z\vec{e}_z$ along $\vec{e}_y$ and $\vec{e}_z$, respectively.

A gradient $\vec{G}_x$ along $\vec{e}_x$, which can either be constant or varying in time, results in a magnetic field dependence

$$\vec{B}_0\left(x\right) = \left(B_0 + G_x x\right)\vec{e}_z. \tag{2.13}$$

If we assume a rotating frame with $\omega_0 = \gamma B_0$ this yields a position-dependent precession $\Delta\omega\left(x\right)$ in the rotating frame of

$$\Delta\omega\left(x\right) = \gamma G_x x. \tag{2.14}$$

For a rectangular pulsed G_x with a pulse length T_P a spin at position x acquires a phase Φ during the length of the gradient pulse

$$\Phi\left(x\right) = \gamma G_x x T_\mathrm{P} = 2\pi k_x x \tag{2.15}$$

$$\text{with} \quad k_x = \frac{\gamma G_x T_\mathrm{P}}{2\pi}. \tag{2.16}$$

For a single spin a measurement of this phase would directly yield its position x, but in an ensemble the magnetizations of all the spins add up so that the phase cannot be extracted directly. In this case it is necessary to measure the total magnetization $\vec{M}\left(x\right)$ to find the phase.

Since the gradient only causes an additional phase just the magnetization $M_\perp\left(x\right)$ perpendicular to $\vec{B}_0$ holds the position information.

Therefore, $M_\perp(x)$ can be described by using complex numbers and the phase $\Phi(x)$. It reads as

$$M_\perp(x) = M_x(x) + iM_y(x) = |M_\perp(x)|\, e^{-i\Phi x}. \tag{2.17}$$

The total signal $S(k_x)$ is then the integral over all magnetizations

$$S(k_x) = \int M_\perp(x)\,\mathrm{d}x = \int |M_\perp(x)|\, e^{-i\Phi x}\mathrm{d}x = \int |M_\perp(x)|\, e^{-2\pi i k_x x}\mathrm{d}x, \tag{2.18}$$

which is effectively the Fourier transform of $|M_\perp(x)|$. Therefore, a measurement of $S(k_x)$ in k-space followed by a Fourier transform will yield $|M_\perp(x)|$. Since only a limited number of k_x can be measured during an acquisition, $|M_\perp(x)|$ is calculated through the discrete Fourier transform [76] and the field of view f is determined by the Nyquist sampling theorem to

$$f = \frac{1}{\Delta k_x}, \tag{2.19}$$

with Δk_x the discrete distance between two k-space values. The maximal spatial resolution Δx of $|M_\perp(x)|$ is determined by the number N of k-space values and the field of view f to

$$\Delta x = \frac{f}{N} = \frac{1}{N\Delta k_x}. \tag{2.20}$$

To ease the requirements on the gradient strength, the gradient is recorded from $-k_{\mathrm{max}}$ to k_{max} yielding an achievable resolution of

$$\Delta x = \frac{1}{2k_{\mathrm{max}}} = \frac{2\pi}{2\gamma G_{\mathrm{max}} T_{\mathrm{P}}} = \frac{h}{2g\mu_e G_{\mathrm{max}} T_{\mathrm{P}}}. \tag{2.21}$$

In MRI, typically, gradient pulses are inserted into the free precession times in a Hahn echo [60, 73–75] (figure 2.8 a)). The corresponding gradient pulse sequence is displayed in figure 2.8 b). The arrows indicate the gradient direction and the gradient table depicts the variation of G_x which is needed to build the k-space image. To increase the resolution, a gradient pulse can be inserted into both free precession times as is shown in figure 2.8 b).

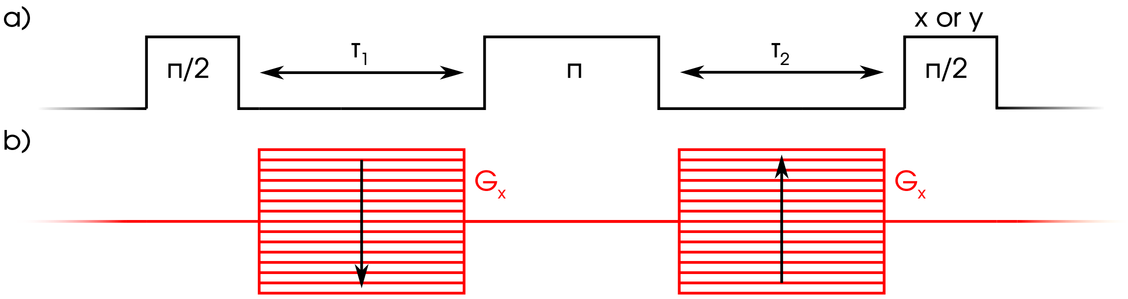

Figure 2.8: a) Sketch of the echo sequence used for MRI. The projection pulse cycles between a phase of 0° and 90° corresponding to a rotation around $\vec{e}_{x'}$ or $\vec{e}_{y'}$ to measure the complex response of the echo to the gradient pulses. b) Gradient pulses inserted into the evolution times τ_1 and τ_2 of the echo sequence. The gradient table symbolizes the sweeping of the gradient strength. The direction of the gradient (depicted by the arrows) is switched between the first and the second pulse to avoid an unwinding of the induced phase.

To avoid unwinding the phase accumulated during the first pulse the gradient direction must be opposite in both precession times (black arrows).

For the Fourier transformation a complex k-space signal is necessary. In MRI, this information is contained in the amplitude and phase of the induction signal, but EDMR cannot measure phases in the x'-y'-plane directly. To extract the phase information from EDMR measurements, it is necessary to measure the gradient echo twice. One sequence, where all pulses have the same rotation angle, yields the real part of the k-space image, while a sequence where the rotation angle of the projection pulse is changed by 90° (e.g. by adding a phase of $\varphi = 90°$ to the pulse) allows to measure its imaginary part [60].

In NMR the method of frequency encoding is commonly employed to speed up the MRI acquisition. It places the gradient at the point of echo acquisition [52] which results in a modulation of the echo due to the spatial distribution of the spins. Similar to the method of phase encoding, the spatial distribution is obtained by a Fourier transformation of the echo signal. Since induction detection allows the acquisition of an echo in one shot, this enables the

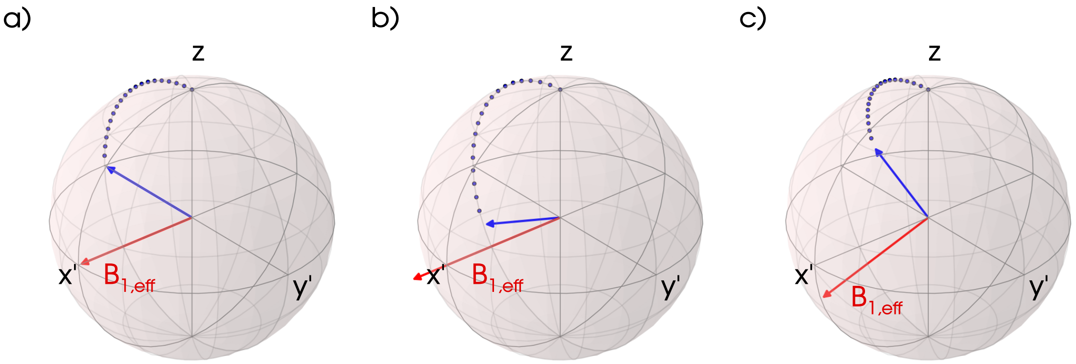

Figure 2.9: Magnetization on the Bloch sphere (blue arrow) and corresponding driving field B_1 (red arrow) for resonant spins with the correct driving strength (panel a)), for resonant spins with an increased B_1 (panel b)) and for off-resonant spins (panel c)).

acquisition of the spatial information along one axis with only one measurement. Unfortunately, this method does not yield the same improvements in EDMR and ODMR, because both detection methods cannot measure the full echo in one shot, but need to reconstruct it with projection pulses. Therefore, frequency encoding does not offer any improvement over phase encoding and we accordingly chose phase encoding for the measurements in this work.

2.5 Shaped pulses

The pulse sequences discussed up to now (sections 2.3.1, 2.3.2, 2.3.3 and 2.4) rely on rectangular microwave pulses with well defined phases Φ. As an example, figure 2.9 a) displays the resulting magnetization (blue arrow) and the corresponding driving field B_1 (red arrow) on the Bloch sphere after such a pulse.

A B_1-inhomogeneity will result in different rotation angles (as shown exemplarily for higher B_1 in figure 2.9 b)) for spins experiencing different B_1-fields. Off-resonance effects, e.g. from different couplings to surrounding spins, will tilt the rotation axis, because the magnetic field as seen by the spins contains not only the component caused by the microwaves, but also a component due to the detuning (as shown exemplarily for $\Delta\omega > 0$ in figure 2.9 c)). In the best case these deviations only cause a quenched amplitude of the respective experiment (c.f. sections 4.3, 4.4, 5.3 and 5.4). In the worst case, they result in wrong measurement results (c.f. sections 6.1.5 and 6.3).

These problems led to the development of composite [77], adiabatic [78] and optimal control pulses [25, 27, 30, 33] for nuclear magnetic resonance (NMR) which are able to counter the adverse effects of B_1-inhomogeneities and off-resonance excitation. In the following sections we discuss the design principles behind adiabatic (section 2.5.1) and optimal control pulses (section 2.5.2). Composite pulses, which are constructed by concatenating rectangular pulses with selected phases and amplitudes, are effectively a subclass of the optimal control pulses and are therefore not discussed here.

The adiabatic and optimal control pulses used in this work can be sorted in two basic categories: point-to-point and universal rotation pulses. Universal rotation pulses, similar to rectangular pulses, have a rotation axis and angle around which all spins rotate. Therefore, these pulses can easily replace all rectangular pulses. In contrast, point-to-point pulses transform a spin from a given starting point to a specific endpoint on the Bloch sphere. Spins that do not lie on the intended starting point will end up at seemingly random positions depending on their position in the B_1-off-resonance space. In general, point-to-point pulses are simpler because they do not need to fulfill as many boundary conditions, but they can only replace specific pulses with fixed start and end position of the spins.

In pEDMR experiments, the excitation pulse can be replaced by a point-to-point pulse because the starting position along the z-axis and the end position in the x'-y'-plane are known. The same argument is true for projection pulses, which transform the projection along e.g. the x'-axis onto the z-axis. However, refocusing pulses only work due to the rotation around a certain axis and can therefore only be replaced by a universal rotation pulse.

2.5.1 Adiabatic Pulses

Adiabatic pulses use the fact that an off-resonance pulse produces a magnetic field along $\vec{e}_z$ in the rotating frame (c.f. equation 2.10).

To describe adiabatic pulses we employ a rotating frame, which rotates with the frequency of the pulse and instantly follows any frequency changes during the pulse (accelerated rotating frame). Vector addition yields the resulting effective magnetic field $\vec{B}_{1,\text{eff}}$ in this accelerated rotating frame

$$\vec{B}_{1,\text{eff}} = \begin{pmatrix} B_1 \\ 0 \\ \frac{\Delta\omega}{\gamma} \end{pmatrix}, \tag{2.22}$$

around which the spins precess during a microwave pulse. The basic idea behind adiabatic pulses is to align this effective magnetic field parallel or antiparallel to the spins and gradually change it during the pulse. If these changes happen slowly compared to the precession, the spins will follow the movement of the effective magnetic field, which results in the intended spin rotation [78].

2.5.1.1 Point-to-point pulses

We employ two types of point-to-point pulses in this work. They are either transformations from $\vec{e}_z$ to $-\vec{e}_z$ (also called adiabatic full passage or AFP) or from $\vec{e}_z$ into the x'-y'-plane (adiabatic half passage or AHP). We will describe the AHP first.

To perform an AHP, $\vec{B}_{1,\text{eff}}$ has to travel from $\vec{e}_z$ to the x'-y'-plane. We choose the x'-axis as an endpoint without loss of generality. To achieve this movement we start with the microwave frequency detuned by $\Delta\omega$ and B_1 reduced to nearly zero. The resulting $\vec{B}_{1,\text{eff}}$ is (c.f. equation 2.22)

$$\vec{B}_{1,\text{eff}} = \begin{pmatrix} B_1 \approx 0 \\ 0 \\ \frac{\Delta\omega}{\gamma} \end{pmatrix} \approx \frac{\Delta\omega}{\gamma}\vec{e}_z. \tag{2.23}$$

By gradually increasing B_1 to $B_{1,\text{max}}$ and reducing $\Delta\omega$, $\vec{B}_{1,\text{eff}}$ moves from $\vec{e}_z$ to $\vec{e}_{x'}$ until the rotating frame rotates with the Larmor frequency of the spin and $\Delta\omega = 0$ which results in

$$\vec{B}_{1,\text{eff}} = \begin{pmatrix} B_{1,\text{max}} \\ 0 \\ \frac{\Delta\omega}{\gamma} \approx 0 \end{pmatrix} \approx B_{1,\text{max}}\vec{e}_{x'}. \tag{2.24}$$

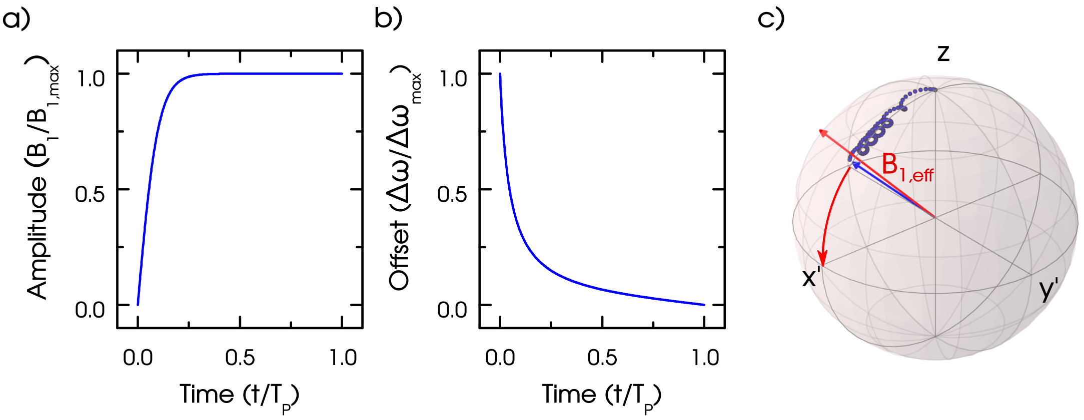

Figure 2.10: a) Amplitude of an AHP pulse as a function of the normalized pulse time t/T_P. b) Frequency offset of an AHP pulse as a function of the normalized pulse time t/T_P. c) Movement of the magnetization (blue arrow) due to the effective magnetic field $\vec{B}_{1,\mathrm{eff}}$ (red arrow). The trajectory of the magnetization is depicted by the blue dots.

Figure 2.10 plots the amplitude (panel a)) and offset curve (panel b)) which yield this transformation for the example of a tanh amplitude modulation and a tan frequency modulation as a function of the normalized pulse time t/T_p. The modulation functions are

$$B_1(t) = B_{1,\mathrm{max}} \cdot \tanh\left(\zeta\left(1 - t/T_\mathrm{p}\right)\right) \tag{2.25}$$

$$\Delta\omega(t) = \Delta\omega_\mathrm{max} \cdot \frac{\tan\left(\kappa t/T_\mathrm{p}\right)}{\tan\kappa}. \tag{2.26}$$

Here, the constants ζ and κ specify the form of the amplitude and phase modulation, respectively. $B_{1,\mathrm{max}}$ is the maximum microwave field, $\Delta\omega_\mathrm{max}$ is the maximum detuning and T_p is the length of the pulse.

To optimize the parameters of those two modulation functions, the adiabaticity η which relates the change of the angle a between $\vec{B}_{1,\mathrm{eff}}$ and $\vec{e}_z$ with the precession frequency $\omega_\mathrm{eff} = \gamma B_{1,\mathrm{eff}}$

$$\eta = \frac{\omega_\mathrm{eff}}{\frac{\mathrm{d}a}{\mathrm{d}t}} \tag{2.27}$$

is maximized. It is a measure of the quality of an adiabatic pulse and has to fulfill $\eta \gg 1$ to ensure that the spins follow $B_{1,\mathrm{eff}}$.

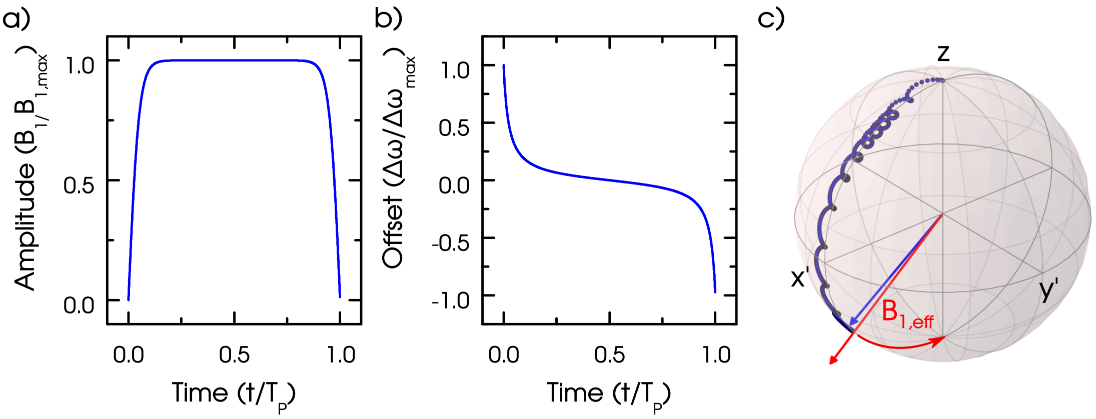

Figure 2.11: a) Amplitude of an AFP pulse as a function of the normalized pulse time t/T_P. b) Frequency offset of an AFP pulse as a function of the normalized pulse time t/T_P. c) Movement of the magnetization (blue arrow) due to the effective magnetic field $\vec{B}_{1,\mathrm{eff}}$ (red arrow). The trajectory of the magnetization is depicted by the blue dots.

This is shown in figure 2.10 c) which plots the magnetization (blue arrow), $\vec{B}_{1,\mathrm{eff}}$ (red arrow) and the trajectory of the magnetization (blue dots) on the Bloch sphere.

Any component of the spin which is not parallel to $\vec{e}_z$ at the beginning of the pulse will also precess around $\vec{B}_{1,\mathrm{eff}}$, but the end position will in general depend on B_1 and result in an arbitrary end position for each spin in an ensemble. Apart from the adiabaticity, this pulse has to fulfill a second condition which follows directly from equation 2.24. For any ensemble with a linewidth $\Delta\omega_l$ in frequency space the z-component of equation 2.24 cannot be zero for all spins. In order to achieve $\Delta\omega/\gamma \approx 0$ for all spins, B_1 has to be much larger than $\Delta\omega_l/\gamma$ so that $\vec{B}_{1,\mathrm{eff}}$ is approximately collinear with $\vec{e}_z$ for most of the spins in the ensemble although a small off-resonance component remains.

An AFP pulse does not stop at the resonance condition, but adjusts the frequency up to $-\Delta\omega$ which results in

$$\vec{B}_{1,\mathrm{eff}} = \begin{pmatrix} B_1 \approx 0 \\ 0 \\ \frac{\Delta\omega}{\gamma} \end{pmatrix} \approx \frac{-\Delta\omega}{\gamma}\vec{e}_z \tag{2.28}$$

at the end of the pulse if B_1 is reduced to zero. Figure 2.11 plots the amplitude (panel a)) and offset curve (panel b)) using the modulation functions 2.25 and 2.26, respectively, which yield this transformation as a function of the normalized pulse time t/T_p. If $\eta \gg 1$, the spins will follow this movement from $\vec{e}_z$ to $-\vec{e}_z$ as is shown in figure 2.11 c).

Any spin parallel or antiparallel to $\vec{B}_{1,\mathrm{eff}}$ will follow this movement throughout the pulse. In contrast to the AHP, there are no further conditions if the frequency sweep is large enough compared to the linewidth $\Delta\omega_\mathrm{l}$, because the end position of the spins does not depend on the exact detuning $\Delta\omega$ as long as it is large enough for equation 2.28 to hold. Similar to the AHP, any spin component perpendicular to $\vec{B}_{1,\mathrm{eff}}$ at the beginning of the pulse will end up at seemingly random positions depending on its B_1 and off-resonance condition. Therefore, both the AHP and AFP are point-to-point pulses and cannot rotate a spin around a certain axis.

2.5.1.2 Universal rotation pulses

In order to construct a universal rotation pulse from a point-to-point pulse, the more or less arbitrary rotation around $\vec{B}_{1,\mathrm{eff}}$ has to be canceled. There exist many different pulses which achieve this by concatenating AHPs in different ways [20, 22, 79]. In this work we will use the so called BIREF-1 and the BIR-4 pulses. An extensive comparison between further pulse shapes for universal rotation pulses can be found in references 20, 78 and 79.

To reverse the phase which the spins pick up due to the precession around $\vec{B}_{1,\mathrm{eff}}$ during an AHP, the BIREF-1 pulse [79] concatenates two AHPs, where the second is time-reversed and has an amplitude function which is inverted compared to the first AHP. The resulting amplitude and frequency offsets as a function of the normalized pulse time t/T_P are plotted in figure 2.12 a). Their effect on the movement of a magnetization initially along $\vec{e}_z$ (blue arrow) and a magnetization initially along $\vec{e}_{x'}$ (fading green arrows) due to the effective magnetic field $\vec{B}_{1,\mathrm{eff}}$ is plotted in figure 2.12 b) and c) for the first and second AHP, respectively. The amplitude inversion after the first AHP leads to a precession around $\vec{B}_{1,\mathrm{eff}}$ during the second AHP whose direction of rotation is reversed (c.f. rotation direction of the fading green arrows in figure 2.12 b) and c)) and thus unwinds the

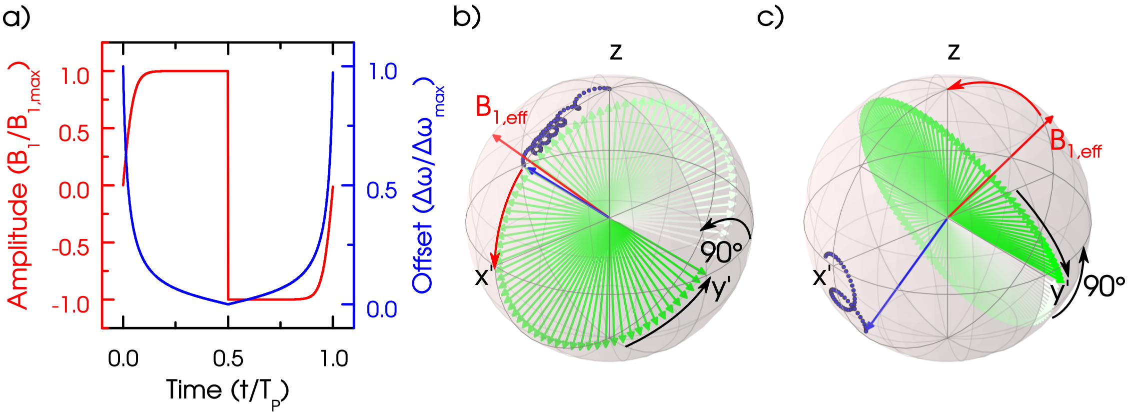

Figure 2.12: a) Amplitude and frequency offset of the BIREF-1 pulse as a function of the normalized pulse time t/T_P. b) Movement of the magnetization for a magnetization initially along $\vec{e}_z$ (blue arrow) and a magnetization initially along $\vec{e}_{x'}$ (fading green arrows) due to the effective magnetic field $\vec{B}_{1,\mathrm{eff}}$ (red arrow) during the first AHP pulse. The trajectory of the magnetization initially along $\vec{e}_z$ is depicted by the blue dots. c) The same as panel b) but for the second AHP pulse.

phase accumulated during the first AHP. The spin transformation of this pulse can be reconstructed by following the movement of $\vec{B}_{1,\mathrm{eff}}$. To do this, we use spins initially aligned along $\vec{e}_{x'}$, $\vec{e}_{y'}$ and $\vec{e}_z$.

For a spin aligned along $\vec{e}_z$ this pulse is basically an AFP. The spin follows $\vec{B}_{1,\mathrm{eff}}$ during the first AHP until $\vec{B}_{1,\mathrm{eff}}$ and the spin are aligned along $\vec{e}_{x'}$ (c.f. blue arrow in figure 2.12 b)). The reversal of the amplitude changes the orientation between the spin and $\vec{B}_{1,\mathrm{eff}}$ from parallel to antiparallel or vice versa. Since the spin will also follow the movement of an antiparallel $\vec{B}_{1,\mathrm{eff}}$, the movement of $\vec{B}_{1,\mathrm{eff}}$ rotates the spin from $\vec{e}_{x'}$ to $-\vec{e}_z$ resulting in a π-rotation (figure 2.12 c)). The reversal of $\vec{B}_{1,\mathrm{eff}}$ from parallel to antiparallel will only work satisfactorily, if $\vec{B}_{1,\mathrm{eff}}$ is nearly parallel to $\vec{e}_{x'}$ after the first AHP. Any off-resonance effects will result in an incomplete reversal of $\vec{B}_{1,\mathrm{eff}}$ since the direction of the off-resonance component of $\vec{B}_{1,\mathrm{eff}}$ does not change. Therefore, this pulse also has to fulfill the condition $B_1 \gg \frac{\Delta\omega_1}{\gamma}$ similarly to an AHP.

Spins along $\vec{e}_{x'}$ and $\vec{e}_{y'}$ will precess on a plane perpendicular to $\vec{B}_{1,\mathrm{eff}}$ (fading green arrows in figure 2.12 b) and c)). Since their precession on this plane is reversed during the second AHP we can

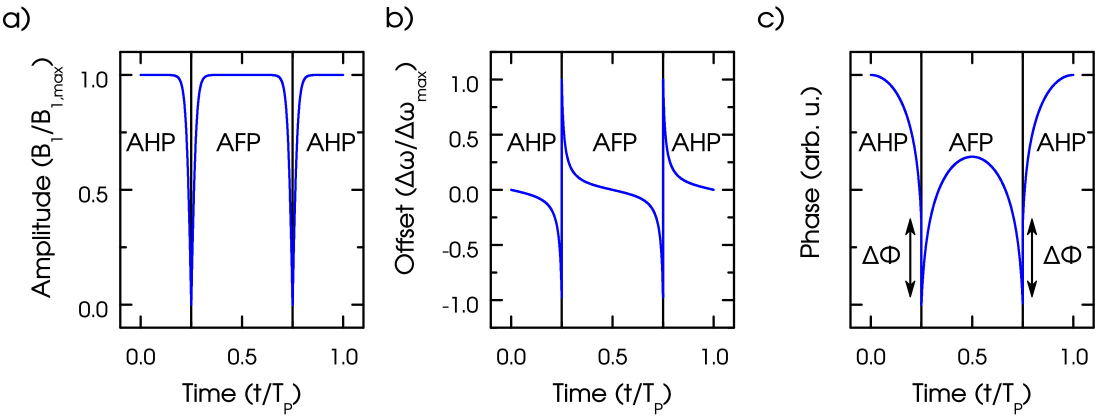

Figure 2.13: Amplitude (panel a)), frequency offset (panel b)) and phase (panel c)) of a BIR4 pulse as a function of the normalized pulse time t/T_P. Here, the phase is defined by the integral over the offset $\Delta\omega$ in the case of the two AHP pulses. The phase of the AFP pulse is shifted by a phase $\Delta\Phi$.

ignore the precession and treat them as if they keep their relative position on this plane constant throughout the pulse. Both the first and second AHP rotate the plane by $\pi/2$ around $\vec{e}_{y'}$ (figure 2.12 b) and c)) and therefore realize a total rotation of π. Since the spins initially aligned parallel to $\vec{e}_{x'}$ and $\vec{e}_{y'}$ keep their relative position on this plane, this causes a π-rotation for the spin along $\vec{e}_{x'}$ and no rotation for the spin along $\vec{e}_{y'}$. Therefore, this pulse performs a π-rotation around $\vec{e}_{y'}$ as is expected of a π universal rotation pulse. It is possible to analogously achieve $\pi/2$ universal rotations by differently concatenating two AHPs [20].

The BIR-4 pulse [22] concatenates two AHP pulses and one AFP pulse (concatenated from two AHPs) and can be set to any rotation angle by an additional phase $\Delta\Phi$ which is applied to the AFP. Figure 2.13 plots the amplitude (panel a)), frequency offset (panel b)) and phase (panel c)) of a BIR-4 pulse as a function of the normalized pulse time t/T_P. Between the first AHP and the AFP and again between the AFP and the second AHP the frequency is inverted. This reverses the overall rotation direction of the spins similar to the BIREF-1 pulse (c.f. figure 2.12 b) and c)) and ensures the fact that any rotation around $\vec{B}_{1,\mathrm{eff}}$ acquired by the pulse before the frequency inversion is reversed by the pulse after the frequency inversion. Therefore, we can again ignore the precession around $\vec{B}_{1,\mathrm{eff}}$ during this analysis. $\vec{B}_{1,\mathrm{eff}}$ starts along $\vec{e}_{x'}$ at the beginning of the pulse and is rotated to $-\vec{e}_z$ during the first AHP. At the beginning of the following AFP $\vec{B}_{1,\mathrm{eff}}$ jumps to $\vec{e}_z$ and rotates from $\vec{e}_z$ back to $-\vec{e}_z$. The angle of this rotation is governed by the additional phase Φ of the AFP pulse. After the AFP, $\vec{B}_{1,\mathrm{eff}}$ jumps to $\vec{e}_z$ again from where it travels back to $\vec{e}_{x'}$. To analyze the behavior of the pulse, we will again resort to three spins initially aligned along $\vec{e}_{x'}$, $\vec{e}_{y'}$ and $\vec{e}_z$.

Due to the adiabaticity of the pulse, the spin along $\vec{e}_{x'}$ which is initially parallel to $\vec{B}_{1,\mathrm{eff}}$ will follow the movement of $\vec{B}_{1,\mathrm{eff}}$ through the pulse. This leads to a transformation of the spins from $\vec{e}_{x'}$ to $-\vec{e}_z$ during the first AHP, an inversion of the spin from $-\vec{e}_z$ to $\vec{e}_z$ during the AFP and a transformation from $\vec{e}_z$ to $\vec{e}_{x'}$ during the second AHP. All these transformations result in a spin parallel to $\vec{e}_{x'}$ which was the initial state suggesting that $\vec{e}_{x'}$ is the rotation axis of the pulse.

Since we can ignore the precession, the movement of the spins initially orthogonal to $\vec{B}_{1,\mathrm{eff}}$ can be modeled by simple rotations $\mathbf{R}_{\vec{n}}(\beta)$ around $\vec{n}$ by the angle β. The first AHP rotates by $\pi/2$ around $\vec{e}_{y'}$, the AFP rotates by π around $\vec{n}$ defined by

$$\vec{n} = \begin{pmatrix} \sin(\Phi) \\ \cos(\Phi) \\ 0 \end{pmatrix} \tag{2.29}$$

and the second AHP again rotates by $\pi/2$ around $\vec{e}_{y'}$. Hence, the resulting rotation by an angle β around the axis $\vec{s}$ is defined by the concatenation of the rotations during the AHP and AFP pulses

$$\mathbf{R}_{\vec{s}}(\beta) = \mathbf{R}_{\vec{e}_{y'}}(\pi/2)\,\mathbf{R}_{\vec{n}}(\pi)\,\mathbf{R}_{\vec{e}_{y'}}(\pi/2)\,. \tag{2.30}$$

To simplify this expression, the rotation matrices are evaluated at their respective rotation angle and rotation axis and the matrix multiplication is carried out. Using the trigonometric double angle relations we find

$$\mathbf{R}_{\vec{s}}(\beta) = \begin{pmatrix} 1 & 0 & 0 \\ 0 & \cos(2(\pi-\Phi)) & -\sin(2(\pi-\Phi)) \\ 0 & \sin(2(\pi-\Phi)) & \cos(2(\pi-\Phi)) \end{pmatrix}. \tag{2.31}$$

This is a rotation by $\beta = 2(\pi - \Phi)$ around $\vec{s} = \vec{e}_{x'}$ and allows to adjust the rotation angle β by a simple change in the phase jump Φ.

Compared to the BIREF-1 pulse this degree of freedom comes at the cost of a two-fold increased pulse length. For samples with a short T_2 time adiabatic universal rotation pulses, which have a fixed angle of rotation and therefore a shorter pulse length, can improve the signal by reducing effects due to decoherence of the spins.

2.5.2 Optimal control pulses

Optimal control pulses are pulses optimized by using optimal control theory [25–41]. In optimal control theory [80], a cost function $\mathfrak{J}(x(t), u(t), t)$ is minimized to find the most suitable trajectory $x(t)$ using a set of controls $u(t)$. This trajectory may be e.g. the shortest, the fastest or the most energy efficient one depending on the cost function. A control could be e.g. an external force on the subject.

In the case of microwave pulses for EDMR, the trajectory is that of the magnetization $M(t)$ and the controls are the amplitude and phase or the x- and y-component of B_1. For computation an optimal control pulse of length T_P is split into short segments of length Δt over which the control inputs are kept constant [25]. This length Δt can either be the time step of the pulse generating hardware or any of its discrete multiples. Apart from this it is also possible to use analytical functions for the control and optimize e.g. the parameters of a frequency sweep or the amplitudes of a discrete sine series [40].

Initially the controls are set to random values or a guessed pulse shape and the magnetization is propagated from its initial M_initial state to a final state M_final by applying the specific pulse. With this final state and the target state M_target, an optimal control cost function which utilizes the scalar product between $\vec{M}_\mathrm{final}$ and $\vec{M}_\mathrm{target}$

$$\mathfrak{J} = \left\langle \vec{M}_\mathrm{final}, \vec{M}_\mathrm{target} \right\rangle = \vec{M}_\mathrm{final} \cdot \vec{M}_\mathrm{target} \tag{2.32}$$

is constructed.[1] This specific cost function will result in an optimized point-to-point pulse because it only depends on the initial and the final state. To optimize universal rotation pulses it has to be adjusted to include e.g. rotation operators [32]. A detailed discussion can be found in references 32, 34 and 35.

---

[1] This cost function is the most simple form and has to be expanded if boundary conditions are to be included.

A finite-differences-based gradient algorithm could be used to optimize the cost function, but it would require to calculate the gradient for all N pulse segments resulting in $2N$ evaluations of $\mathfrak{J}$. Since N can easily reach the order of 1000 and since each evaluation of $\mathfrak{J}$ requires an additional propagation of $\vec{M}$ per iterated pulse shape, this becomes rather quickly computationally expensive.

Optimal control theory provides an efficient way to evaluate this gradient through the cross product of $\vec{M}(t)$ and the costate vector $\vec{\jmath}(t)$, which can be understood as the vector Lagrange multiplier to the Bloch equation [25, 26, 31]

$$\frac{\mathrm{d}\mathfrak{J}}{\mathrm{d}B_{\mathrm{eff}}(t)} = \vec{M}(t) \times \vec{\jmath}(t)\,. \tag{2.33}$$

Here, the costate vector $\vec{\jmath}(t)$ is the back-propagation of $\vec{M}_{\mathrm{target}}$ under the influence of the current realization of the microwave pulse. Therefore, the evaluation of the gradient only requires the propagation of $\vec{M}_{\mathrm{initial}}$ and the back-propagation of $\vec{M}_{\mathrm{target}}$ which greatly reduces the computational cost for the optimization (gradient ascent pulse engineering (GRAPE) [25]). In order to construct pulses which work over a region of offsets ν_0 and Rabi frequencies ν_1, $\vec{M}(t) \times \vec{\jmath}(t)$ is calculated for each combination of ν_0 and ν_1 and the mean $\left\langle \vec{M}(t) \times \vec{\jmath}(t) \right\rangle$ is used during optimization [25].

Depending on the step Δt used in the discretization of the pulse, the calculated optimal control pulses can exhibit a huge bandwidth over which they may disturb other spins. To circumvent this problem, unwanted frequency components can be filtered out during the optimization which limits the (final) bandwidth of the pulse [32]. Apart from this a further optimization of optimal control pulses in a sequence is possible by allowing subsequent pulses to correct for errors introduced by earlier pulses. These pulses are called cooperative optimal control pulses and are able to significantly reduce the length of each individual pulse in a sequence [37]. This method can also be applied to phase cycles [31], where pulses in different cycles correct the errors made in earlier cycles, but such cooperative phase cycles were not used in this work.

3

EDMR setup for arbitrarily shaped pulses

This chapter introduces the EDMR setup for arbitrarily shaped pulses. We start with a short introduction into the theoretical basics of pulse generation and the propagation of microwave and DC pulses in our setup (section 3.1). Afterwards the actual pEDMR setup with the pulse generation and pulse delivery on the sample is discussed (section 3.2) before we treat the effects and remedies of non-ideal spectrometer behavior (section 3.3).

3.1 Theoretical basics

3.1.1 Complex baseband representation

This section follows reference 81. The pulses applied in this work have a bandwidth of less than 100 MHz at carrier frequencies ν_C in the gigahertz range. This type of waveform is called a passband signal s_P and can be written as

$$s_\mathrm{P}(t) = \sqrt{2}\,(I(t)\cos(2\pi\nu_\mathrm{C}t) - Q(t)\sin(2\pi\nu_\mathrm{C}t))\,. \tag{3.1}$$

Here, $I(t)$ and $Q(t)$ are real valued functions and ν_C is typically chosen to lie in the center of the passband signal. The factor of $\sqrt{2}$ is arbitrary and simplifies the notation. The complex baseband representation of this signal is then defined as

$$s(t) = I(t) + iQ(t), \tag{3.2}$$

which can be connected to $s_\mathrm{p}(t)$ by

$$s_\mathrm{p}(t) = \mathrm{Re}\left(\sqrt{2}s(t)\,e^{2\pi i\nu_\mathrm{C}t}\right). \tag{3.3}$$

Since the fast oscillating term $e^{2\pi i\nu_\mathrm{C}t}$ is known for all times t, all the information of the signal resides in $s(t)$ and we can limit the treatment of the pulses to the complex baseband. For a better understanding, the functions $I(t)$ and $Q(t)$ are related to the amplitude $A(t)$ and the phase $\Phi(t)$ of the passband signal by the relations

$$\begin{aligned} A(t) &= \sqrt{I^2(t) + Q^2(t)}, && (3.4)\\ \Phi(t) &= \arctan\frac{Q(t)}{I(t)}, && (3.5)\\ I(t) &= A(t)\cos\Phi(t) && (3.6)\\ \text{and}\quad Q(t) &= A(t)\sin\Phi(t). && (3.7) \end{aligned}$$

Passband pulses are generated from $I(t)$ and $Q(t)$ using equation 3.1. If the passband signal is known, the complex baseband signal is obtained by multiplying $s_\mathrm{p}(t)$ with $\cos(2\pi\nu_\mathrm{C}t)$ or $\sin(2\pi\nu_\mathrm{C}t)$ and removing the frequency components at $2\nu_\mathrm{C}$:

$$\begin{aligned} \sqrt{2}s_\mathrm{p}(t)\cos(2\pi\nu_\mathrm{C}t) &= I(t) + Q(t)(\cos(4\pi\nu_\mathrm{C}t) - \sin(4\pi\nu_\mathrm{C}t)) && (3.8)\\ &\approx I(t) && (3.9)\\ -\sqrt{2}s_\mathrm{p}(t)\sin(2\pi\nu_\mathrm{C}t) &= Q(t) + I(t)(\sin(4\pi\nu_\mathrm{C}t) - \cos(4\pi\nu_\mathrm{C}t)) && (3.10)\\ &\approx Q(t). && (3.11) \end{aligned}$$

3.1.2 IQ mixer

Both the conversion from the complex baseband to the passband (upconversion) and from the passband to the complex baseband (downconversion) are carried out by an IQ mixer. Figure 3.1 shows

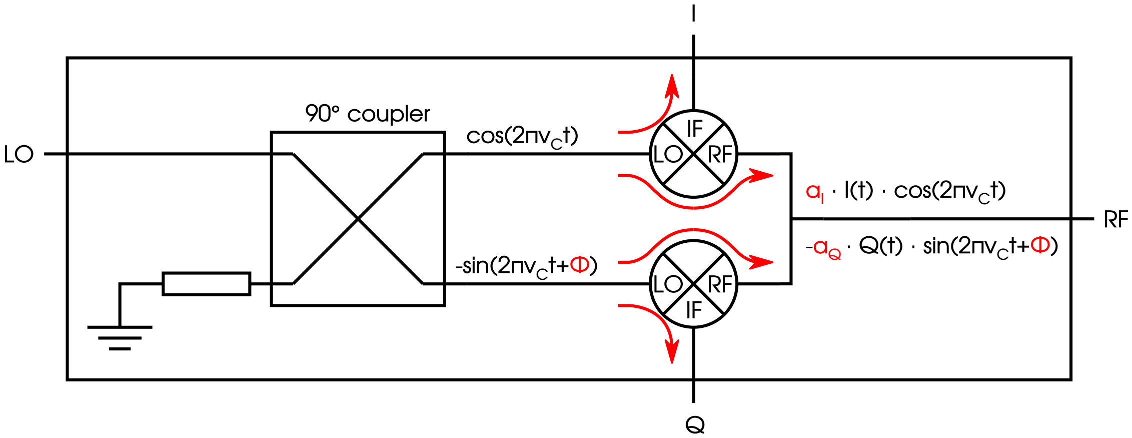

Figure 3.1: Schematic drawing of an IQ mixer consisting of a 90° coupler, two mixers and a combiner. The IQ mixer imperfections LO leak-through, amplitude imbalance and phase imbalance are shown in red.

a schematic drawing of such an IQ mixer. The microwave carrier ν_C, which is input to the LO port, passes a 90° coupler to generate the cosine and sine terms in equation 3.1. If the mixer is used as an upconverter, the baseband signal is fed into the I and Q port where it is multiplied with the respective LO terms. The results of both multiplications are added in a combiner and the resulting passband signal is output to the RF port. If the IQ mixer is used as a downconverter, the RF port acts as the input for the passband signal. The combiner splits the signal evenly between the respective mixers for the I and Q ports where the passband signal is multiplied with the sine or cosine term and the resulting signal is output at the respective port. To obtain a baseband signal this output has to be low-pass-filtered to cut out the high frequency terms in equations 3.9 and 3.11.

As a component, the IQ mixer deviates from the ideal behavior of equation 3.1. Firstly, due to non-ideal isolation between the LO, RF and IF ports of the actual mixers, the LO input can leak into the IF or RF port (red arrows in figure 3.1). This leads to an unmodulated signal with a frequency ν_C in addition to the desired passband signal. Secondly, because of runtime differences in the I and Q channels as well as imperfections in the 90° coupler, the phase between the I and Q ports can deviate by an angle Φ from 90°. Lastly, the ratio $g = a_I/a_Q$ between the gains for the I (a_I) and the Q

(a_Q) ports may differ. Both these latter imperfections are called IQ imbalances and will lead to a distortion of the generated waveform.

3.1.3 Single sideband upconverter

The IQ mixer imperfections discussed in 3.1.2 will lead to aberrations which all coincide with ν_C if $I(t)$ and $Q(t)$ have DC components. By replacing $I(t)$ and $Q(t)$ in equation 3.1 with equations 3.6 and 3.7 and using $\Phi(t) = \Phi + 2\pi\nu_{IF}t$, which shifts the DC I and Q signal by ν_{IF} in frequency, we find

$$s_p(t) = A(t)\cos\left(2\pi\left(\nu_C + \nu_{IF}\right)t + \Phi\right) \tag{3.12}$$

after some trigonometric transformations. Therefore the IQ mixer generates a signal at $\nu_C + \nu_{IF}$. If the I and Q inputs are interchanged, the resulting passband signal will be at $\nu_C - \nu_{IF}$.

To generate the $I(t)$ and $Q(t)$ signal needed for single sideband upconversion, the I and Q inputs of the IQ mixer are fed by two arbitrary waveform generator (AWG) channels or from one AWG channel in combination with a 90° coupler[1]. Any IQ imbalances result in a signal at $\nu_C - \nu_{IF}$ for a passband signal at $\nu_C + \nu_{IF}$ and vice versa [82]. We will call this signal the unwanted sideband from here on.

Since the passband signal resides at $\nu_C + \nu_{IF}$, the LO leakage is at ν_C and the unwanted sideband is at $\nu_C - \nu_{IF}$, all effects are easily discerned from each other. For convenience, the magnitude of the LO leak-through and of the unwanted sideband are expressed comparing their power P_{unwanted} to the power of the wanted sideband P_{wanted} by

$$\text{suppression} = 10\log_{10}\left(\frac{P_{\text{unwanted}}}{P_{\text{wanted}}}\right). \tag{3.13}$$

If the imbalances do not change a lot over the bandwidth of a pulse and if there are no ESR resonances at the frequencies of the LO leak-through and at the frequency of the unwanted sideband, the use of single sideband upconversion might render the correction

---

[1] The 90° coupler allows to use only one AWG channel if the correction of LO leak-through and IQ mixer imbalances is not necessary.

of these errors unnecessary. This, however, is not necessarily the case and we will treat the correction of such imperfections in the next section.

3.1.4 Correction of IQ mixer imperfections

We use the fact that the different imperfections show up at different frequencies to calibrate the IQ mixer and compensate the signals $I(t)$ and $Q(t)$ in order to minimize the effects of the different imperfections.

The LO leak-through of the up- and downconverter can be canceled by applying DC offsets to the $I(t)$ and $Q(t)$ function [83]. To find the right DC offset for each function, the LO leak-through is measured, while one of the DC offsets is varied. When a minimum is found, the procedure is repeated for the other function.

The effect of IQ imbalances can be described by the method in reference 82. Their effect on the modulated $m(t)$ and demodulated $d(t)$ complex baseband signal in vector notation, ignoring leak-through or DC offsets, can be modeled by

$$\widetilde{m}(t) = \mathbf{M}\, m(t) \tag{3.14}$$

$$\text{and} \quad \widetilde{d}(t) = \mathbf{D}\, d(t) \tag{3.15}$$

with the matrices $\mathbf{M}$ and $\mathbf{D}$ defined by

$$\mathbf{M} = \begin{bmatrix} g_\mathrm{M} \cos(\Phi_\mathrm{M}/2) & \sin(\Phi_\mathrm{M}/2) \\ g_\mathrm{M} \sin(\Phi_\mathrm{M}/2) & \cos(\Phi_\mathrm{M}/2) \end{bmatrix} \tag{3.16}$$

$$\text{and} \quad \mathbf{D} = \begin{bmatrix} g_\mathrm{D} \cos(\Phi_\mathrm{D}/2) & g_\mathrm{D} \sin(\Phi_\mathrm{D}/2) \\ \sin(\Phi_\mathrm{D}/2) & \cos(\Phi_\mathrm{D}/2) \end{bmatrix}, \tag{3.17}$$

respectively. Here g_M, g_D, Φ_M and Φ_D denote the gain imbalance and the phase imbalance for the modulator and demodulator, respectively. If those matrices are known, their effects can be reversed by multiplying the modulated or demodulated signal with the corresponding inverse matrix. To find the values of g and Φ it is either possible to measure the amplitude of the unwanted sideband while successively sweeping g and Φ until a minimum is found or the method presented in reference 82 can be used.

We will now briefly describe this method here. It uses microwaves from a single tone source which are downconverted by the IQ mixer under calibration. The resulting output from the I and Q ports is sampled by a fast oscilloscope and Fourier transformed to obtain a complex baseband representation of the signal. The phase imbalance Φ_D and the gain imbalance g_D of the demodulator will result in a signal which does not only contain the desired sideband, generated by the single tone source, but also the unwanted sideband. If the gain and phase imbalance are small, the relative sideband ratio $S_\mathrm{D} = W_2^*/W_1$, where W_2^* is the complex conjugated amplitude of the unwanted sideband and W_1 is the amplitude of the desired sideband, is used to estimate Φ_D and g_D, according to

$$g_\mathrm{D} = \frac{1 + \mathrm{Re}\,(S_\mathrm{D})}{1 - \mathrm{Re}\,(S_\mathrm{D})} \tag{3.18}$$

$$\text{and} \quad \Phi_\mathrm{D} = -2 \arctan\left(\mathrm{Im}\,(S_\mathrm{D})\right). \tag{3.19}$$

To calibrate the modulator the calibrated demodulator is used to measure the power spectrum

$$P_\mathrm{M} = \left|\frac{V_2}{V_1}\right|^2 = \frac{g_\mathrm{M}^2 + 1 - 2g_\mathrm{M}\cos\left(\Phi_\mathrm{M}\right)}{g_\mathrm{M}^2 + 1 + 2g_\mathrm{M}\cos\left(\Phi_\mathrm{M}\right)} \tag{3.20}$$

generated by the wanted (V_1) and unwanted (V_2) sideband. By adjusting g_M by a known quantity and remeasuring the power spectrum, we get two equations with two unknown values, which can be solved to obtain g_M and $|\Phi_\mathrm{M}|$. To find the sign of Φ_M, the power spectrum is measured both for the positive and the negative phase correction values and the value, which results in the better sideband suppression, is used.

In general, LO leak-through and IQ imbalances can be frequency-dependent and may vary slightly in time so that the calibration process has to be repeated at least for each new LO frequency and for each new measurement campaign.

3.1.5 Impulse Response

Every electric circuit will have some imperfections which will alter its response from the intended behavior. Ideally, these deviations are predictable so that the input can be altered to account for those deviations. If an electric circuit is linear and time invariant, its behavior can be modeled by linear system theory [84]. By using the impulse response $h_\mathrm{P}(t)$, which is the response of the system to a Dirac delta function $\delta(t)$, the reaction of the system $y_\mathrm{P}(t)$ to any excitation can be obtained by the convolution of the impulse response $h_\mathrm{P}(t)$ with the excitation $x_\mathrm{P}(t)$:

$$y_\mathrm{P}(t) = (x_\mathrm{P} * h_\mathrm{P})(t) = \int_{-\infty}^{+\infty} h_\mathrm{P}(t-t')\, x_\mathrm{P}(t')\,\mathrm{d}t'. \tag{3.21}$$

This equation can be translated to the complex baseband where it reads as [81]

$$y = \frac{1}{\sqrt{2}}(x * h)(t), \tag{3.22}$$

with the complex baseband representations $y(t)$, $x(t)$ and $h(t)$ of the passband functions $y_\mathrm{P}(t)$, $x_\mathrm{P}(t)$ and $h_\mathrm{P}(t)$, respectively. The in-phase and quadrature-phase components of y are

$$y_\mathrm{I}(t) = (x_\mathrm{I} * h_\mathrm{I})(t) - (x_\mathrm{Q} * h_\mathrm{Q})(t) \tag{3.23}$$

$$\text{and}\quad y_\mathrm{Q}(t) = (x_\mathrm{I} * h_\mathrm{Q})(t) + (x_\mathrm{Q} * h_\mathrm{I})(t), \tag{3.24}$$

which are depicted graphically in figure 3.2. Here, $h_\mathrm{I}(t)$ and $h_\mathrm{Q}(t)$ are the in-phase and quadrature-phase components of the impulse response. The black arrows depict the direction in which $h_\mathrm{I}(t)$ and $h_\mathrm{Q}(t)$ are measured of the device under test (DUT). To obtain $h_\mathrm{I}(t)$ or $h_\mathrm{Q}(t)$, the modulator is excited with $x_\mathrm{I}(t)$ or $x_\mathrm{Q}(t)$ while the other input is terminated and both $y_\mathrm{I}(t)$ and $y_\mathrm{Q}(t)$ are recorded. This results in two measurements for each $h_\mathrm{I}(t)$ and $h_\mathrm{Q}(t)$, which allows to detect e.g. runtime differences or IQ imperfections (c.f. section 3.3.3, where we discuss the experimental realization).

3.1.6 Maximum-length-sequence-based impulse response measurement

For discrete-time impulse response measurements the Dirac delta function is replaced by a Kronecker delta. Since measurements using

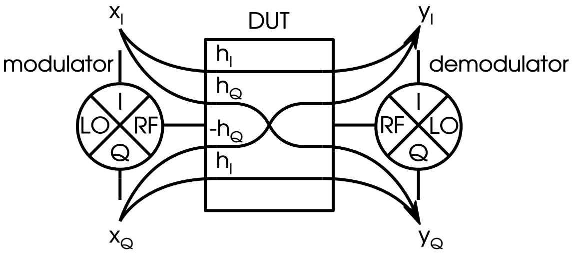

Figure 3.2: Measurement scheme for the baseband impulse response using two IQ mixers. The black arrows depict the direction in which h_I and h_Q are measured for the device under test (DUT). The connections to the LO port of the IQ mixers are left out for clarity.

a single Kronecker delta excitation are very susceptible to noise, there exist numerous ways to measure the impulse response with other methods [85–88]. Reference 88 uses a sampling oscilloscope to measure the generated pulse at its upconverted frequency so that an IQ mixer for downconversion and its calibration is not required. Unfortunately, the jitter of the AWG trigger is too high in our setup so that we cannot employ this method. If the system exhibits strong nonlinearities, an exponentially swept sine measurement [87] can separate the linear response from the different order harmonics at the cost of a preringing of the impulse response [89]. The maximum length sequence (MLS)-based method in reference 85 does not have this disadvantage [89], but produces additional distortion peaks if the system contains nonlinearities [90].

Apart from these methods, a measurement of the system transfer function, using a vector network analyzer (VNA) and a Fourier transformation of this transfer function, will yield the impulse response. This impulse response, however, will not contain the impulse response of the AWG, which has an important influence on the system impulse response (c.f. section 3.3.3). In reference 91 the magnitude of the system transfer function is obtained through nutation experiments at different frequencies. This has the advantage that the transfer function is directly measured by spins, but does not yield the phase component of the frequency transfer function, which makes it impossible to calculate the full impulse response from the magnitude-only transfer function.

The setup in this work is optimized to work in its linear region (c.f. section 3.3.1) so that any advantages of the swept sine method with respect to nonlinearities are outweighed by its distortion of the impulse response. Furthermore, the effects of small nonlinearities on the MLS measurement, e.g. caused by the ADC in the measuring oscilloscope, can be counteracted [90] so that the MLS method seems to be the most suitable method.

In the following, we shortly describe the ideas behind the maximum length sequence measurement. A maximum length sequence m with N elements is a binary sequence [92] generated by a linear feedback shift-register (LFSR) [93] whose characteristic polynomial is primitive [92, 94]. To account for the discrete measurement due to the ADC sampling frequency, equation 3.21 is reformulated in its cyclic discrete form [84]

$$y[k] = (x * h)[k] = \sum_{i=0}^{N-1} x[i]\, h[(k-i)_N]. \tag{3.25}$$

Here k and i are the discrete representations of the time t. x and h represent the system input and the impulse response, respectively. The integral is replaced by the sum over x and h. To simplify the notation, $)_N$ denotes the modulo N operation. Additionally, the discrete cyclic cross correlation can be calculated as [84]

$$\rho_{ab}[k] = \frac{1}{N} \sum_{i=0}^{N-1} a^*[i]\, b[(k+i)_N] \tag{3.26}$$

and can be represented by a convolution using [84]

$$\rho_{ab}[k] = \frac{1}{N} (\hat{a}^* * b)[k] \tag{3.27}$$

with $\hat{a}^*[k] = a^*[-k]$. Both operations assume that the input arrays are of the same length. Usually, the impulse response is short compared to the excitation and has to be zero padded to reach the length of the excitation. The key property of a MLS m is its cyclic autocorrelation function [95]

$$\rho_{mm}[k] = \begin{cases} +1, \text{if } k = 0 \\ -\frac{1}{N}, \text{if } k \neq 0 \end{cases} . \tag{3.28}$$

For large N this approximates an ideal Kronecker delta $\delta[k]$. If we use a MLS as the excitation of our system and cross correlate the system response with the MLS, we find

$$\begin{aligned}
\rho_{my}[k] &= \frac{1}{N}(m^* * y)[k] && (3.29)\\
&= \frac{1}{N}(m^* * (m * h))[k] && (3.30)\\
&= \frac{1}{N}((m^* * m) * h)[k] && (3.31)\\
&\approx (\delta * h)[k] && (3.32)\\
&\approx h[k]\,. && (3.33)
\end{aligned}$$

Therefore, by using the associativity of the convolution together with equation 3.28 we find that the cross correlation of the system response with the MLS approximately yields the system impulse response. Since this operation uses the discrete cyclic convolution and cross correlation, two conditions have to be met. Firstly, the impulse response must be shorter than the play time of the MLS. Secondly, since periodic signals are assumed, the system needs to be excited with at least one period of the MLS before starting the actual measurement to drive the system in a steady state at the beginning of the actual measurement.

For an increasing bit length n of the LFSR, the cross correlation operation scales with p^2 for $p = 2^n - 1$ [94] which can quickly become large. If the computation time grows too large, the cross correlation can be calculated by using the similarities between the MLS matrix and the Hadamard matrix, which reduces the amount of operations to $p \log_2(p)$ [94].

3.2 Hardware

In this section, the setup for pulsed electrically detected magnetic resonance is discussed. The sections 3.2.2, 3.2.4, 3.2.5 and 3.2.6 are based on reference 96.

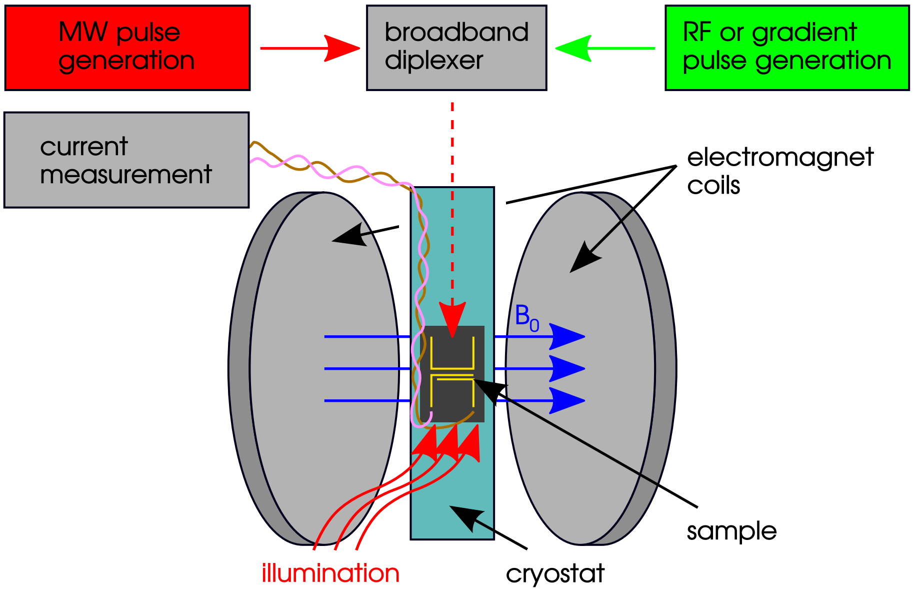

Figure 3.3: Overview of the pEDMR setup.

3.2.1 Overview of the setup

For a successful pEDMR experiment a measurement setup has to provide a method to set a static magnetic field, generate pulsed microwave and radio frequency radiation, deliver it to the sample to be investigated and detect the spin-dependent current through the sample (c.f. chapter 2). Furthermore, for measurements on silicon dopants, the sample needs to be cooled ($T \approx 5\,\mathrm{K}$) and illuminated with above band gap light (c.f. section 2.1.2).

In figure 3.3 the setup used throughout this thesis is sketched schematically. A water-cooled electromagnet (e.g. Bruker B-E 25), which is controlled by a Hall sensor (Bruker B-H 15), generates the external magnetic field B_0. The cryostat (Oxford CF-935) with a window for illumination purposes resides in between the pole caps of the electromagnet. It controls the sample temperature with the help of liquid helium and a computer-controlled heater (Cryogenic Control Systems Model 32B). The sample is mounted on a sample holder which places it behind the cryostat window. It is connected to the microwave and radio frequency pulse generation (c.f. sections 3.2.5, 3.2.6 and 6.1.8) with a semi-rigid coaxial cable with 2.92 mm connectors approved for cryogenic applications (SHF TCRG219G/SUS). The connections for the current measurements (c.f. section 3.2.4) are built by off-the-shelf coaxial cables. Both the microwave transmission line and the current measurement cables are mounted in a sealed glass fiber rod, which sits inside a Swagelock vacuum feed-through mounted into the cryostat with a KF50 vacuum flange [97]. For the pulsed illumination a red LED (Thorlabs M625L3) controlled by a laser diode driver with pulsing capabilities (Thorlabs LDC210C) is used.

3.2.2 Antenna structures

A stripline structure to excite spin resonance has to fulfill the following requirements [18]:

- The amplitude of the oscillating magnetic field B_1 has to be big enough to yield pulse durations shorter than the spin dephasing time T_2^* of the spins to be studied.
- The residual electric field has to be kept as small as possible.

In addition to these requirements, the homogeneity of the B_1-field should be as high as possible to reduce the dephasing in the spin ensembles studied. This excludes downscaling of the antennas to the nanometer scale to achieve the highest possible B_1 conversion factors, since this reduces the size of the spin ensemble or results in higher B_1-inhomogeneities in larger samples.

3.2.2.1 Sample structure

The basic sample structure for all samples used in this work is the same. They are made from pieces of silicon-on-insulator wafers with a 20-nm-thick phosphorus-doped Si top layer with natural isotope composition and a doping concentration of $3 \cdot 10^{16}\,\mathrm{cm}^{-3}$, $9 \cdot 10^{16}\,\mathrm{cm}^{-3}$ or $3 \cdot 10^{17}\,\mathrm{cm}^{-3}$ on top of a 2.5-µm-thick nominally undoped Si layer grown by chemical vapor deposition. For EDMR measurements a measurement geometry is defined by subsequent photolithography, electron-beam evaporation and lift-off steps. Figure 3.4 depicts the layer structure of our samples, whose optimization is described in detail in section 3.2.2.2. On top of the silicon-on-insulator wafer DC contacts, consisting of 20 nm chromium and

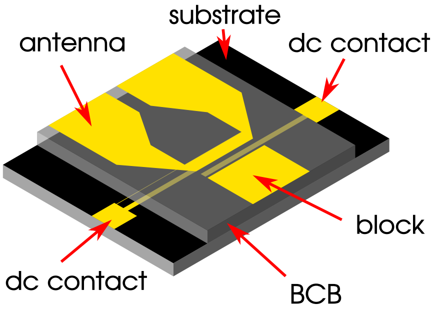

Figure 3.4: Sketch of the phosphorus-doped silicon sample including the silicon semiconductor (black), metalizations for measurement fingers and microwave delivery (yellow) and the BCB isolation layer (transparent).

80 nm gold, define the area through which the spin-dependent current is measured. These contacts are insulated from the microwave delivery structure, consisting of 50 nm of chromium and 500 nm of gold, by a hard-baked layer of benzocyclobutene-based photoresist (BCB). Depending on the sample, a gold block of the same thickness as the microwave delivery structure concentrates the generated microwave B_1-fields into the gap between microwave antenna and block (c.f. section 3.2.2.2). The DC contacts and the microwave delivery structure are connected to a sample holder made of Rogers RO3010 printed circuit board, using aluminum wire bond connections.

3.2.2.2 Simulation of the microwave excitation

The optimization of stripline structures for single spin experiments has been extensively covered [18, 97]. This section summarizes and expands on the results of reference 97 on optimal stripline structures for spin ensembles. For this we simulated the electric and magnetic fields at stripline shorts using the software COMSOL 4.3a. The simulation volume was set to a cube with an edge length of 2 cm and perfectly conducting walls. For the silicon sample a cuboid of the dimensions 15 mm × 4 mm × 0.35 mm positioned in the center of the simulation volume was used. On top of the sample the stripline structure was defined by a perfect electric conductor with infinitely small thickness. The electromagnetic wave was excited by a lumped port with a voltage amplitude of 2 V which corresponds to a microwave power of 40 mW in microwave lines with an impedance of 50 Ω.

Figure 3.5 shows slices through the sample at a frequency of 10 GHz for five simulated structures either 2 µm (panels a), b) and c)) or 20 nm below the stripline structure (d) and e)) depicting either B_{1z} (a), b) and e)) or B_{1x} (c) and d)). In the following, the structures will be called a to e according to their panel labels. The red squares in figure 3.5 a) and b) depict the area where a contact structure such as interdigit fingers would be placed for EDMR experiments with a B_1-inhomogeneity as obtained from the simulation of less than ±5 %. In figure 3.5 c) the area exactly beneath the short has a similar B_1-inhomogeneity of less than ±10 %. In structure d the short width is reduced from 20 µm in structure c to 5 µm. Although fabrication of a contact structure beneath the short is still possible for this reduced width, e.g. using electron beam lithography, it would increase fabrication complexity significantly. Therefore, structure e is intended to be used as microwave delivery and contact structure at the same time. That is why an additional metalization 5 µm in front of the 5-µm-wide short is added ("block" in figure 3.4). The area beneath the short and the gap between stripline structure and the additional contact in figure 3.5 e) have a higher B_1-inhomogeneity of up to ±50 %.

All B_1-amplitudes obtained from the simulation quoted below have been divided by a factor of two since for magnetic resonance only one of the two circularly polarized fields contributes to the spin manipulation in the rotating wave approximation. The average B_1-amplitude inside the indicated measurement area is 0.02 mT for structure a and 0.01 mT for structure b, which results in expected microwave power-to-B_1 conversion factors of $0.1\,\mathrm{mT}\,\sqrt{\mathrm{W}}^{-1}$ and $0.05\,\mathrm{mT}\,\sqrt{\mathrm{W}}^{-1}$, respectively, leading to a power requirement of 13 W and 50 W for 50 ns π-pulses, typical for standard commercial pulsed X-band resonators. The average B_1-amplitude inside the measurement area underneath the short of structure c is 0.14 mT, corresponding to a conversion factor of $0.7\,\mathrm{mT}\,\sqrt{\mathrm{W}}^{-1}$ and a theoretical power requirement of 260 mW for a 50 ns π-pulse. By reducing the short width from 20 µm in structures a, b and c to 5 µm in structure d, the average B_1-field exactly beneath the short can be increased by a factor of four. With the metal contact in front of the short, a similar

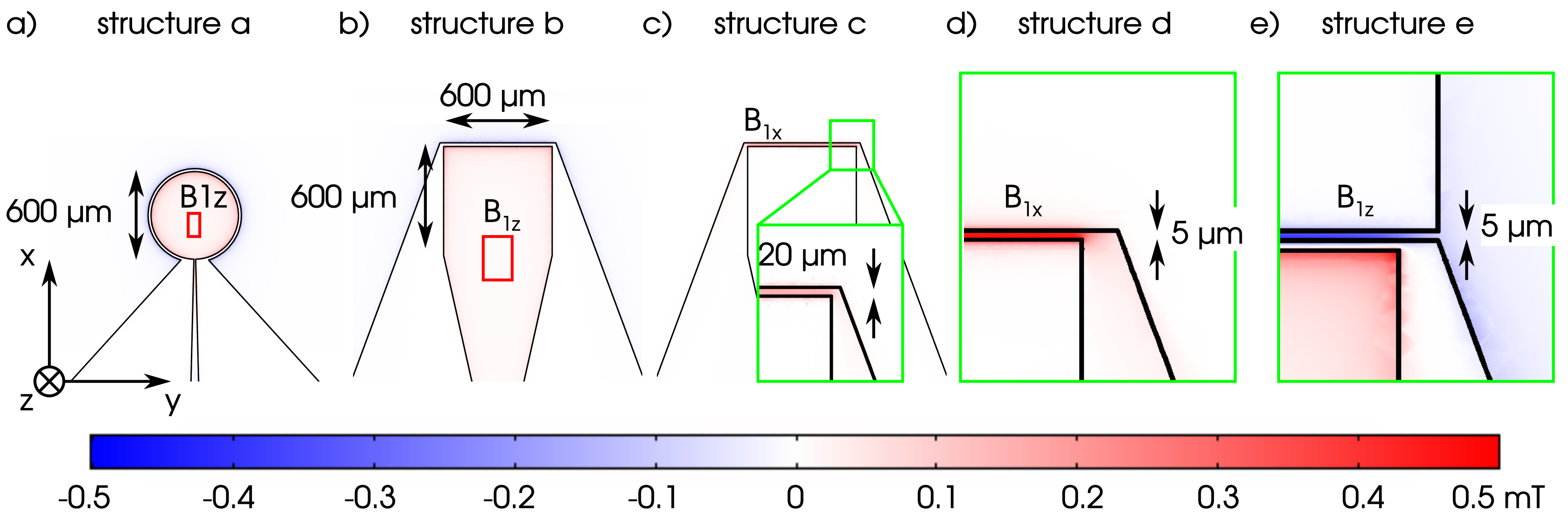

Figure 3.5: Slices through the sample at a frequency of 10 GHz for five simulated structures depicting B_{1z} (panels a), b) and e)) or B_{1x} (c) and d)) either 2 µm (panels a), b) and c)) or 20 nm below the stripline structure (d) and e)). A voltage of 2 V corresponding to 40 mW is applied to the coplanar stripline. The red rectangles depict the measurement area of structures a and b. The measurement area for structure c and d is situated beneath the short, whereas the measurement area for structure e is between the short and the additional contact in front of the short.

average B_1-amplitude of 0.58 mT can also be reached in the gap between the short and the contact. The corresponding conversion factor of 2.9 mT $\sqrt{\mathrm{W}}^{-1}$ should allow for 50 ns π-pulse times with a power of only 15 mW.

As expected, the simultaneous simulation of the electric field (data not shown) shows that it is smallest at the short where the magnetic field exhibits a maximum and the electric field has a node. Therefore, to reduce the influence of electric fields, the same close proximity of the short and the contact structure already deduced from the optimization of the conversion factor is desirable.

3.2.3 Sample holder

The sample holder fixes the sample mechanically and provides the interface from the coaxial microwave cable to the coplanar stripline geometry of the sample. It consists of a 640-µm-thick Rogers RO3010 microwave printed circuit board, which carries a 17-µm-thick copper sheet. The microwave transmission lines are defined from this sheet by photolithography and a subsequent etching process with a hydrochloric acid and hydrogen peroxide solution. To increase the mechanical stability, this substrate is glued to a thin fiberglass sheet with an epoxy-based adhesive. We discuss the basic components of the sample holder below. For imaging experiments, this basic design is adjusted so that it allows to route the microwave and gradient pulses through the different antennas on the sample.

All microwave-related parts of the sample holder transmission line are optimized so that they have an impedance of 50 Ω to reduce reflections. The basic sample holder geometry is sketched in figure 3.6. All transmission line traces are shown in a coppery color and bond wire connections are depicted with black lines. On the left side the sample holder starts with a Rosenberger 02K243-40ME3 connector (yellow outline), which connects the sample holder to the microwave line with a 2.92 mm connector. For the length of the center pin, the central coplanar waveguide (CPW) line is widened to ease soldering. In order to improve the microwave transmission this solder connection is thoroughly cleaned with acetone and isopropanol [98]. Afterwards, the CPW dimensions are tapered to the

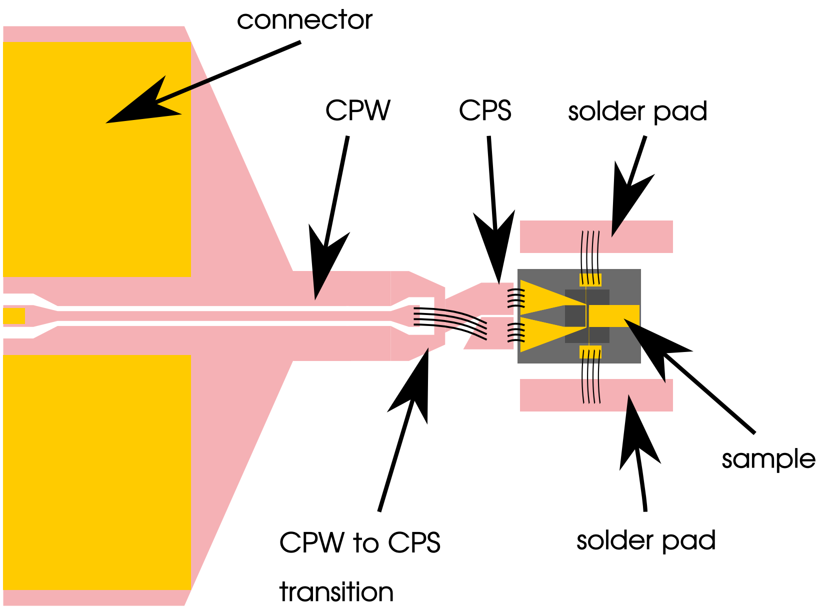

Figure 3.6: Schematic drawing of the sample holder used in this work. All transmission line traces are in a coppery color and the bond connections are shown with black lines.

dimensions which correspond to 50 Ω without the connector. For the optimization of the transmission line dimensions, including the connector center pin and solder, please see references 98 and 99. In order to change the transmission line geometry from a CPW to a coplanar stripline (CPS), we use a modified transition from reference 100. This CPS is connected to the sample with the help of at least four wire bond connections to ensure a good high frequency transmission [98] . Measured in a back-to-back configuration, this sample holder has less than 4.5 dB insertion loss for frequencies up to 18 GHz, which suggests a loss of less than 2.25 dB for an individual sample holder. The solder pads used for the photocurrent measurement provide the space for a solder joint of a thin wire and are connected to the sample with the help of wire bond connections.

3.2.4 Detection circuit

The current through the sample is amplified by a custom-built symmetric transimpedance amplifier (Elektronik Manufaktur Mahlsdorf) with switchable high (1 kHz, 5 kHz or 10 kHz) and low pass

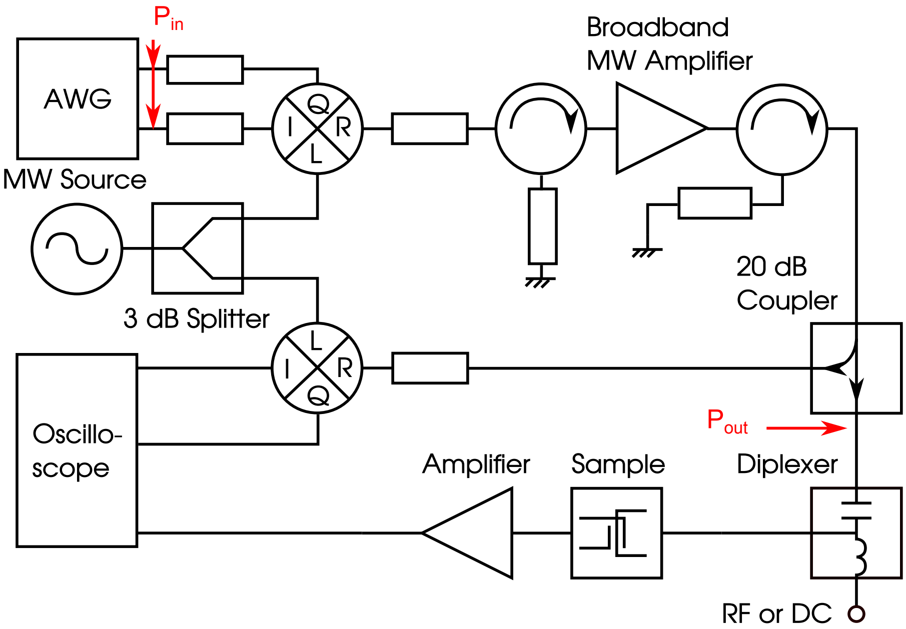

Figure 3.7: Microwave pulse generation setup consisting of an AWG for pulse generation, IQ mixers to convert the pulse from baseband to microwave frequencies, a broadband amplifier and an oscilloscope for pEDMR and pulse measurements.

filters (5 µs, 2 µs or <1 µs) and an amplification from $1 \cdot 10^4\,\mathrm{V\,A^{-1}}$ to $2 \cdot 10^7\,\mathrm{V\,A^{-1}}$. The resulting voltage is sampled by the oscilloscope (Agilent DSO9254A) and sent to the measurement computer for further processing.

3.2.5 Microwave pulse generation

There are two slightly different approaches to ESR spectrometers with pulse shaping capabilities in the literature [35, 88, 101, 102]. We use the approach of [101] where pulses are generated at an intermediate frequency of $\nu_{\mathrm{IF}} = 250\,\mathrm{MHz}$ and an IQ mixer is used as a single sideband upconverter. This method has the advantage that local oscillator (LO) leak-through with the frequency ν_{LO} can be set to a non-resonant frequency and that IQ mixer imbalances show up at $\nu_{\mathrm{LO}} - \nu_{\mathrm{IF}}$ (unwanted sideband) (c.f. section 3.1.2) which is chosen to be non-resonant, too. If it is not possible to choose a non-resonant frequency for those two unwanted effects, a calibration, e.g. with the method presented in [82] or by minimizing the ESR signal found at the frequencies of the LO or the unwanted sideband (c.f. section 3.3.2), reduces their magnitude significantly.

A schematic drawing of the microwave pulse setup is shown in figure 3.7. The AWG (Agilent 81180B, sample rate set to 4 GS s^{-1}) generates the in-phase and quadrature-phase parts of the pulse at an intermediate frequency of 250 MHz. The pulses are damped to suppress reflections and to adjust their power so that they do not drive the IQ mixer in the nonlinear regime when the AWG is at its maximum output power. Afterwards, the pulses are single-sideband-upconverted by an IQ mixer (Marki MLIQ0218L or Hittite HMC 009[2]) whose local oscillator (LO) port is fed by a microwave source (Agilent E8257D) through a -3 dB splitter (Marki PD0R618) for coherent up- and downconversion. The power of the upconverted pulses is adjusted so that the pulsed broadband gallium nitride microwave amplifier (Microsemi AML218P4011, saturation power P_{sat}=39 dBm for frequencies from 2 to 18 GHz) is used in its linear regime up to a nominal amplifier output power of P_{max} = 25 dBm (c.f. section 3.3.1). The isolators (MCLI IS-10, IS-19 and IS-29[3]) at the input and at the output of the broadband power amplifier suppress reflections. With the 20 dB coupler (Marki C20-0226) a small part of the pulse power is split off for coherent downconversion and pulse analysis. The pulses in the analysis path are damped to the IQ mixer input level and the downconverted pulses are recorded by an oscilloscope (Agilent DSO9254A, sample rate set to 4 GS s^{-1}). The bulk of the pulse power reaches a broadband diplexer (SHF DX-45) where the microwave pulses can be combined with radio frequency pulses or gradient pulses. These pulses are routed to the sample via a coaxial cable and the sample holder discussed above. To keep the effects of reflections on the impulse response minimal, all cables are as short as possible.

3.2.6 Radio frequency pulse generation

Although radio frequency (RF) pulses could be synthesized directly, a similar setup to the microwave pulse generation was used since

---

[2] Depending on the experiment. The Hittite mixer was used for all measurements in chapter 4, while the Marki mixer was used in all other experiments because of its larger LO bandwidth.

[3] The choice of isolator depends on the microwave frequency.

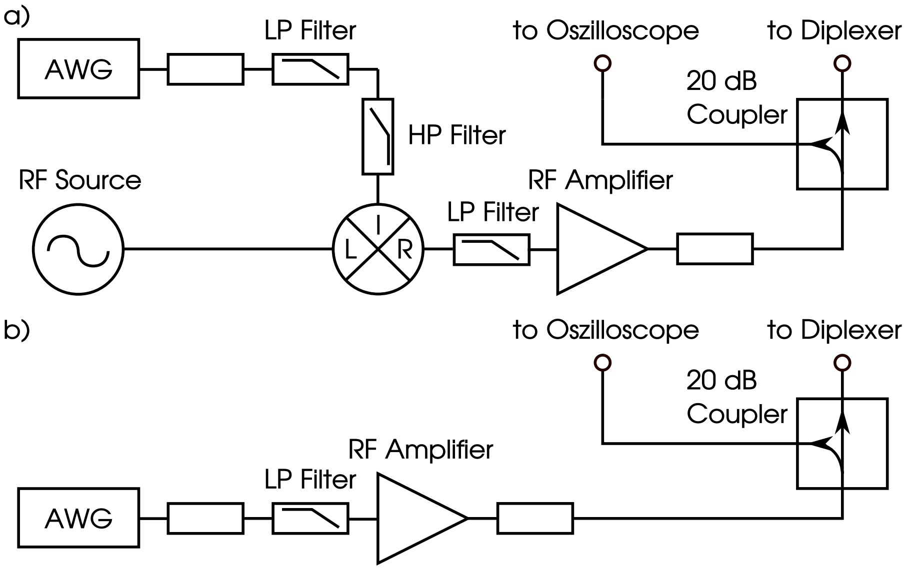

Figure 3.8: a) RF setup consisting of an AWG for pulse generation, a pulsed radio frequency source and a mixer to combine both pulses. The resulting RF pulses are low-pass-filtered to cut the unwanted sideband, amplified and damped to set the output power. A 20 dB coupler allows to measure the resulting pulse. b) Simplified RF setup consisting of an AWG for pulse generation, a pulsed RF amplifier and a 20 dB coupler for pulse measurements.

it enables frequency sweeps without pulse recalculations. This is necessary, because the AWG used for the RF setup (Chase DA14000) does not allow sequencing and the reprogramming of its memory takes up to a few seconds. In addition, this configuration allows to isolate the AWG output from the rest of the circuit by pulsing the radio frequency LO source output, which reduces the effect of noise generated by the AWG on the detection circuit during readout. Figure 3.8 a) shows this RF pulse setup. The NMR pulses, modulated with a frequency of 150 MHz for mixing with the RF local oscillator, are synthesized by the AWG (Chase DA14000, sample rate 4 GS s^{-1}), damped to set the pulse power and filtered (MiniCircuits SLP 200+ and SHP 50+) to suppress reflections and remove synthesization artifacts. Afterwards, the pulses are mixed with the pulsed radio frequency from the RF source (Agilent E4421B) yielding a pulse with the target frequency and a pulse in an unwanted sideband which is filtered by a low pass filter (MiniCircuits SLP 100+). A RF amplifier

(ENI 3200L) lifts the pulse power to 200 W which is subsequently damped to the desired pulse power. A 20 dB coupler (MiniCircuits ZFBDC20-61HP+ or ZFBDC20-62HP+) splits the RF into a path for pulse analysis and a path leading to the broadband diplexer. In the analysis path a further attenuator reduces the pulse power to safe levels for the oscilloscope.

With the use of a pulsed amplifier (TOMCO BT00250) and a AWG with faster waveform upload (PXDAC4800, sample rate $1.2\,\mathrm{GS\,s^{-1}}$) the RF pulse generation can be vastly simplified as is shown in figure 3.8 b). Here, the AWG directly synthesizes the RF pulses which are low pass filtered to remove discretization artifacts, damped to adjust the AWG output level to the RF amplifier input levels, amplified by the RF amplifier and damped again to adjust their power to the desired pulse power.

3.3 Calibration

The microwave components which make up the EDMR spectrometer are not ideal. At every connection between two components there are reflections due to e.g. impedance mismatch. Some of the components (e.g. IQ mixers, amplifiers) exhibit a nonlinear behavior through some parts of their operating range. The relation between the I and Q port of the IQ mixer may deviate in amplitude, the nominal 90° angle between I and Q and all the components in general may show a frequency-dependent behavior in their amplitude and phase response. All these effects influence the microwave pulses so that the pulse, which finally acts on the spins, may deviate from the intended pulse. In this section, these effects are examined and different solutions to mitigate their influence on the spin rotation are discussed.

3.3.1 Spectrometer nonlinearities

Power amplifier nonlinearities and their correction are an ongoing area of research in the field of telecommunication. There are many different methods to predistort signals to ensure a linear output of the amplifier [103–105]. The simplest method to circumvent

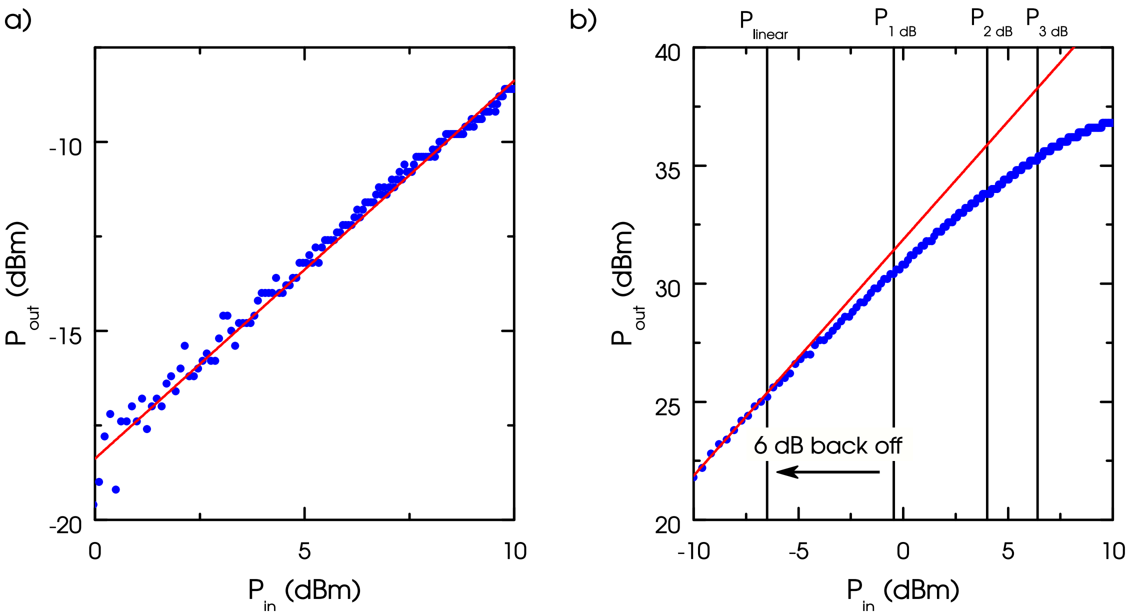

Figure 3.9: a) Power at the output of the IQ mixer as a function of the AWG output power for one channel. The red curve is a linear fit with a forced slope of 1. b) Power at the output of the power amplifier as a function of the AWG output power for one channel. The red curve is a linear fit with a forced slope of 1 and the black lines mark the P_{linear}, $P_{1\,\text{dB}}$, $P_{2\,\text{dB}}$ and $P_{3\,\text{dB}}$ points.

nonlinearities is to stay 6 dB below the 1 dB compression point of the power amplifier. This may seem rather excessive, but e.g. GaN-based microwave broadband power amplifiers are available up to output powers of 50 W and the stripline antennas used in this work have a high conversion factor. This allows us to employ this simple method to avoid nonlinearities.

In order to later operate the IQ mixers and the power amplifier in their linear region, we first measured the output power of the IQ mixers and the broadband amplifier with a calibrated microwave diode as a function of the AWG output power of one channel. Figure 3.9 shows the measurement results for the IQ mixer (panel a)) and the power amplifier (panel b)) in double logarithmic plots. In both cases, a linear fit with a slope of 1 is plotted in red.

The measurement and the linear fit in figure 3.9 a) match very well which implies that the IQ mixer is linear throughout the output region of the AWG. This is achieved by inserting 6 dB attenuators between the AWG and the IQ mixer I and Q ports, which basically perform a 6 dB power back-off so that the IQ mixer behaves linearly throughout the dynamic range of the AWG. The increased variance at low input powers can be accounted to the limited sensitivity of the oscilloscope.

For the nonlinearity measurement of the power amplifier a second amplifier was inserted between the IQ mixer and the power amplifier. This additional amplifier is operated in its linear region and allows us to drive the power amplifier into nonlinear operation. The power amplifier 1 dB compression point $\mathrm{P}_{1\,\mathrm{dB}}$ lies at an input power of −0.5 dBm. Therefore, according to the 6 dB back-off rule, the linear region should end around $P_{\mathrm{in}} = -6.5\,\mathrm{dBm}$, which is the case here. Therefore, up to an output power of about 25 dBm, the amplifier can be used without any nonlinear effects.

3.3.2 IQ mixer calibration

Apart from nonlinearities, which we avoid by the 6 dB back-off from the 1 dB compression point, the effects of LO leak-through and IQ imbalance, as discussed in section 3.1.2, deteriorate the output signal. They might be mitigated by the single sideband upconversion scheme employed to generate the microwave pulses in this work if the bandwidth of the pulses is below the intermediate frequency (c.f. section 3.3.2.2). Nevertheless, it is necessary to know the impact of IQ imperfections on the modulated and demodulated signal for the measurement of a system impulse response or for predistortion schemes. In the following sections, we will present different calibration processes for the IQ mixers either using pEDMR measurements, a spectrum analyzer or a single tone source and discuss their advantages as well as disadvantages.

3.3.2.1 Calibration with EDMR measurements

The LO leak-through and the IQ imbalances lead to additional frequency components at ν_{LO} and at $\nu_{\mathrm{LO}} - \nu_{\mathrm{IF}}$, respectively (c.f. section 3.1.2). This will result in additional pEDMR spectra at their corresponding magnetic fields. In order to measure these spectra, we

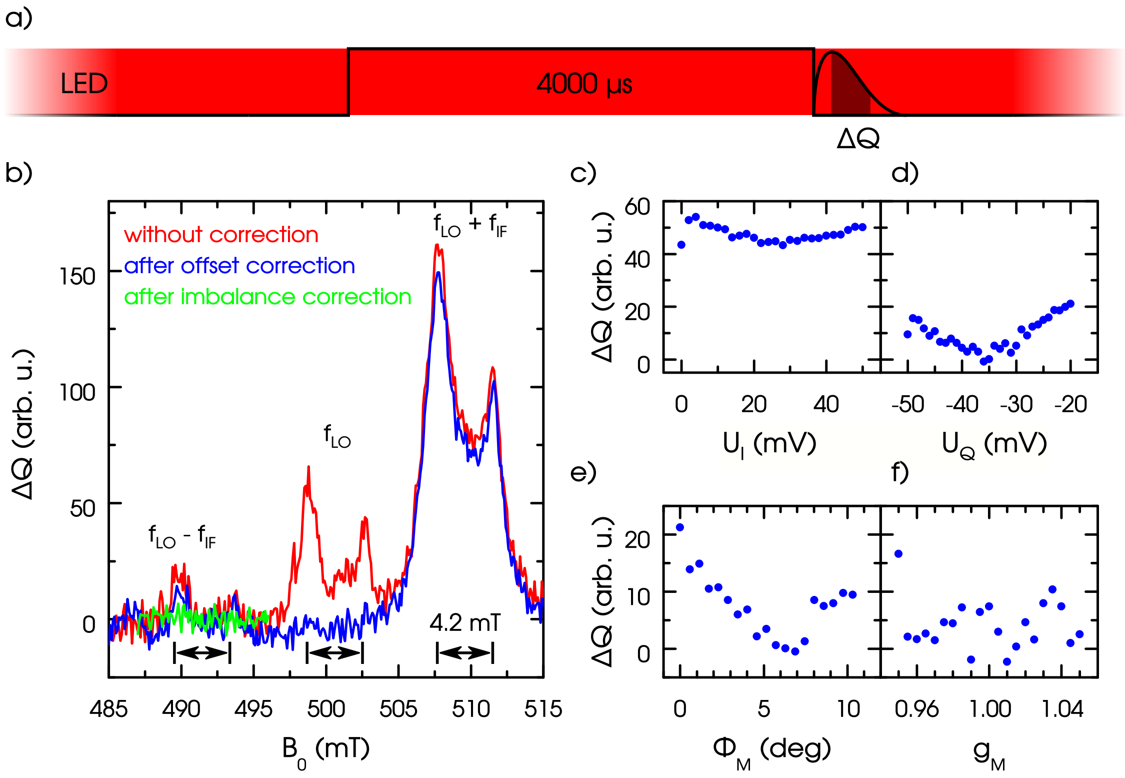

Figure 3.10: a) Pulse sequence employed during the optimization. b) pEDMR spectrum for an LO frequency of 14 GHz and an IF frequency of 250 MHz measured with microwave pulses with a length of 4000 µs before and after IQ imperfection calibration. For better visibility, we removed a linear background by subtracting a straight line. c) pEDMR signal amplitude for a magnetic field of 504.5 mT as a function of the I channel DC voltage with zeroed Q channel DC voltage. d) pEDMR signal amplitude as a function of the Q channel voltage using the optimal I channel voltage of 28 mV. e) pEDMR signal amplitude for a magnetic field of 492 mT as a function of Φ_M for $g_M = 0$. f) pEDMR signal amplitude as a function of g_M ($\Phi_M = 6.9°$).

used the pulse scheme depicted in figure 3.10 a). Here, the constant illumination increases the signal-to-noise ratio and the omission of a lock-in-scheme allows to measure the LO leak-through signal, which would be suppressed otherwise.

The contributions of the LO leak-through and the unwanted sideband are at least damped by 20 dB compared to the wanted sideband.

Therefore, we use a 4000-µs-long microwave pulse for a Rabi frequency of 30 MHz to enhance the pEDMR spectrum for the unwanted sideband and LO leak-through. Instead, to reduce the loss of signal due to T_2^*, an increased microwave power could be used to achieve shorter pulses whenever the sample allows it.

The measurements in this section were performed on a Marki MLIQ0218L mixer. The red curve in figure 3.10 b) shows a magnetic field sweep for $\nu_{\mathrm{LO}} = 14\,\mathrm{GHz}$ and $\nu_{\mathrm{IF}} = 250\,\mathrm{MHz}$. Apart from the desired pEDMR spectrum around 510 mT, highlighted by the 4.2 mT hyperfine line splitting of the two ^{31}P resonances, we see a spectrum with a reduced amplitude around 500 mT due to the LO leak-through and at 490 mT, which is caused by the IQ mixer imbalances. For the LO leak-through calibration the magnetic field is set to the most intense feature in that part of the spectrum and the DC offsets of the I and the Q channels are varied subsequently. To remove any microwave-induced background signals this measurement is repeated for two off-resonant fields and the resulting signal is subtracted by the linear interpolation of those off-resonant signals. Figure 3.10 c) shows the pEDMR amplitude at $B_0 = 499\,\mathrm{mT}$ as a function of the I channel bias U_{I} which has a clear minimum around a voltage of 28 mV. Using this bias voltage, the same experiment for the Q channel (c.f. figure 3.10 d)) yields a minimum of the pEDMR signal for a bias voltage of $U_{\mathrm{Q}} = -36\,\mathrm{mV}$. The pEDMR spectrum after this LO leak-through optimization (blue graph in figure 3.10 b)) does not exhibit any contribution due to the LO leak-through and a measurement with a spectrum analyzer indicates a reduction of the LO leak-through by 30 dB.

The same method can be applied to the IQ imbalances by sweeping Φ_{M} (c.f. figure 3.10 e)) and g_{M} (c.f. figure 3.10 f)) to minimize their contributions to the pEDMR spectrum. While the Φ_{M} sweep shows a minimum at $B_0 = 490\,\mathrm{mT}$ for an angle of $\Phi_{\mathrm{M}} = 6.9°$, the signal of the g_{M} sweep vanishes in the noise floor so that the pEDMR spectrum after imbalance correction (c.f. green curve in figure 3.10 b)) was measured with $g_{\mathrm{M}} = 1$. It does not show any contributions by IQ imbalances, as was the case for the LO leak-through optimization. A measurement with a spectrum analyzer shows a reduction of 40 dB. In contrast to the LO leak-through, depending on the severity of the imbalances, the contributions to the mirror image amplitude from g_M and Φ_M may not be independent [82]. Therefore, it might be necessary to record more than two sweeps to achieve a substantial reduction in the mirror image amplitude. Furthermore, if the skew between the I and the Q channels is high, Φ_M may strongly depend on the intermediate frequency so that it becomes necessary to determine g_M and Φ_M at two frequencies mirrored around ν_LO to determine the skew and repeat the optimization with an adjusted skew. This would result in at least nine measurements for the IQ imbalances and two measurements to optimize LO leak-through, which may not be feasible, if the signal-to-noise ratio of the sample is too low.

3.3.2.2 Calibration using a spectrum analyzer

If the signal-to-noise ratio of the sample is too low or a substantial skew between the I and the Q channels is present, the different frequency components of the microwave caused by the IQ imbalance and LO leak-through can be determined with a spectrum analyzer instead of the pEDMR measurements used in the previous section[4]. The measurements in this section were performed on the same Marki MLIQ0218L mixer. Figure 3.11 a) shows the microwave power as a function of the microwave frequency ν_C at the output of the uncalibrated IQ mixer (red), the IQ mixer calibrated by the pEDMR sweep method (blue) and the IQ mixer calibrated with the help of a spectrum analyzer (green). Similar to the previous section, the correction values are found by sweeping either the I and Q channel DC offset or Φ_M and g_M until their corresponding frequency contributions are minimal. The resulting suppression after the optimization is $-50\,\mathrm{dB}$ and $-65\,\mathrm{dB}$, respectively, which is significantly higher than the suppression achieved by the pEDMR calibration. To detect a skew between the I and the Q channel, this procedure is repeated for many intermediate frequencies ν_IF. Figure 3.11 b) plots Φ_M as a function of ν_IF (red dots). A linear fit of Φ_M has a slope of $m = 5.3\,^\circ\,\mathrm{GHz}^{-1}$, which corresponds to a skew of $15\,\mathrm{ps}$. This value is in between two possible skew correction steps of the AWG. Therefore, both values were tried and a correction value

---

[4] This measurement requires a suitable CW microwave output of the AWG.

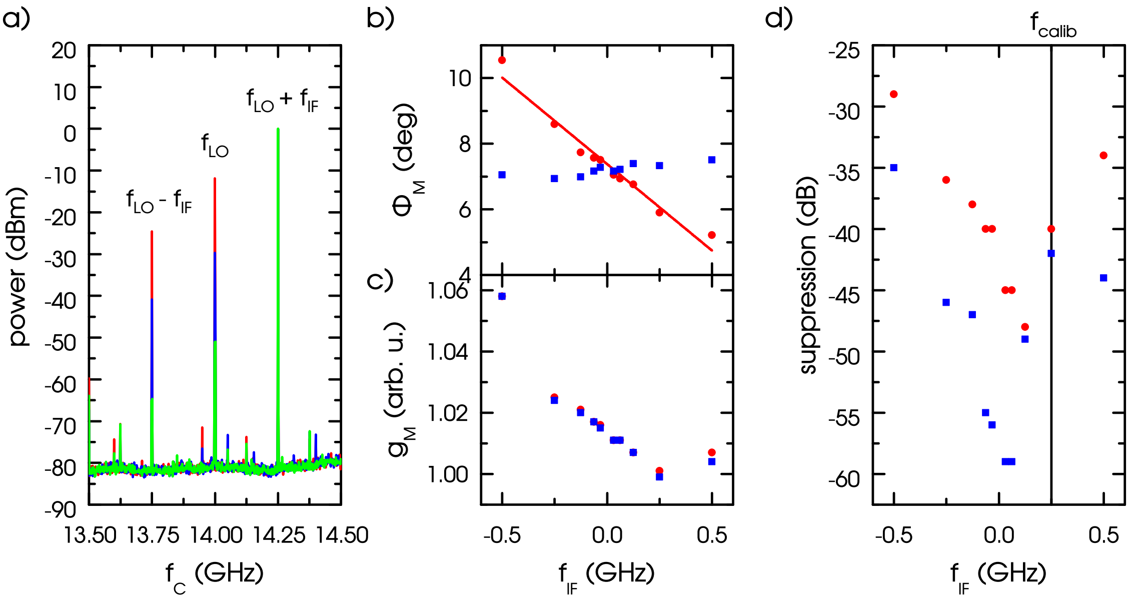

Figure 3.11: a) Microwave power as a function of the microwave frequency ν_C at the output of the IQ mixer without calibration (red), calibrated by the pEDMR sweep method (blue) and calibrated with the help of a spectrum analyzer (green). b) Φ_M as a function of the intermediate frequency before (red) and after (blue) skew correction. The linear fit which was used for the skew correction is plotted in red. c) g_M as a function of the intermediate frequency ν_{IF} before (red) and after (blue) skew correction. d) Suppression of the unwanted sideband as a function of the intermediate frequency using the values of g_M and Φ_M found with the pEDMR calibration (red) and for the median of g_M and Φ_M determined from panels b) and c) (blue). The intermediate frequency used in the pEDMR calibration f_{calib} is marked with the vertical black line.

of 10 ps was chosen, because it resulted in a virtually constant Φ_M throughout the IF frequency range (blue squares in figure 3.11 b)). The amplitude imbalance g_m (c.f. figure 3.11 c)) also depends on ν_{IF}, but does not depend on whether there is a skew correction (red dots) or not (blue squares).

Since adiabatic and optimum control pulses can span frequency ranges up to a gigahertz [35, 102], the quality of the IQ correction as a function of ν_{IF} is of interest. Figure 3.11 d) plots the sideband suppression as a function of ν_{IF} for the correction values found with pEDMR measurements (red dots) and for the median values $\Phi_\mathrm{M} = 7.19^\circ$ and $g_\mathrm{M} = 1.013$ (blue squares). The skew-corrected calibration outperforms the pEDMR-detected calibration for intermediate frequencies which are far away from the intermediate frequencies used for the pEDMR calibration (f_calib marked by the vertical black line). This is due to the omission of the skew-correction for the pEDMR measurements because of the amount of measurements necessary for this and has the effect that additional imbalance effects are generated by the skew. For pulses with a bandwidth around 100 MHz the difference is rather small so that a correction including the skew does not significantly improve the unwanted sideband suppression.

For the case without skew correction the sideband suppression varies between −48 dB and −40 dB for a pulse with a bandwidth of 250 MHz centered around $\nu_\mathrm{IF} = 125\,\mathrm{MHz}$. With the help of equation 3.13 we can estimate the amplitude variation of the wanted sideband in this region. Assuming that the total pulse power $P_\mathrm{total} = P_\mathrm{unwanted} + P_\mathrm{wanted}$ stays the same independent of ν_IF, equation 3.13 can be rewritten as

$$P_\mathrm{wanted} = \frac{P_\mathrm{total}}{1 + 10^{\frac{\mathrm{suppression}}{10}}}. \tag{3.34}$$

For better readability we denote the wanted sideband power for a suppression of −40 dB and −48 dB with $P_\mathrm{w}\,(-40\,\mathrm{dB})$ and $P_\mathrm{w}\,(-48\,\mathrm{dB})$, respectively. By dividing $P_\mathrm{w}\,(-40\,\mathrm{dB})$ by $P_\mathrm{w}\,(-48\,\mathrm{dB})$ we find for the power ratio $r_\mathrm{P} \approx 0.999\,92$. Since $P \propto B_1^2$ the B_1-ratio is $r_{B_1} = \sqrt{r_\mathrm{P}} \approx 0.999\,96$ and the variation of B_1 over the whole bandwidth is $4.2 \cdot 10^{-5}$. This is well below the 12 bit resolution of the AWG, which is at best $2.4 \cdot 10^{-4}$. Therefore, a skew correction is only necessary, if the pulse bandwidth centered around ν_IF exceeds $2\nu_\mathrm{IF}$ and the wanted and unwanted sidebands overlap.

3.3.2.3 Calibration using a single tone source

For impulse response measurements, which employ two IQ mixers for up- and downconversion, both IQ mixers have to be calibrated (c.f. section 3.3.3). The methods which have been discussed up till now only calibrate the upconverter, not the downconverter.

quantity	g_D	Φ_D	g_M	Φ_M
value	0.98	3.1°	0.99	3.8°

Table 3.1: Mean correction values for the demodulating and modulating mixers (Hittite HMC 009).

To calibrate the downconverter we chose the method presented in reference 82, which is briefly explained in section 3.1.2. To speed up these measurements, we wrote a software which automatically calibrates the receiver and the modulator for ν_{IF} between −500 MHz and 500 MHz, calculates the skew for both the modulator and the demodulator and finds the mean values for g_D, g_M, Φ_D, Φ_M and the I and Q channel DC offsets.

We will shortly present the results of this method using the example of modulating and demodulating Hittite HMC-009 mixers, which have a higher skew than Marki MLIQ0218L mixers used before and therefore show the effects of the calibration more clearly. Here, we find a skew of 60 ps for the demodulating IQ mixer and a skew of 40 ps for the modulating IQ mixer by fitting a linear function to the measured Φ_M and Φ_D values. The mean values for g_D, g_M, Φ_D and Φ_M are noted in table 3.1. This correction achieves a similarly high suppression in the pEDMR signal compared to the pEDMR detected method (data not shown) with the benefit of the additional skew correction for a measurement time of under a minute. The effects of the skew correction on the impulse response are discussed in section 3.3.3.

3.3.3 Spectrometer impulse response

Ideally, the system transfer function is measured from the AWG to the location of the spins. In reference 35 a pick-up coil in the stray field of the resonator is used for this purpose in a conventional EPR spectrometer. This pick-up coil is made with a standard coaxial microwave cable which has its outer conductor and isolation removed and its inner conductor soldered to the outer conductor. The impulse response of the pick-up coil and of the receiving hardware is assumed to be negligible and therefore it is ignored. The microwave transmission used in this work, which consists of a

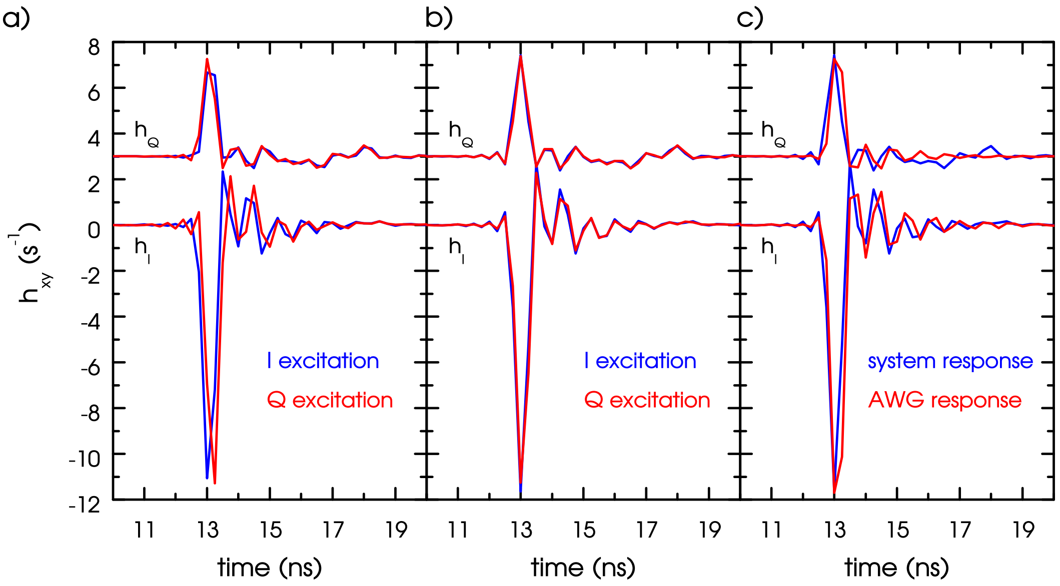

Figure 3.12: a) Impulse response of the system measured with an uncalibrated IQ mixer using a MLS excitation at the I port (blue lines) and the Q port (red lines). For all three panels, the h_Q part of the impulse response is shifted up by $3\,\mathrm{s}^{-1}$ compared to the h_I part. b) Impulse response of the system measured with a fully corrected IQ mixer using a MLS excitation at the I port (blue lines) and the Q port (red lines). c) Comparison of the system impulse response (blue lines) with the impulse response of the AWG only (red lines).

coaxial cable in the sample stick, the sample holder and the sample itself, is conceptually similar to the pick-up coil in reference 35. We have demonstrated that both the sample [97] and the sample holder [98] have very flat system responses over the frequency range up to 18 GHz. Therefore, we neglect the impulse response of the microwave transmission to the stripline short, too, and measure the impulse response from the AWG through the microwave setup to the oscilloscope via a 20 dB coupler (c.f. figure 3.7). The IQ mixers (Marki MLIQ0218L or Hittite HMC 009) and the oscilloscope (Agilent DSO9254A) both have a bandwidth of 3.5 GHz per channel, which is much larger than the 1 GHz bandwidth per channel of the AWG, and are ignored for this reason.

Figure 3.12 a) plots the in-phase $h_I(t)$ and quadrature-phase $h_Q(t)$ components of the passband impulse response measured with the

MLS method without IQ mixer calibration. As described in section 3.1.5, we can use an excitation at the I port while the Q port is terminated and vice versa to redundantly measure the impulse response. The blue lines in figure 3.12 show the impulse response obtained with an MLS excitation at the I port, while the red lines show the impulse response for a MLS excitation at the Q port. We again use a Hittite HMC 009 mixer for up- and downconversion, because the larger skew allows us to see the effects of an uncalibrated IQ mixer more clearly. The main part of the impulse response resides in $h_\mathrm{I}(t)$ which has a rise time of 0.4 ns, a full width at half maximum of also roughly 0.4 ns and is fully decayed after about 5 ns. Both $h_\mathrm{I}(t)$ and $h_\mathrm{Q}(t)$ show a time shift between the graphs for the I excitation and the Q excitation. By comparing the rising and the falling flanks we find shifts of about 60 ps and 100 ps for $h_\mathrm{Q}(t)$ and $h_\mathrm{I}(t)$, respectively. These shifts have the same order of magnitude as the combined baseband skew found in section 3.3.2.3. The situation is significantly improved by the IQ mixer calibration discussed in section 3.3.2.3 as can be seen in figure 3.12 b). Here, the impulse responses measured with I and Q excitation agree very well for $h_\mathrm{I}(t)$ and $h_\mathrm{Q}(t)$. If a Marki MLIQ0218L mixer is used instead of the Hittite HMC 009 mixer for up- and downconversion, the skew correction is not necessary due to its much lower skew (c.f. section 3.3.2.2).

To elucidate the cause of this impulse response, we measured the impulse response of the AWG directly connected to the oscilloscope. This results in a purely in-phase impulse response since there is no physical connection between the I excitation and Q detection and vice versa. To compare this impulse response to the measurement from figure 3.12 b) it was rotated in the complex plane by an angle of 160°. Figure 3.12 c) shows the resulting impulse response after the rotation (red lines) together with the impulse response from figure 3.12 b) (blue lines). Apart from minor differences during the decay and differences due to a shift of the discretization caused by the different run-times of the signal, they are very similar. Therefore, the impulse response of the whole microwave system is dominated by the impulse response of the AWG and cannot be substantially improved without exchanging the AWG.

We will discuss the effects of this impulse response on the optimal control pulses used in this thesis in detail in chapter 5. However, the fact that the impulse response has decayed completely after about 8 ns implies that pulses which have a bandwidth well below 125 MHz should not be affected. A Fourier transformation of the impulse response reveals a total bandwidth of about 2 GHz.

4

Broadband pulse shaping capabilities of the setup

In this chapter we test the capabilities of the EDMR setup for arbitrarily shaped pulses. The ability to generate and deliver shaped pulses in the frequency range of 2 GHz to 18 GHz is evaluated with pEDMR sweeps of Gaussian pulses in section 4.1. Afterwards, we perform Rabi measurements on different stripline structures, compare the fabricated structures with the simulation and identify the most promising stripline structure for subsequent experiments (section 4.2). To further test the pulse shaping capabilities, we use the BIR-4 pulse to improve the fidelity of rotations up to 2π (section 4.3) and implement a fully adiabatic electron nuclear double resonance experiment (section 4.4). This chapter is based on reference 96.

4.1 Broadband capabilities

We first investigate the broadband capabilities of the microwave antennas via Gaussian pulses exhibiting good selectivity [106]. The full pulse sequence used for this is shown at the top of figure 4.1. The illumination via a light-emitting diode (LED) is depicted in red and the Gaussian microwave pulse is shown in black. The EDMR response in the form of the charge ΔQ is obtained through boxcar integration over the current transient after the pulse [5, 49].

Figure 4.1 depicts EDMR spectra for pulse frequencies ν_{MW} from 2.5 GHz to 17.5 GHz in steps of 1 GHz measured with a single Gaussian pulse with a standard deviation of 60 ns truncated symmetrically to a total pulse length of 400 ns, which results in a FWHM of 32 MHz in the frequency domain. The ordinate displays the normalized charge ΔQ while the static magnetic field B_0 shifted by $(h\nu_{\mathrm{MW}})\,/\,(g_{\mathrm{P}}\mu_{\mathrm{e}})$ with Planck's quantum h and the Bohr magneton μ_{e} is plotted on the abscissa. This allows a direct comparison of the hyperfine-split ^{31}P electron resonances at different microwave frequencies, because they remain at a magnetic field of ±2.1 mT (vertical red lines) in this representation. In contrast, the resonances corresponding to the different orientations of the dangling bond readout partner Pb_0 (green and blue line) seem to move with increasing microwave frequency due to their slightly different g-factors. Figure 4.1 clearly demonstrates that pulsed EDMR spectra can be obtained with the antenna structures studied here over the whole range of microwave frequencies between 2 GHz and 18 GHz compatible with the broadband microwave power amplifier. All spectra show a similar signal-to-noise ratio.

4.2 Performance comparison of broadband antennas

In order to experimentally verify the conversion factors of the different antenna structures introduced in section 3.2.2 and to compare them to the simulations, Rabi experiments with square microwave pulses have been performed on the high field phosphorus resonance for all structures. The microwave power in each case was set so that the length of each π-pulse is about $T_\pi = 50\,\mathrm{ns}$ corresponding to a B_1 of about 0.35 mT. Since the total pulse times are short compared to the T_2 of the system [47], the Rabi experiments have been performed under constant illumination. The corresponding pulse sequence is shown in figure 4.2 together with the results obtained on structures

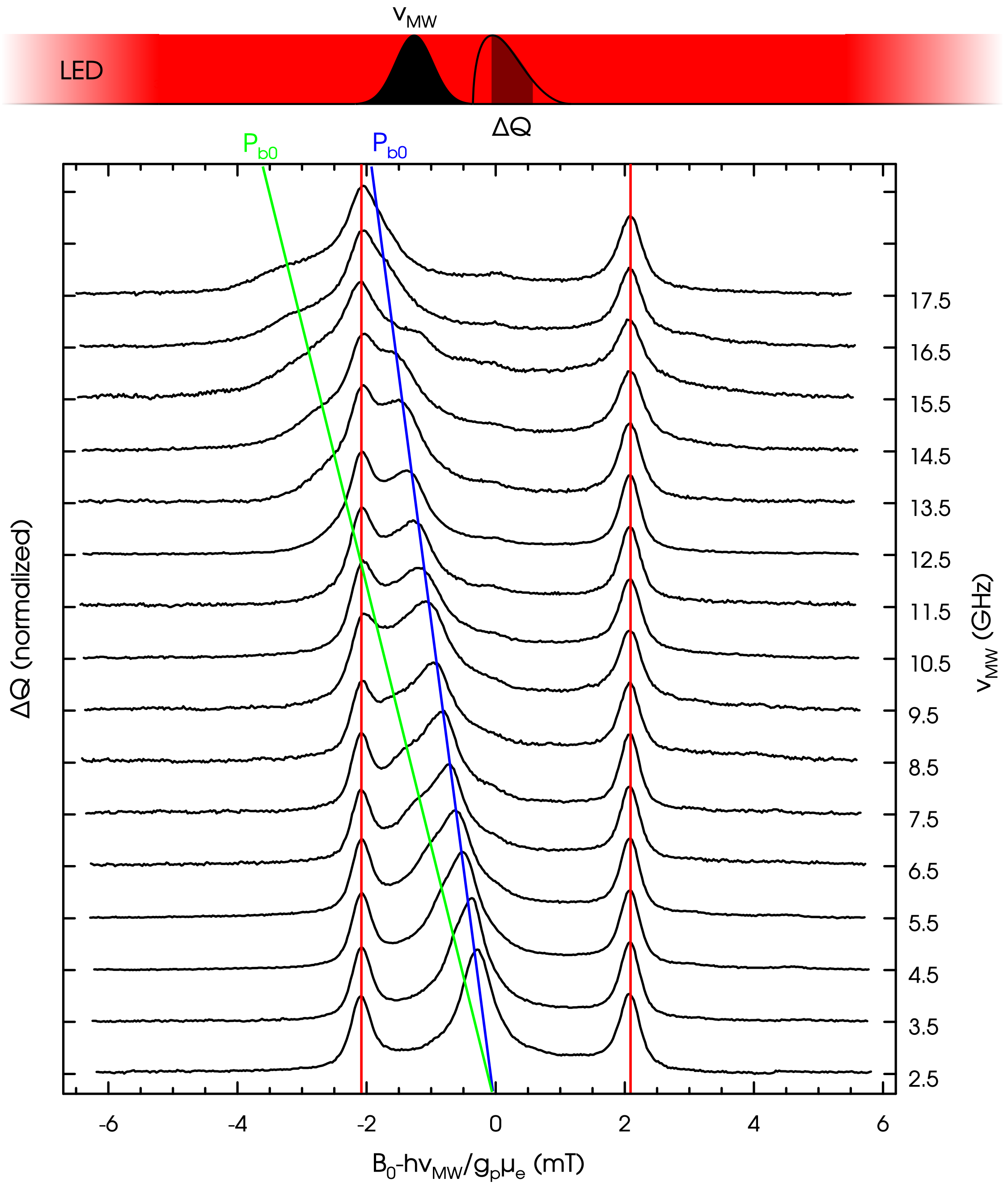

Figure 4.1: Broadband pulsed EDMR spectra of Si:P for microwave frequencies from 2.5 GHz to 17.5 GHz. The EDMR signal intensity ΔQ is plotted versus the magnetic field B_0 shifted by $(h\nu_{\mathrm{MW}})\,/\,(g_{\mathrm{P}}\mu_{\mathrm{e}})$ to align the spectra with respect to the ^{31}P resonances for different frequencies. The red lines mark the hyperfine-split phosphorus resonances, the blue and green lines follow the two dangling bond resonances observed for the sample oriented with [110] parallel to B_0.

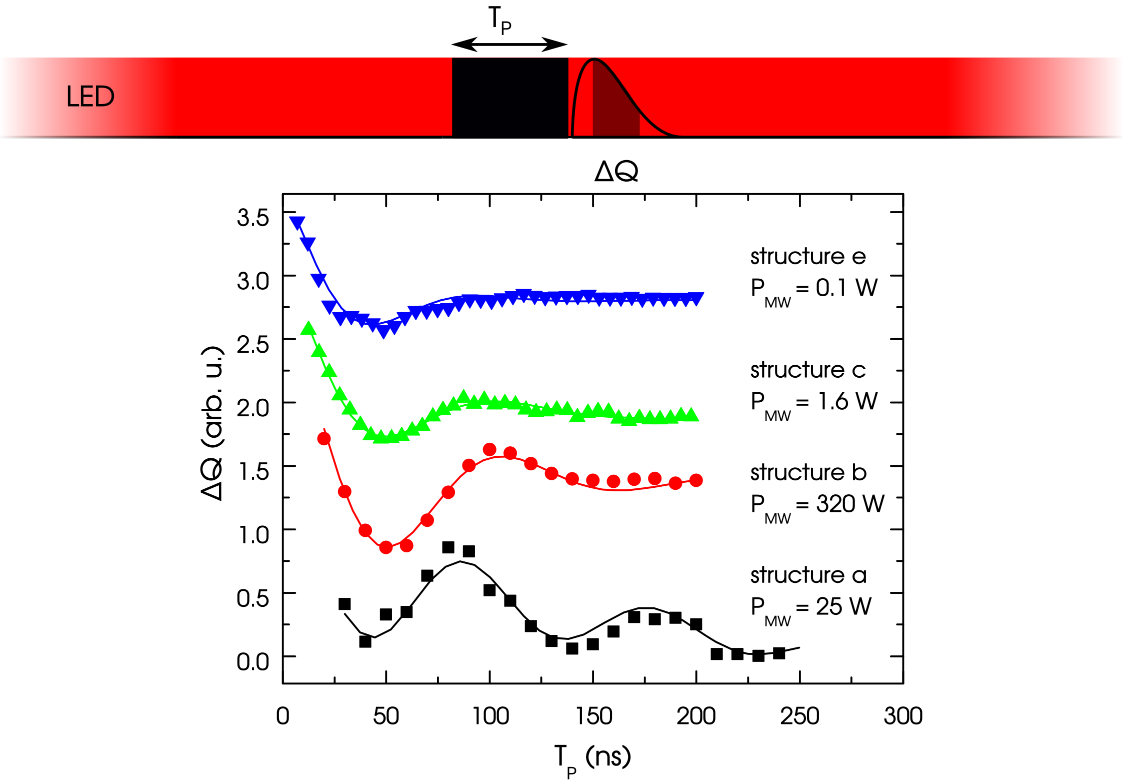

Figure 4.2: Square-pulse-driven Rabi oscillations for structures a, b, c and e measured by EDMR with continuous illumination of the sample at a microwave frequency of 9 GHz for structures a and b and 6.5 GHz for structures c and e. The normalized EDMR signal intensity ΔQ after the MW pulse is plotted versus the pulse length T_p.

a, b, c and e where the EDMR signal intensity ΔQ is plotted as a function of the length T_P of the pulse. The data for each structure are fitted with

$$y = A_\mathrm{Rabi} \cdot \cos\left(\frac{2\pi}{T_{2\pi}} \cdot T_\mathrm{p}\right) \cdot \exp\left(-\frac{T_\mathrm{p}}{\tau_\mathrm{deph}}\right) + y_0, \tag{4.1}$$

with the Rabi oscillation period $T_{2\pi}$ and the dephasing time τ_deph. This corresponds to a Lorentzian distribution of the B_1-fields under the assumption that the g-factor distribution is small in comparison with the B_1-inhomogeneity and can be neglected. The half width at half maximum of the B_1-distribution can then be calculated as $\Delta B_1 = \hbar/(g\mu_\mathrm{e}\tau_\mathrm{deph})$. Used microwave powers P_MW, Rabi oscillation periods $T_{2\pi}$, the relative dephasing times $\tau_\mathrm{deph}/T_{2\pi}$,

structure	a	b	c	e
P_{MW} [W]	25	320	1.6	0.1
$T_{2\pi}$ [ns]	91	112	113	102
$\tau_{\mathrm{deph}}/T_{2\pi}$	1.44	0.50	0.35	0.30
$\Delta B_1/B_1$	0.11	0.32	0.46	0.59
$B_1/\sqrt{P_{\mathrm{MW}}}$ $\left[\mathrm{mT}/\sqrt{\mathrm{W}}\right]$	0.08	0.02	0.25	1.09

Table 4.1: Microwave powers, Rabi oscillation periods, relative dephasing times, B_1-field inhomogeneities and conversion factors obtained from the Rabi oscillations in figure 4.3 a) for structures a, b, c and e.

relative B_1-inhomogeneities $\Delta B_1/B_1$ and the conversion factors $B_1/\sqrt{P_{\mathrm{MW}}}$ are listed in table 4.1 for the four antennas.

Only structures c and e exhibit a large enough conversion factor to generate π-pulses which are shorter than the T_2^* of our spin ensemble when using the 10 W broadband amplifier. For the use of the other structures, more powerful amplifiers such as traveling wave tube amplifiers are necessary. The relative increase of conversion factors from structure b to structures c and e are predicted very well by the simulation (c.f. section 3.2.2.2), although all measured conversion factors are roughly 9 dB lower than the simulated factors. A factor of 3 dB can be attributed to the microwave lines leading to the sample. The remaining difference of 6 dB might stem from the assumption of perfect electric conductors for the simulated microwave structure, from the fact that no substrate conductivity was included in the simulation and from reflections at the bond connection between sample holder and sample. In contrast to this, structure a deviates from this scheme with a measured conversion factor that is equal to the simulated conversion factor if the microwave lines are considered. The minimum relative B_1-inhomogeneity of ±11 % calculated from the fit is big compared to the relative B_0-inhomogeneity of about ±0.1 % resulting from the linewidth [58] so that the assumption taken in equation 4.1 is warranted. A B_1-inhomogeneity of ±5 % as calculated for structures a and b should at least result in a $\tau_{\mathrm{deph}}/T_{2\pi}$ of 3.2. Both structures a and b do not quite reach this value with measured values of $\tau_{\mathrm{deph}}/T_{2\pi} = 1.44$

(structure a) and 0.5 (structure b). The same difference is found for structure c, where the measured $\tau_{\mathrm{deph}}/T_{2\pi} = 0.35$ is smaller than the predicted ratio of 1.6. For structure e, where the measured and calculated ratios for $\tau_{\mathrm{deph}}/T_{2\pi}$ are 0.30 and 0.32, respectively, perfect agreement is found. This behavior might be caused by the omission of the measurement structures in the simulation of structures a, b and c in contrast to that of structure e, where the microwave delivery itself is used as measurement structure. Since structure e allows to reduce the pulse power to such an extent that the broadband amplifier can even be used in its linear region (c.f. section 3.3.1), all further measurements in chapters 4 and 5 are performed with structure e.

4.3 Pulse shaping capabilities

Using the fit to the Rabi oscillations of structure e we can estimate the negative impact of the dephasing on the modulation depth. At the end of a π-pulse, the modulation depth $\exp\left(-T_{\mathrm{p}}/\tau_{\mathrm{deph}}\right)$ is already reduced to 16 % while the modulation depth for a 2π-pulse is a mere 2.4 % of the initial EDMR signal intensity. To circumvent the observed effects of the inhomogeneity we use the BIR-4 pulse described in section 2.5.1.2. We use a pulse time T_{p} of 400 ns for each adiabatic half passage at an amplitude $B_{1,\mathrm{max}}$ of 1.4 mT (the maximum amplitude which can be generated avoiding non-linearities) and a frequency sweep amplitude $\Delta\omega_{\mathrm{max}}$ of $2\pi \cdot 25$ MHz. Due to an increased T_2 of the donor electron spin in the dark in our samples, the EDMR experiment is conducted using pulsed light. To increase the signal-to-noise ratio, the lock-in technique, where sequences with resonant pulses (frequency ν_{on}) and with off-resonant pulses (frequency ν_{off}) follow each other and are subtracted from one another, is used (c.f. section 2.3). With $\kappa = 0.6$ and $\zeta = 1.45$, which were found by maximizing the adiabaticity η (c.f. section 2.5.1) for each half passage, we find a maximum adiabaticity of $\eta = 136$. This adiabaticity is extremely high compared to e.g. the adiabaticity which already yields good results in our ENDOR experiments (c.f. section 4.4) and suggests that the pulse here uses either a higher than necessary B_1 or a pulse length which is longer than needed.

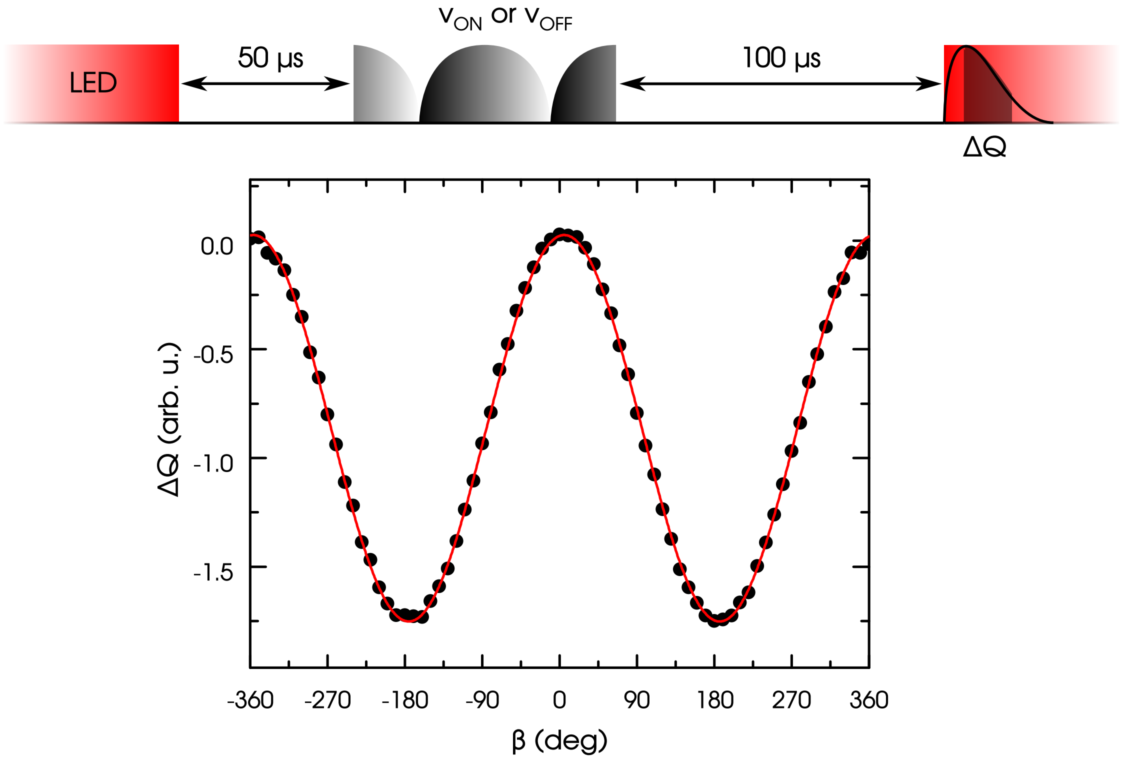

Figure 4.3: Effect of a BIR-4 pulse on the EDMR signal ΔQ as a function of the rotation angle β. The pulse sequence used for the study of the BIR-4 universal rotation is plotted on top. The microwave is applied in the dark, the EDMR is measured during the transient induced by the optical refill pulse. The red line depicts the expected dependence of the EDMR signal intensity ΔQ for a BIR-4 pulse with varying β.

Since B_1 is dictated by the linewidth of the resonance (c.f. section 2.5.1.2), shorter pulses, e.g. with $T_p = 200\,\mathrm{ns}$, can be built (c.f. section 5.3). The full pulse sequence is shown in figure 4.3 where the microwave amplitude evolution during the pulse is again depicted by the amplitude and the frequency evolution through the brightness gradient.

Figure 4.3 plots the measured ΔQ as a function of the rotation angle β of the BIR-4 pulse. The measured data is fitted with $\Delta Q = A_{\mathrm{BIR4}} \cdot \cos\beta$ which is the expected angular dependence of the ^{31}P-Pb$_0$ pair recombination on the rotation or rather nutation angle of one of the spin pair constituents. The EDMR amplitude when using the

BIR-4 sequence in figure 4.3 is the same as the one determined via a fit to equation 4.1 for the square-pulse-driven Rabi oscillations of the same structure e in figure 4.2. Therefore, within the errors of the fits, the BIR-4 pulse is able to achieve arbitrary rotations from -2π to 2π for the whole spin ensemble, effectively removing the drawbacks of B_1-inhomogeneity from the broadband samples.

4.4 ENDOR capabilities of the system

To further demonstrate the broadband capability of the delivery system we turn to electron nuclear double resonance experiments (ENDOR), using the same antenna and adiabatic pulses for the excitation of the ESR as well as the NMR transitions. We apply a modified Davies ENDOR sequence for EDMR [107] based on the difference between the lifetimes of the parallel (τ_p = 1 ms) and the antiparallel (τ_ap = 16 µs) [5]) state of the phosphorus-dangling bond spin pair to generate a polarization of the ionized nuclear donors. The pulse sequence, which was adapted to use adiabatic full passage pulses for both the ionization and the readout, is shown in figure 4.4 a). RF pulses are depicted by amplitude- and frequency-modulated sines. For the following discussion we will focus on the high-field hyperfine-split phosphorus electron spin resonance with a nuclear spin quantum number of $m_I = -\frac{1}{2}$ labeled ν_PH in figure 4.4 b). (The experiment would work the same way if performed on the $m_I = +\frac{1}{2}$ resonance ν_PL.)

At the start of the experiment, the light is switched off and during the following 50 µs the charge carriers in the bands recombine and the current through the sample settles to zero. All antiparallel donor/dangling bond spin pairs recombine as well. An adiabatic full passage pulse on the $m_I = -\frac{1}{2}$ resonance transforms the remaining donor/dangling bond spin pairs with parallel spin orientation and a $m_I = -\frac{1}{2}$ of the phosphorus nucleus into the short-lived antiparallel state. For the next 100 µs these spin pairs also recombine leading to an ensemble of ionized nuclear spins initialized to the $m_I = -\frac{1}{2}$ state (c.f. figure 4.4 c)). Now, NMR on the ionized ensemble can be performed (c.f. figure 4.4 d)) and will lead to a net polarization of all donor nuclear spins depending on the rotation angle of the

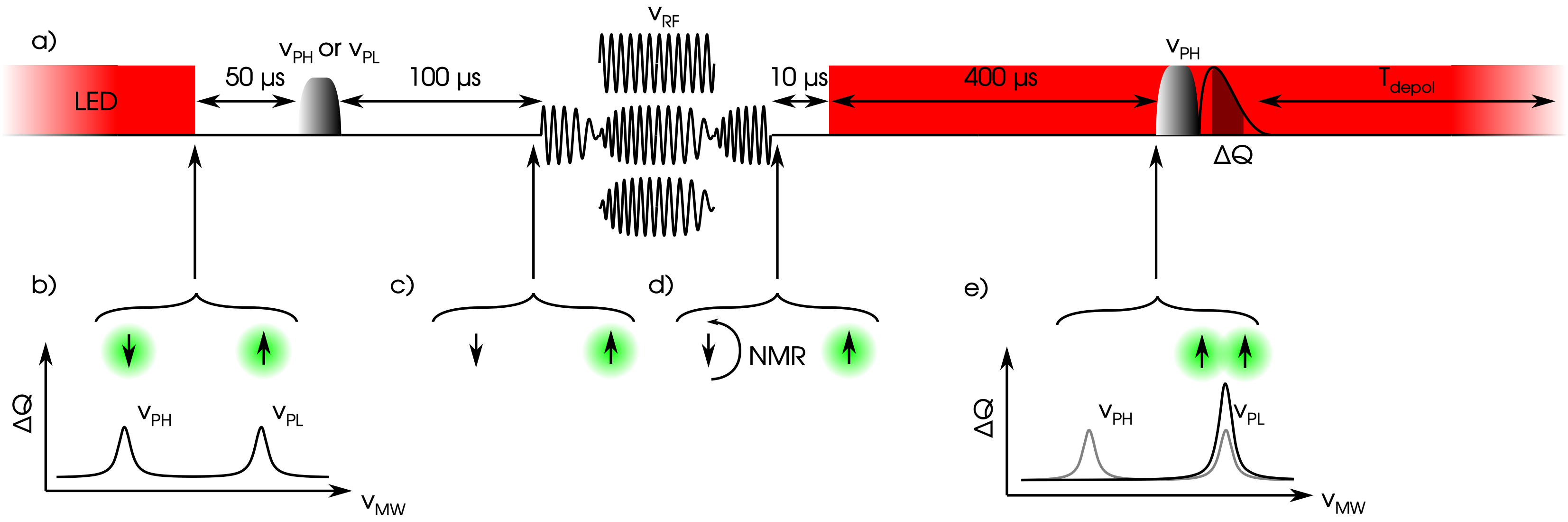

Figure 4.4: a) Modified EDMR Davies ENDOR sequence using adiabatic full passage pulses. RF pulses are depicted by amplitude- and frequency-modulated sines. b) Idealized EDMR spectrum of hyperfine-split phosphorus donors as a function of the microwave frequency at the time where the illumination is switched off. The spin state of the nucleus is depicted by the black arrow, which is surrounded by the green cloud symbolizing the donor electron attached to the donor. c) State of the nuclear spin ensemble after the ESR full passage donor ionization pulse and a waiting time of 100 µs. The nuclear spin ensemble corresponding to the high-field ^{31}P resonance is ionized, which is depicted by the absence of the green cloud. d) The NMR pulse transforms all ionized donors. e) Idealized EDMR spectrum after all donors have been refilled with charge carriers. The gray line depicts the pre-sequence situation.

NMR pulse. Thereafter, the light is switched on for 400 µs to allow the recapture of charge carriers at ionized donors [5]. With the full passage ESR readout pulse, the population of the $m_I = -\frac{1}{2}$ state is measured (c.f. figure 4.4 e)). After the readout pulse, the experiment is paused for the time T_{depol} to allow for the light-induced depolarization of the generated nuclear spin polarization, which takes about 100 ms [108].

EDMR relies on the symmetry of a spin pair for its high sensitivity. However, this leads to strong nuclear hyperpolarization [108], which makes the analysis of the effects of adiabatic pulses in ENDOR somewhat difficult. If the ionization pulse is switched between the $m_I = -\frac{1}{2}$ and the $m_I = +\frac{1}{2}$ resonances at every other sequence while the readout pulse is kept on the $m_I = -\frac{1}{2}$ resonance, the generated polarization should switch between the $m_I = -\frac{1}{2}$ and $m_I = +\frac{1}{2}$ nuclear spin states, resulting in an alternation of ΔQ which can be used for lock-in detection. While this lock-in signal will still exhibit some polarization effects, the polarization now mostly depends on the fidelity of the RF pulse and therefore allows for at least qualitative comparisons between different pulses without the need of a light-induced reset of the nuclear polarization.

All measurements in this section were performed at a B_0-field of 234.75 mT, which allows us to address both the high-field and the low-field ^{31}P resonance (c.f. figure 4.1). This B_0 results in the microwave frequencies $\nu_{\mathrm{PH}} = 6.5\,\mathrm{GHz}$ and $\nu_{\mathrm{PL}} = 6.617\,\mathrm{GHz}$. We use a power of 50 mW for all RF pulses. Figure 4.5 depicts nuclear Rabi oscillations driven by square RF pulses with a frequency of 4.0246 MHz after the MW ionization pulse. The measurement was performed using the lock-in technique discussed in the last paragraph with a T_{depol} of 2 ms. The ENDOR signal intensity ΔQ is plotted versus the length T_{p} of the RF pulse. Since the polarization effects distort the Rabi oscillation, equation 4.1 cannot be used to fit the data in a satisfying way. The red line in figure 4.5 therefore is a fit of equation 4.1 to the data using $\tau_{\mathrm{deph}}/T_{2\pi}$ from the electron Rabi measurements of structure e. Assuming that the maximum in figure 4.5 at 100 µs corresponds to a π-pulse, we find a B_1-field of 0.29 mT and obtain a conversion factor of $1.3\,\mathrm{mT}\,\sqrt{\mathrm{W}}^{-1}$ close to the conversion factor for the microwave frequencies of $1.1\,\mathrm{mT}\,\sqrt{\mathrm{W}}^{-1}$. The dephasing of the nuclear Rabi oscillation is qualitatively similar

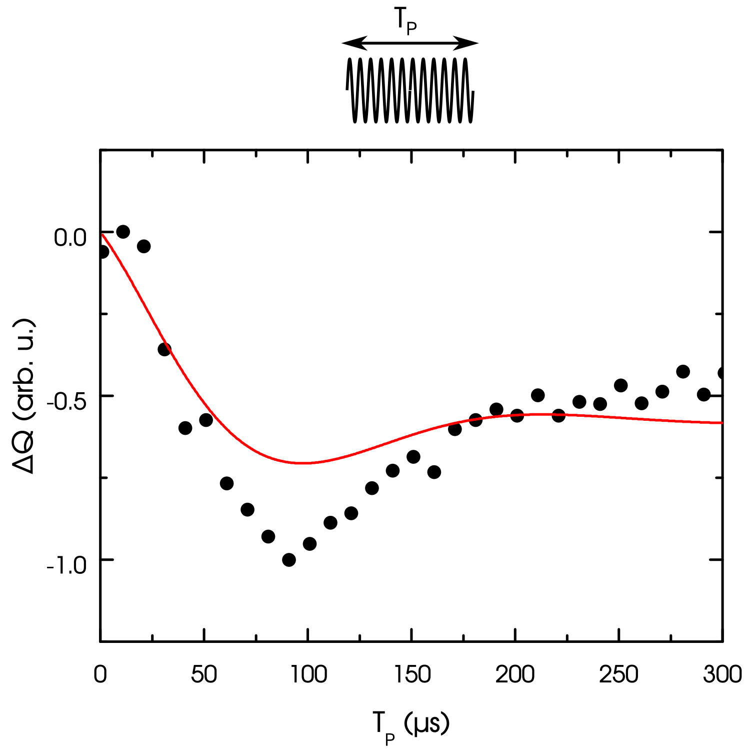

Figure 4.5: Square-RF-pulse-driven nuclear Rabi oscillation for an RF power of 50 mW. The red line is a fit to the data using the dephasing times obtained from the electron Rabi oscillations shown in figure 4.2 a).

to the electron case, which is to be expected, because the same antenna and donor/dangling bond ensembles were used.

In figure 4.6 a) the ENDOR signal intensity ΔQ, measured using the lock-in technique with a T_{depol} of 2 ms, is plotted versus the center frequency υ_{RF} of an adiabatic full passage NMR pulse which is concatenated from two adiabatic half passages described in equations 2.25 and 2.26. For the adiabatic full passage the parameters $\kappa = 0.62$ and $\zeta = 8.6$, found by optimizing the adiabaticity for a frequency sweep amplitude $\Delta\omega_{\mathrm{max}} = 2\pi \cdot 8.6\,\mathrm{kHz}$ and a pulse length of 100 µs per adiabatic half passage, were used. With $B_{1,\mathrm{max}} = 0.29\,\mathrm{mT}$ this results in an adiabaticity of $\eta = 2.2$.

To test the dependence of the full passage amplitude on the adiabaticity, ENDOR spectra using full passage pulses where the adiabaticities were varied by changing κ and ζ have been recorded.

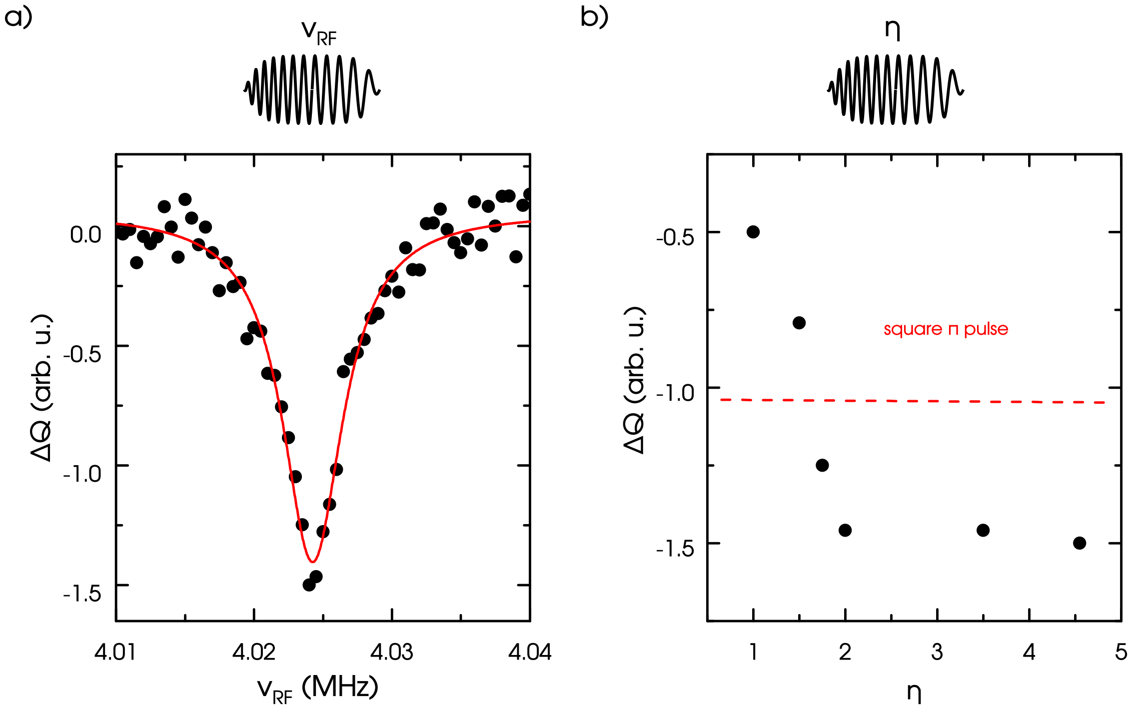

Figure 4.6: a) ENDOR spectrum using an adiabatic full passage NMR pulse as indicated on the top. b) ENDOR signal amplitude ΔQ for adiabatic full passage pulses with different adiabaticities η. The dashed red line indicates the ENDOR ΔQ for a 100 µs-long square RF pulse.

The maximum ENDOR amplitude ΔQ plotted versus the adiabaticity is shown in figure 4.6 b). The red horizontal line depicts the performance of a square π-pulse from figure 4.6 a). As can be seen from figure 4.6 b), for adiabaticities higher than 2, ΔQ saturates. Compared to a rectangular π-pulse, the signal intensity is increased by a factor of 1.5.

As was the case for the electrons, we also concatenated four adiabatic half passages to form BIR-4 RF pulses to realize universal rotation pulses for the nuclear spin. The length of each half passage was 400 µs and we used the parameters $\kappa = 1.09$ and $\zeta = 8.61$ which were optimized for a pulse time of 400 µs and a sweep width of $\Delta\omega = 2\pi \cdot 8.4\,\mathrm{kHz}$ at a $B_{1,\mathrm{max}} = 0.29\,\mathrm{mT}$ resulting in an adiabaticity factor of $\eta = 13$. Compared to the BIR-4 pulse on the ESR resonances, the required power is much smaller due to the small NMR linewidth of

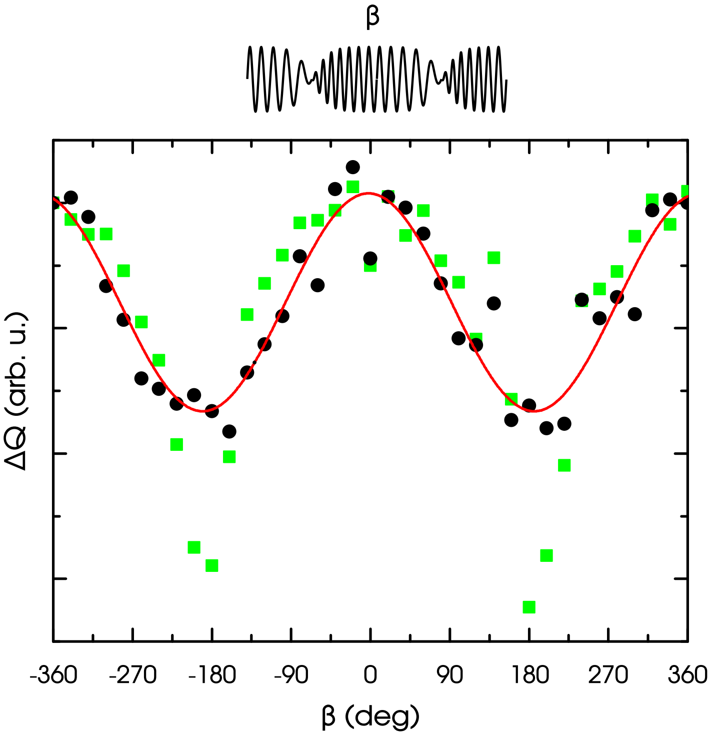

Figure 4.7: ENDOR signal ΔQ as a function of the rotation angle β of a BIR-4 pulse for depolarization times T_{depol} of 2 ms (green rectangles) and 100 ms (black dots). The expected dependence of the EDMR signal on the rotation angle β is shown in red.

290 Hz [107]. Similar to the nuclear Rabi measurements, the lock-in-detected BIR-4 pulse shows polarization when short relaxation times $T_{\mathrm{depol}} = 2$ ms are used (c.f. green squares in figure 4.7, which shows the ENDOR signal ΔQ as a function of the rotation angle β of the BIR-4 pulse). By increasing the time T_{depol} to 100 ms, every new experiment starts with a much reduced hyperpolarization of the ^{31}P nuclei, and the expected response to the BIR-4 pulse is recovered (black dots).

4.5 Summary and outlook

We have demonstrated here the capabilities of pulsed broadband EDMR using shaped pulses for a frequency range from 4 MHz to 18 GHz. The high conversion factor of $\approx 1.1\,\mathrm{mT}\,\sqrt{\mathrm{W}}^{-1}$ allows to generate 50-ns-long π-pulses for ESR with a microwave power of ≈100 mW, which is well below the amplifier 1 dB compression point of the broadband amplifier. We furthermore demonstrated the delivery of shaped pulses to the broadband antennas as well as the realization of full adiabatic inversion pulses and BIR-4 universal rotation pulses for both ESR and NMR, ultimately achieving electrically detected ENDOR with adiabatic pulses only. We will now use these capabilities to compare the performance of adiabatic and optimal control pulses (chapter 5) and to implement micro-coil-based magnetic resonance imaging where the design of the microwave excitation with stripline antennas results in a B_1-inhomogeneity of up to ±50 % (chapter 6).

5

Optimal control pulses for magnetic resonance

Optimal control pulses designed by e.g. gradient ascent pulse engineering have shown to be a versatile tool in nuclear magnetic resonance (NMR) to design pulses with increased excitation bandwidth [25], compensate for spectrometer imperfections like radio frequency amplitude inhomogeneities [33] or heteronuclear decoupling [30], to name but a few. The higher gyromagnetic ratios and shorter coherence times usually found in electron spin resonance require the pulses in ESR to be shorter (tens of nanoseconds rather than microseconds) and at higher frequencies (gigahertz instead of megahertz) compared to NMR pulses. Therefore, shaped adiabatic or optimal control pulses have not been used in ESR until recently, when arbitrary waveform generators with a high enough bandwidth became available. Since then, for ESR, adiabatic [91, 102, 109–113] and optimal control pulses [35] have mainly been used for their increased excitation bandwidth compared to rectangular pulses. In the field of optically detected magnetic resonance (ODMR), optimal control pulses were used to increase the fidelity of spin entanglement [39], for sensitive magnetic field measurements [36, 40] and for qubit control beyond the rotating wave approximation [38]. In this chapter we explore the use of optimal control pulses for pulsed electrically detected magnetic resonance to compensate for effects introduced by the frequency space[1] resonance linewidth ($\Delta\nu_0$) and by microwave field ($\Delta\nu_1$) inhomogeneities. Using the characterization of the spectrometer obtained in section 3.3.3 and the specific properties of our spin pair (section 5.1) we can simulate the effect of arbitrary pulses on our system (section 5.2). We compare these simulations with measurements for universal rotation pulses (optimal control, BIR-4 and rectangular, section 5.3) and echo decays built from universal rotation optimal control pulses, cooperatively optimized [37] optimal control, adiabatic and rectangular pulses (section 5.4).

5.1 Sample characterization

To avoid the problems caused by a resonator [35, 88] and for the free choice of the operating frequency, we again use a stripline antenna similar to structure e, but with a separate finger structure beneath the gap between short and block, for the microwave excitation [14, 18, 96] (c.f. section 3.2.2). Figure 5.1 b) shows a frequency-swept pEDMR spectrum shifted by the resonance frequency of the low-frequency ^{31}P resonance ($\nu_{\mathrm{low}} = 14.25\,\mathrm{GHz}$) and a simultaneous fit of five Lorentzians (green curve). The spectrum was measured using Gaussian π-pulses with a sigma of 144 ns for an external magnetic field of $B_0 = 511.6\,\mathrm{mT}$. At this magnetic field, the hyperfine-split low-frequency ^{31}P resonance (red curve) is separated from its dangling bond readout partners (blue curves) and the high-frequency ^{31}P resonance (red curve) by about 100 MHz. The resonance (magenta) centered between both ^{31}P resonances might either stem from conduction band electrons [114] or exchange-coupled phosphorus electron spins [115].

For optimal control pulse optimization we need to determine both the linewidth of the ^{31}P resonance as well as the ν_1-inhomogeneity caused by our antenna structure. From the fit we find the instrumentally broadened FWHM linewidth of the low frequency ^{31}P resonance

---

[1] We employ a frequency-space linewidth instead of the magnetic field linewidths used in the last chapter because this simplifies the comparison of experimental results and pulse simulations.

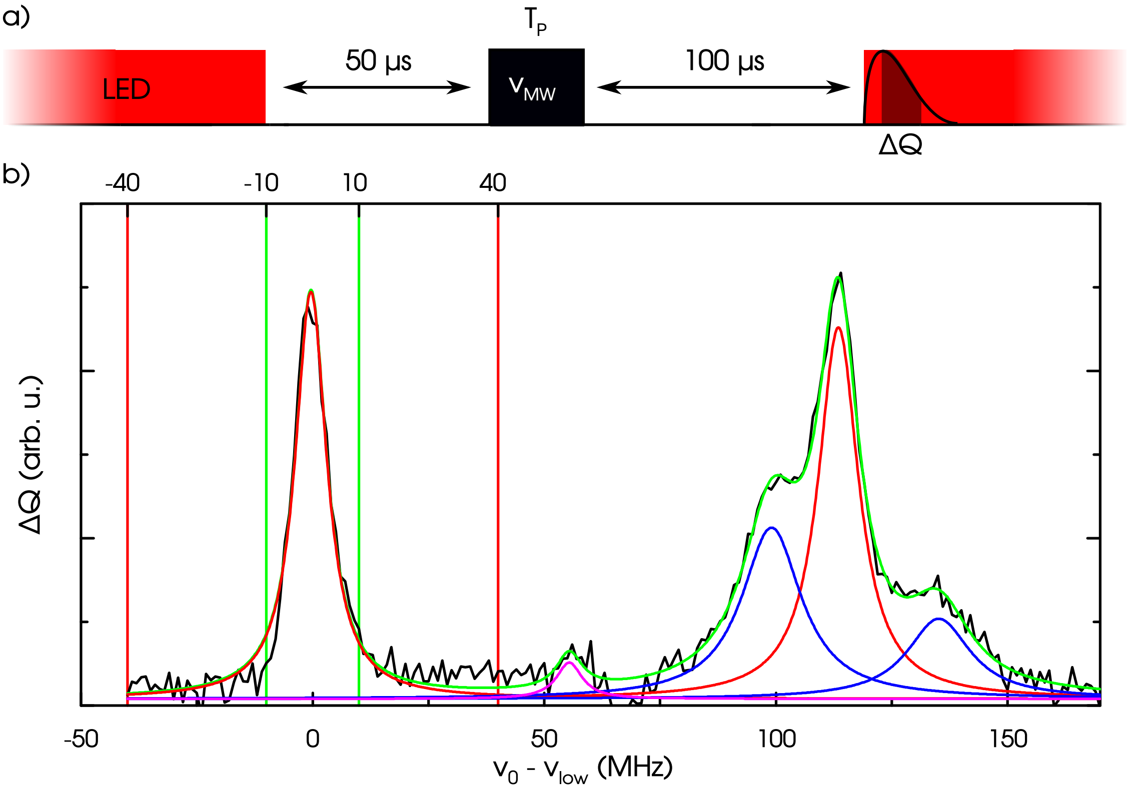

Figure 5.1: a) Pulse sequence used for the measurements. b) Frequency-swept spectrum of Si:P for a magnetic field of 511.6 mT shifted by the resonance frequency of the low-frequency ^{31}P resonance ν_{low}. A combined fit of five Lorentzian lines is plotted in green. Its parts are color-coded as follows: red corresponds to the hyperfine-split ^{31}P resonance, blue is used for the different $\mathrm{P_{b0}}$ orientations and magenta represents the conduction band electron or exchange-coupled phosphorus resonance. The optimization region and the cut-off region for optimal control pulses are depicted by vertical lines in green and red, respectively.

to be 8.3 MHz. Knowing this, we set the $\Delta\nu_0$ optimization window to ±10 MHz (vertical green lines in figure 5.1 b)), which allows us to coherently manipulate at least 75 % of the resonance. It is possible to increase this window at the cost of either pulse fidelity or pulse playtime. Unfortunately, for pEDMR it is insufficient to only optimize the pulse over this bandwidth. In addition, the pulse has to leave the readout partner untouched. To achieve this, we cut off

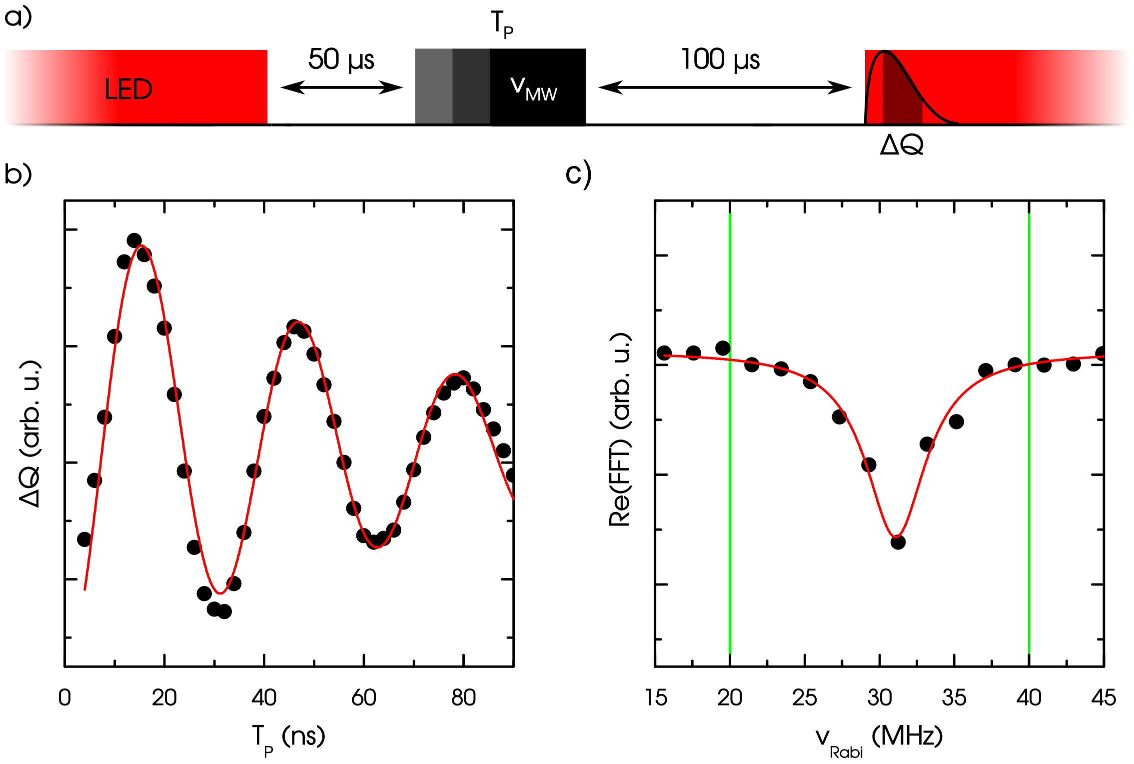

Figure 5.2: a) Pulse sequence used for the measurements. b) Excerpt of Rabi oscillations measured on the low-frequency ^{31}P resonance with a fit of an exponentially decaying cosine (red line). c) Real part of the Fourier transform of the fully-decayed Rabi oscillations measured on the low-frequency ^{31}P resonance. The optimization region for optimal control pulses is depicted by the green vertical lines.

all pulse components with a frequency higher than ±40 MHz (red vertical lines in figure 5.1 b) during the optimization. This results in smooth pulses similar to the ones optimized in reference 40.

In order to determine our optimization window for the ν_1-inhomogeneities, we measured Rabi oscillations using rectangular pulses. Figure 5.2 b) shows an excerpt of the Rabi oscillations in ΔQ as a function of the rectangular pulse length T_P. The red line is a fit of equation 4.1 with a Rabi frequency of $\nu_\mathrm{Rabi} = 32\,\mathrm{MHz}$ and a dephasing constant of $\tau_\mathrm{deph} = 72\,\mathrm{ns}$. Following the argument in reference 96, the full width at half maximum (FWHM) of the resonance can be estimated from τ_deph to be $\Delta\nu_1 = 4.4\,\mathrm{MHz}$. For a more thorough analysis, we transform these oscillations, which were measured up to pulse lengths where they vanish in the background noise, perform a complex rotation by 60° to account for the missing zero value and take the real part (c.f. figure 5.2 c)). With a fit of a Lorentzian (red line in figure 5.2 c)) we find $\Delta\nu_1 = 4.9\,\text{MHz}$. Here we chose a rather large window of ±10 MHz (vertical green lines in figure 5.2 c) to be able to use the pulses for other structures with a higher ν_1-inhomogeneity, too (c.f. section 4.2). For this particular sample, a reduction of the ν_1-window could be used to calculate shorter pulses or generate pulses with a higher fidelity.

5.2 Simulation and measurement of Δv_0-v_1-maps

Having characterized our system, we now perform a comparison between simulations and measurements for the example of an optimal control universal rotation $\pi/2$-pulse with a length of 300 ns. It was optimized using the constraints shown in figure 5.1 c) and figure 5.2 c) using the GRAPE algorithm (c.f. section 2.5.2). Since pEDMR is sensitive to polarizations as opposed to coherences we concatenate two $\pi/2$-pulses to obtain an effective π-rotation or no net rotation which we use in alternating sequences (cycles) to generate a lock-in effect [59]. The corresponding sequence is shown in figure 5.3 a), where the height of the depicted shapes encodes the amplitude and the brightness encodes the phase throughout the pulse. Its borders are depicted by vertical red lines.

We use this sequence to map the response of the pulse to offsets in both ν_0 and ν_1 using a simulation of the spin movement during the pulse and pEDMR measurements. Figure 5.3 b) shows the simulated z-projection after the pulse as a function of the ν_0-offset $\Delta\nu_0$ and ν_1. Here, a value of -0.5 corresponds to no rotation of the spin during both cycles and a value of 0.5 reflects the situation in which the cycle with the effective π-pulse results in a rotation by π and the cycle with the 0-pulse leaves the spins in their initial state. The green horizontal and vertical lines depict the optimization goals of the pulse, which are fully met by the optimized pulse.

For a more realistic simulation, we include the system impulse response determined in section 3.3.3 in figure 5.3 c). Figure 5.3

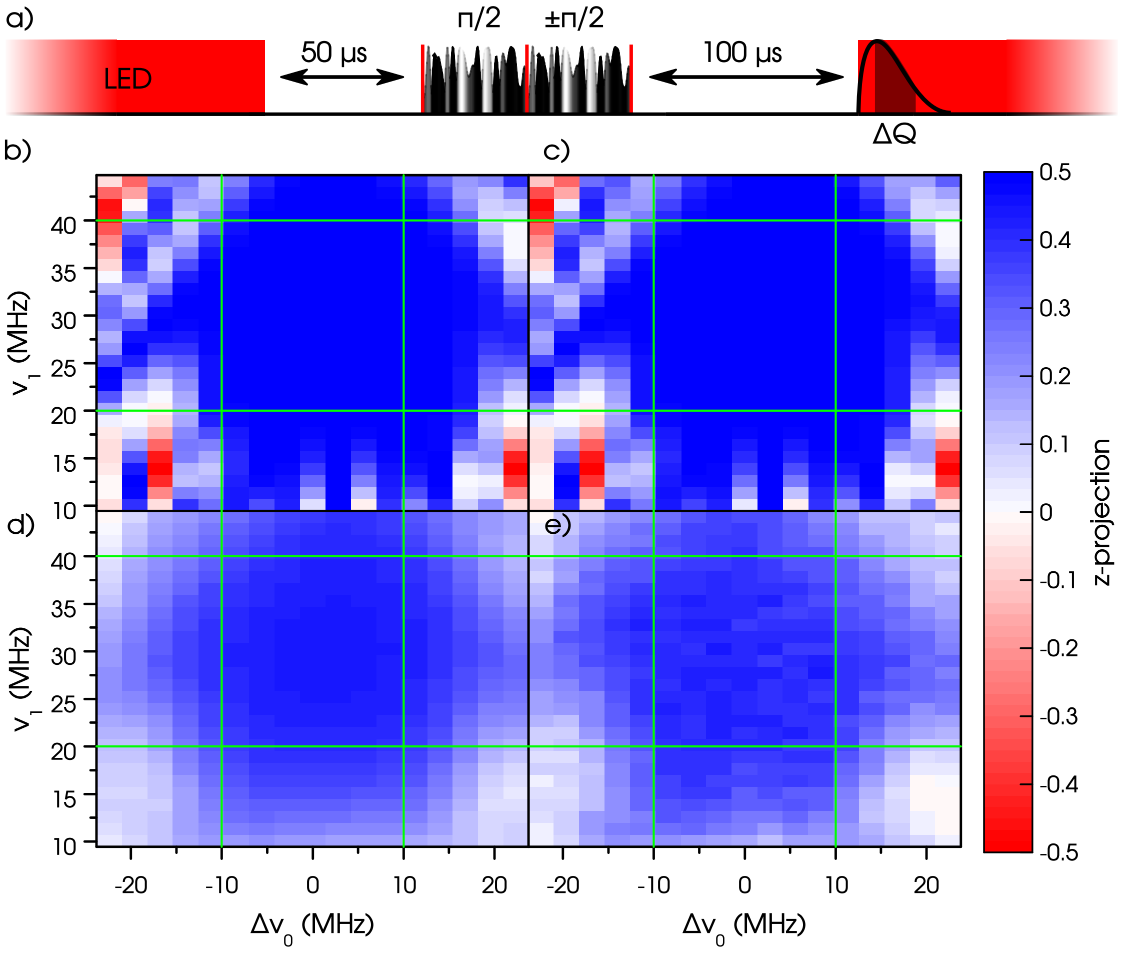

Figure 5.3: a) Pulse sequence used for all measurements and simulations in this figure. The amplitude and phase of the optimal control pulse are depicted by its height and brightness, respectively. Pulse borders are marked with green vertical lines. b) Simulated subtracted map of the spin z-projection for two cycles using an effective π- and 0-pulse. c) z-projection from panel b) simulated including the impulse response shown in figure 3.7. d) z-projection from panel c) convoluted with the ν_1-widths found in figure 5.2 and a ν_0-width determined by Fourier transforming the FID. e) Map of z-projection measured on the low-frequency ^{31}P resonance.

b) and c) are virtually identical. This is expected, because the system impulse response has a bandwidth of around 2 GHz, which is much larger than the 80 MHz bandwidth of our pulse. Therefore,

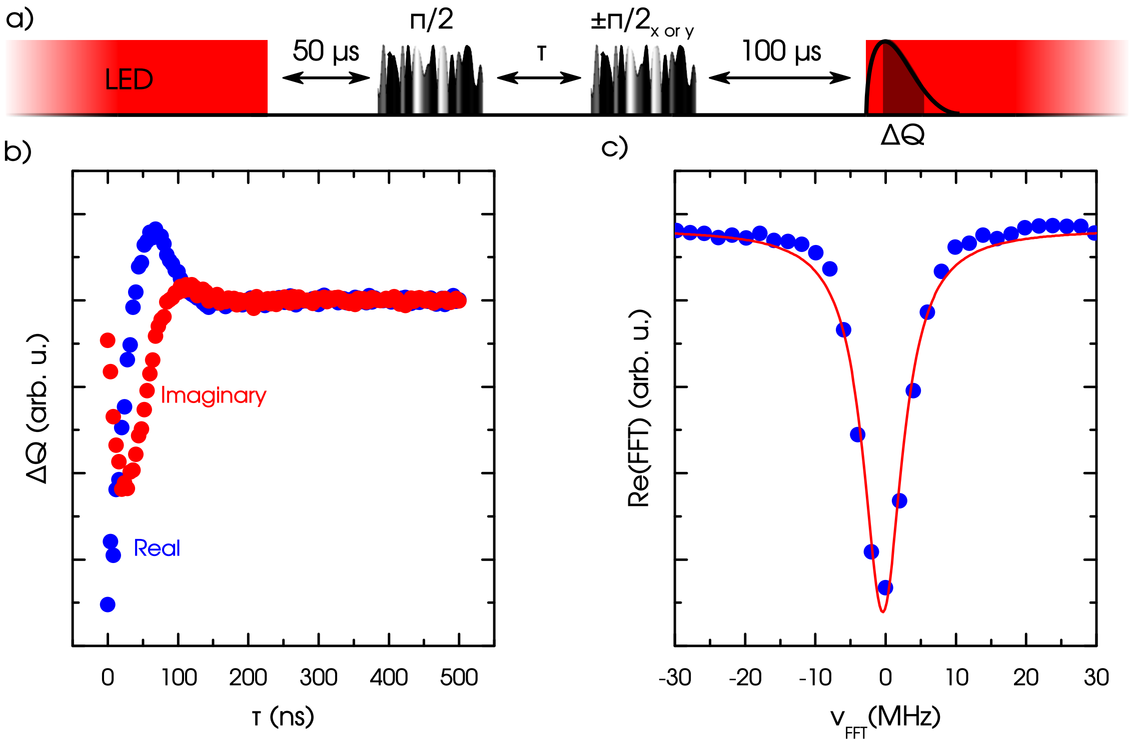

Figure 5.4: a) Pulse sequence used for the FID detection. b) Real and imaginary part of the FID. c) Real part of the Fourier-transformed FID. The fit of a Lorentzian function is shown in red.

in contrast to reference 35, we can ignore the system impulse response for all further pulse optimizations.

To be able to compare measurement and simulation, we have to include the ν_0- and ν_1-distributions of our system. Since the ν_0-distribution extracted from the spectrum is instrumentally broadened, we measured a FID (c.f. section 2.3.2) by using pulses with an optimization window of 20 MHz and Fourier transformed the result. Figure 5.4 b) plots the real and imaginary part of the FID measured with x and y projection pulses, respectively, as a function of the inter-pulse distance τ. The non-vanishing imaginary part is probably due to a slight detuning between the actual resonance frequency and the microwave pulse frequency and the resulting Fourier transform (figure 5.4 c)) shows a slight deviation from zero for this reason. The fit of a Lorentzian[2] to this peak yields a ν_0-distribution FWHM of

---

[2] As can be seen from figure 5.4, the shape of the resonance is not completely described by a

$\Delta\nu_0 = 6.8\,\mathrm{MHz}$ (indeed smaller than the $\Delta\nu_0 = 8.3\,\mathrm{MHz}$ determined from figure 5.1), which should allow the optimal control pulse to work on 79 % of the ν_0-distribution. It is also possible to obtain this information by Fourier transforming a spin echo, which results in the same distribution (data not shown).

By using a two-dimensional convolution of the simulation shown in figure 5.3 c) with the normalized ν_0- and ν_1-distributions we arrive at the map shown in figure 5.3 d). The z-projection does not reach -0.5 but has a minimum of -0.44, which corresponds to 88 % of the total value. This percentage is higher than the expected 79 %, because the pulse fidelity does not drop to zero instantaneously outside of the optimization window.

For comparison we measured the pEDMR signal ΔQ as a function of the AWG channel voltage, which is proportional to the square root of the channel output power and accordingly proportional to ν_1, and as a function of the external magnetic field. To obtain the ν_1-axis, we take the Rabi measurements shown in figure 5.2 b) and transform the channel voltages to nutation frequencies. The values of the ν_0-axis were calculated with the help of the phosphorus g-factor g_p. Since pEDMR does not yield absolute values, we scaled the measurement to the simulation in figure 5.3 d) by using a far off-resonance field as the zero value and adjusting the maximal pEDMR value so that it is equal to the simulated maximum. Figure 5.3 e) shows the resulting map measured on the low frequency ^{31}P resonance, which, apart from noise, shows a high agreement between simulation and measurement. This comparison was made for all pulses used in this work and shows a similarly high consistency between measurement and simulation in each case.

5.3 Adiabatic and optimal control universal rotation pulses

We use this understanding of our system to study the performance of optimal control universal rotation π/2- and π-pulses in comparison

---

Lorentzian. This is due to the interaction of the ^{31}P electron spin with surrounding ^{29}Si nuclear spins [116].

to their adiabatic and rectangular counterparts. Again, for the optimal control pulses we apply the optimization goals determined from figure 5.1 b) and figure 5.2 c) and employ pulses with a length of $T_\mathrm{p} = 300\,\mathrm{ns}$. For the adiabatic pulse we choose the BIR-4 [22] universal rotation pulse because it allows us to easily switch its rotation angle from $\pi/2$ to π without the need to re-optimize the pulse (c.f. section 2.5.1.2). A pulse length of $T_\mathrm{p} = 200\,\mathrm{ns}$ results in a total play time of the BIR-4 sequence of 800 ns. The parameters $\nu_{1,\mathrm{max}} = 30\,\mathrm{MHz}$, $\Delta\omega_\mathrm{max} = 2\pi \cdot 72.9\,\mathrm{MHz}$, $\zeta = 10$ and $\kappa = 0.7$ were found by optimizing each value using pEDMR measurements and pulse simulations. The resulting minimum adiabaticity [78] is $\eta = 21$. These rather high values are needed to ensure the off-resonance fidelity of the adiabatic pulse which is limited by the maximal possible nutation frequency ν_1 in comparison with the resonance linewidth $\Delta\nu_0$ (c.f. section 2.5.1.2). For the rectangular pulses the pulse times of 8 ns and 16 ns result in a $\pi/2$- and a π-pulse, respectively.

We first study the performance of universal rotation $\pi/2$-pulses. To gain an understanding of the performance of each of those pulses with respect to our ν_0- and ν_1-distributions, we plot the simulated 95 % fidelity line for two concatenated universal rotation $\pi/2$-pulses, using phase-cycling on the second $\pi/2$-pulse. These fidelities include the impulse response but not the convolution with the ν_0- and ν_1-distributions. Instead, we indicated the goals used in the optimal control pulse optimization with vertical and horizontal green lines. Here, the rectangular pulse (black line) does not reach these goals. It has both a worse ν_0-bandwidth and a worse response to ν_1-inhomogeneities compared to the BIR-4 pulse (red line) and the optimal control pulse (blue line). The BIR-4 pulse is equal or better than the optimal control pulse with respect to ν_1-inhomogeneities, but it does not reach the ν_0-bandwidth of the optimal control pulse, which is even greater than the ν_0-bandwidth of the optimization window. Therefore, we expect the optimal control pulse to perform better than the rectangular and BIR-4 pulse in the measurements because it shows a robustness to ν_1-inhomogeneities that is high enough for the studied ensemble and can even address off-resonant spins which lie outside the ν_0-optimization window, which only contains 79 % of the spin ensemble.

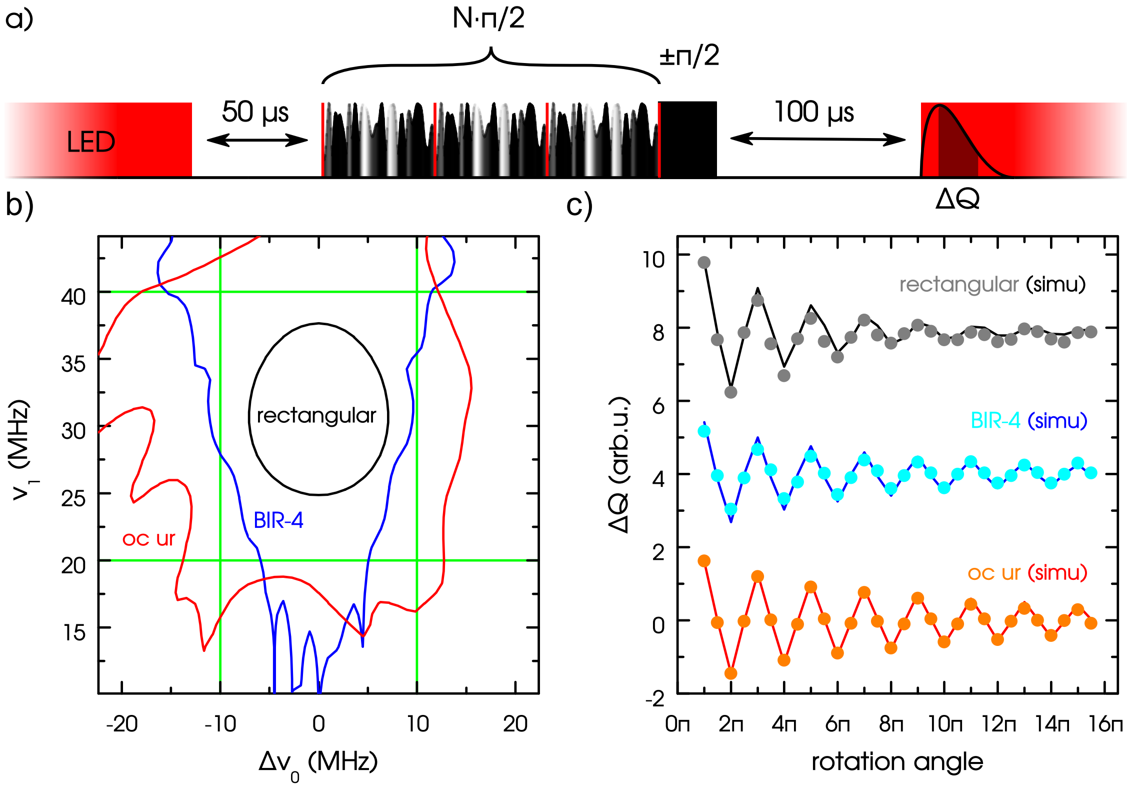

Figure 5.5: a) Pulse sequence used in panel c). b) Simulated 95 % fidelity circumference for two concatenated rectangular, adiabatic or optimal control universal rotation π/2-pulses using phase-cycling on the second $\pi/2$-pulse. The optimization goals are indicated by the horizontal and vertical green lines. c) EDMR signal amplitude after N concatenated rectangular, adiabatic or optimal control universal rotation π/2-pulses followed by a rectangular π/2 projection pulse. Darker colors depict the simulated effect of the respective concatenated pulse.

We now compare the performance of each pulse at its optimal point of the $\Delta\nu_0$-ν_1-map for N concatenated pulses with $N \leq 30$ in figure 5.5 c). The pulse sequence we employ for this is sketched in figure 5.5 a). A phase-cycled rectangular π/2-pulse, right after the concatenated pulses, is used for readout to filter out an ensemble with a low nutation frequency that is also present in our sample and would otherwise interfere with the measurements. According to the simulations, this results in a slightly reduced amplitude of 95 % and 90 % in the case of the BIR-4 and optimal control measurements, respectively. To combine the measured (dots) and simulated (lines) data, we multiply the simulated difference for $N = 1$ and $N = 3$ for the case of the optimal control pulses with a constant so that it equals the measured difference and adjust all other simulations with the same constant. Since the simulation does not include T_1- and T_2-effects, the simulated data is multiplied with a stretched exponential $A \cdot \exp\left(-\left(t/\tau\right)^n\right)$, whose parameters ($\tau = 9\,\mu\text{s}$ and $n = 0.7$) were found by fitting this exponential to the echo decay measurements shown in figure 5.7 c). This leads to a very high agreement between the simulations and the measurement for each case.

If we compare the amplitudes for all three pulse types, the rectangular pulse (black and gray) performs best, because it has the shortest duration while the adiabatic (blue and turquoise), and to a lesser extent the optimal control pulse (red and orange), suffer from decoherence because of their respective lengths. For higher rotation angles, the situation reverses, as the measurement using rectangular pulses deteriorates due to the ensemble ν_0- and ν_1-inhomogeneities, which leads to a faster decay than that caused by the decoherence. As an example, due to its shorter length and greater bandwidth, the measured amplitude is 29 % higher in the optimal control case than the BIR-4 amplitude for the rotation from 14π to 15π. We tried to shorten the BIR-4 pulse to counteract this behavior, but did not find a shorter BIR-4 realization that outperformed the BIR-4 measurements shown here.

In the case of universal rotation π-pulses, the 95 % $\Delta\nu_0$-ν_1-fidelity-maps (figure 5.6 b) for a single amplitude-cycled rectangular, adiabatic or optimal control pulse show a similar behavior as the maps for the two phase-cycled concatenated π/2-pulses. The main difference can be found for the rectangular pulse which has a wider ν_0-bandwidth than two concatenated π/2-pulses. This is not expected since both the single π-pulse and the two concatenated π/2-pulses have the same length of 16 ns. This difference is caused by the sequence where the second π/2-pulse has a phase of 180°, which results in no net rotation. The ν_0-bandwidth over which this sequence achieves its desired rotation angle is smaller than the ν_0-bandwidth of the sequence with a resulting π-rotation and thus results in a reduced ν_0-bandwidth of the phase-cycled sequence.

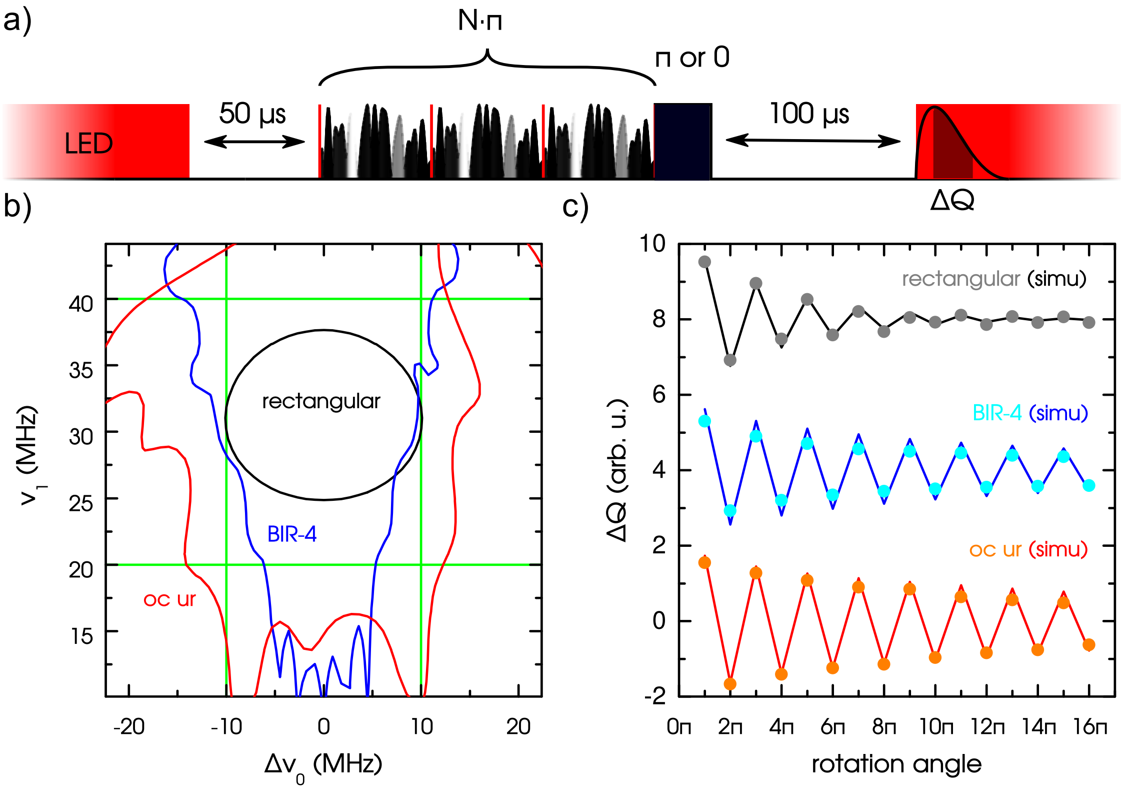

Figure 5.6: a) Pulse sequence used in panel c). b) Simulated 95 % fidelity circumference for one rectangular, adiabatic or optimal control universal rotation π-pulse using amplitude cycling. The pulse optimization goals are indicated by the horizontal and vertical green lines. c) EDMR signal amplitude after N concatenated rectangular, adiabatic or optimal control universal rotation π-pulses followed by a rectangular π-pulse. Darker colors depict the simulated effect of the respective concatenated pulse.

The performance of the pulses in the $\Delta\nu_0$-ν_1-fidelity-maps is reflected in the measurements for concatenated π-pulses (figure 5.6 c), for which we use the adjusted pulse sequence as shown in figure 5.6 a). Again, we use a rectangular pulse for readout to suppress the ensemble with a low nutation frequency. As was the case for the π/2-pulses, we have a very good agreement between the simulations and the measurements. In contrast to the π/2 results, the gains of the adiabatic and optimal control pulses compared to the rectangular pulse are much higher for a given rotation angle, since we only need one pulse for a π-rotation so that even for the difference between a π- and 2π-rotation, the optimal control pulse outperforms the rectangular pulse. The difference between the BIR-4 and optimal control pulse for the rotation from 14π to 15π is 18 %.

5.4 Adiabatic and optimal control Hahn echo sequence

Using these optimal control π- and π/2-pulses, we build an Hahn echo sequence (c.f. section 2.3.3) to compare the characteristics of optimal control to adiabatic and rectangular pulses in a sequence. The corresponding sequence is shown in figure 5.7 a). Since significant ν_1-inhomogeneities are present in the sample, ν_1-insensitive pulses are necessary. Therefore, we use an adiabatic half passage for the excitation, a BIREF-1 [20] pulse for refocusing and a time-reversed adiabatic half passage for the projection of the echo onto the z-axis for the adiabatic sequence. The BIREF-1 pulse is used to shorten the total sequence length, because we do not need the adjustable rotation angle of the BIR-4 pulse. All adiabatic half passages have a length of 400 ns resulting in a total length of 1.6 µs and a minimal $\eta = 76$ for the parameters $\nu_{1,\max} = 30\,\mathrm{MHz}$, $\Delta\omega_{\max} = 2\pi \cdot 34\,\mathrm{MHz}$, $\kappa = 0.2$ and $\zeta = 3$. As was the case for the adiabatic universal rotation pulses, we tried to shorten their length but could not improve the results of the adiabatic echo. For the rectangular echo, we again use π/2- and π-pulses with a length of 8 ns and 16 ns, respectively. The echo using optimal control pulses is built from the universal rotation π/2- and a π-pulses introduced in the last sections. Since the universal rotation pulses suffered from decoherence in the previous experiments, a shorter optimal control echo built by replacing the two universal rotation excitation and projection pulses with point-to-point pulses, could lead to larger amplitudes. We take this approach one step further and use a cooperatively optimized [37] optimal control echo sequence which halves the lengths of the individual pulses ($T_\mathrm{P} = 150\,\mathrm{ns}$) compared to the universal rotation optimal control pulses.

The simulated results of all four pulse sequences are plotted in the 95 % $\Delta\nu_0$-ν_1-map shown in figure 5.7 b) which exhibits a

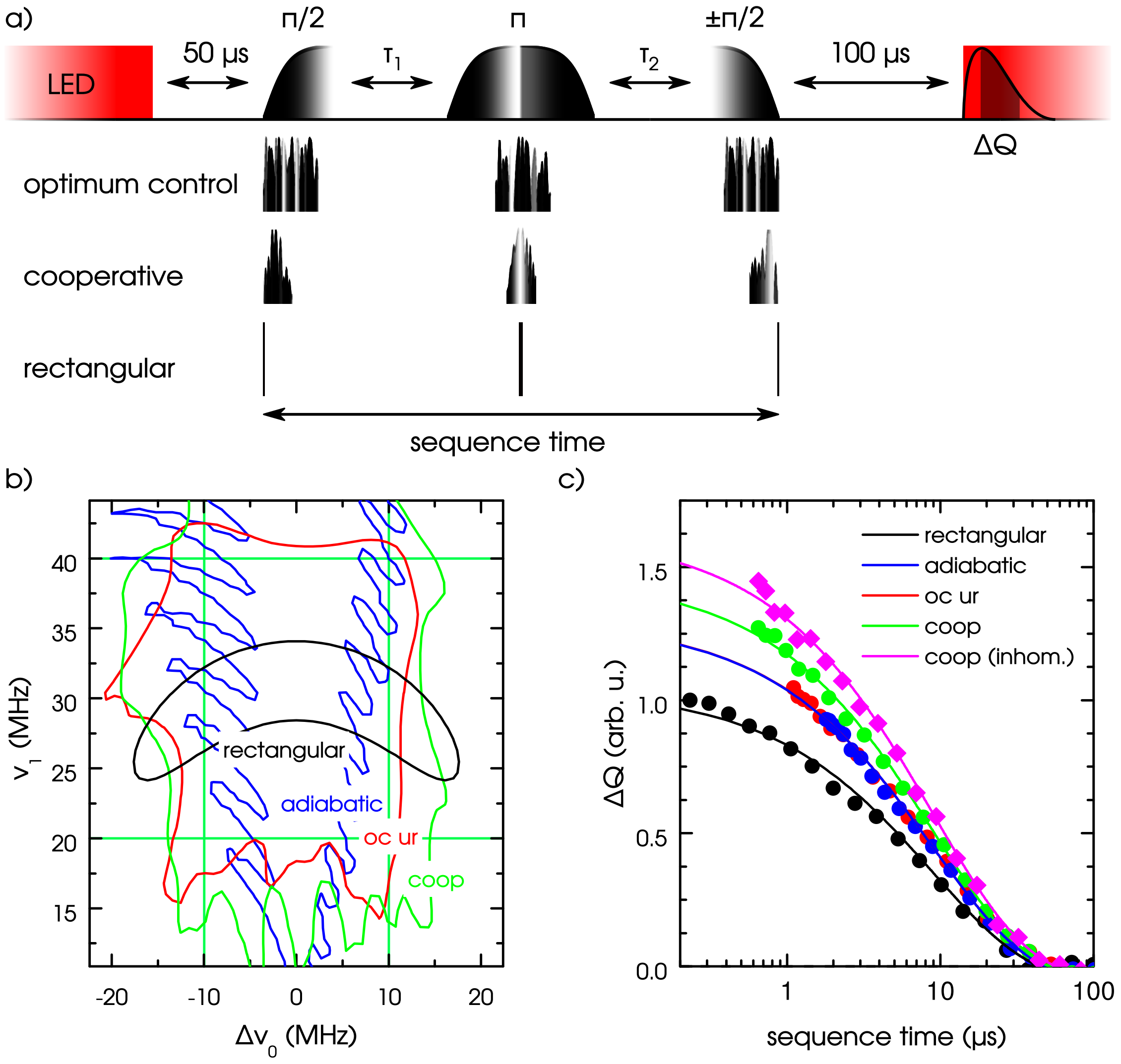

Figure 5.7: a) Pulse sequence used in panels b) and c). b) Simulated 95 % fidelity circumference for a phase-cycled echo sequence built from rectangular, adiabatic, universal rotation optimal control or cooperatively optimized optimal control pulses. The goals used for the optimal control optimization are plotted in green. c) Echo decay measurements for the echo sequences simulated in b). A fit of a stretched exponential for each decay is shown as a line.

similar behavior to the maps in figure 5.5 b) and figure 5.6 b). Remarkably, even though the cooperatively optimized sequence is much shorter than the echo sequence built from universal rotation pulses, its robustness to ν_1-inhomogeneities is considerably higher.

Therefore, shorter cooperatively optimized sequences should be possible, but even a sequence with 75-ns-long pulses might only improve upon the total amplitude by 5 % for the T_2 times present in our system.

To be able to compare the different echo sequences despite their different pulse lengths, we measured an echo decay for each sequence. Figure 5.7 c) plots the pEDMR signal ΔQ as a function of the total length of each sequence. The decays for all sequences are fitted simultaneously with one stretched exponential where only the amplitude is adjusted individually. The resulting parameters are $n = 0.7$, $T_2 = 9\,\mu\text{s}$, $A_{\text{rectangular}} = 1.10$, $A_{\text{adiabatic}} = 1.35$, $A_{\text{oc ur}} = 1.35$ and $A_{\text{coop}} = 1.52$ for the rectangular, adiabatic, optimal control and cooperatively optimized optimal control sequence, respectively. If we compare these amplitudes, we find that both the adiabatic and universal rotation optimal control echo improve upon the rectangular sequence by about 23 % and the cooperatively optimized pulse enhances the echo signal by 38 % for equal sequence lengths. For a different sample with a higher ν_1-inhomogeneity (pink dots) the improvement of the cooperatively optimized echo sequence compared to the rectangular sequence is greater than 50 %. These improvements are higher than the values found by the simulation (not shown), which predicts gains of 25 %, 8 % and 4 % for the sample characterized in section 5.1 using the cooperatively optimized, optimal control and adiabatic echoes, respectively.

The cause for this behavior can be found in the properties of each sequence at the ν_0-frequencies of the readout partners. Figure 5.8 a) and b) plot the $\Delta\nu_0$-ν_1-map for one cycle of the rectangular and the cooperatively optimized sequence, respectively. The frequency, at which either the dangling bond resonances or the high-frequency phosphorus resonance will also be excited by the pulse, is marked by the black vertical line. Here, the rectangular pulse produces significant rotations at the dangling bond resonances while the cooperatively optimized sequence, as well as the echoes built from universal rotation pulses and adiabatic pulses, do not excite rotations at those frequencies. Since the simulations do not take the readout partner into account, we observe larger amplitudes for the adiabatic and optimal control sequences than predicted by the simulation.

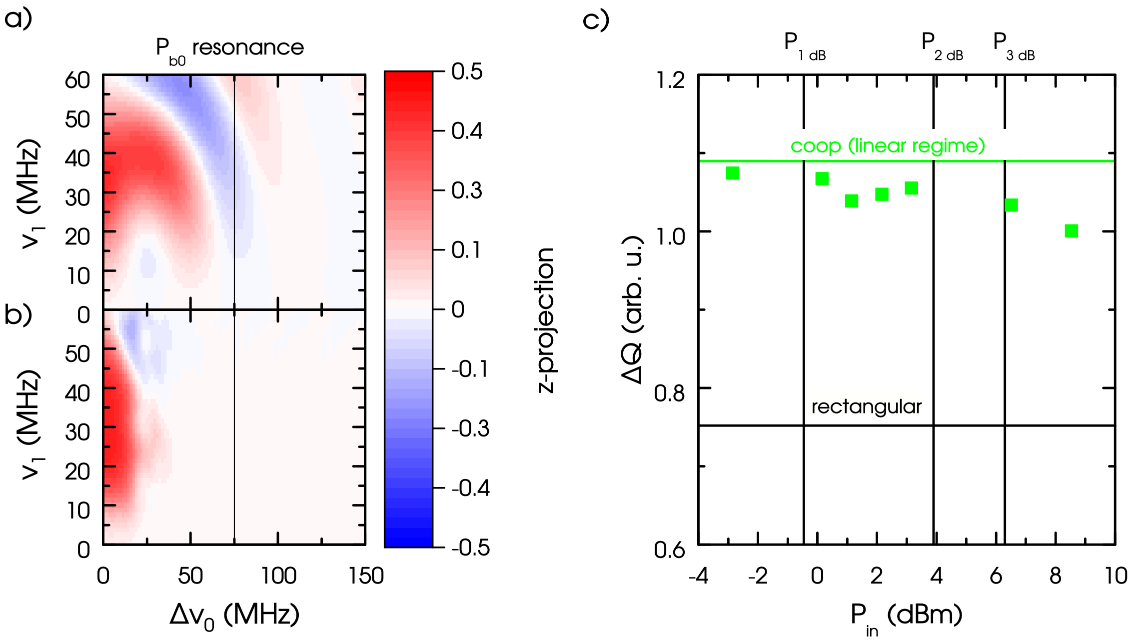

Figure 5.8: a) Simulated $\Delta\upsilon_0$-υ_1-map of the z-projection for a rectangular echo and the cooperatively optimized optimal control echo b). The onset of the dangling bond resonances is marked by the vertical black line. c) Echo amplitude ΔQ for a cooperatively optimized echo with a sequence length of 1.5 µs as a function of the AWG channel power P_{in}. The vertical black lines mark the 1 dB, 2 dB and 3 dB amplifier compression points $P_{1\,\mathrm{dB}}$, $P_{2\,\mathrm{dB}}$ and $P_{3\,\mathrm{dB}}$, respectively. The horizontal green and black lines show the results for the rectangular and the cooperatively optimized echo in the linear region for a sequence length of 1.5 µs.

To complete the picture, we now study the behavior of the cooperatively optimized optimal control echo in the presence of nonlinearities by gradually increasing the nonlinearity up to a compression of 4.5 dB. At each measurement point, the power for the cooperatively optimized echo was adjusted with a variable attenuator inserted after the power amplifier so that the echo amplitude was maximal. The resulting amplitudes ΔQ are plotted in figure 5.7 c) as a function of the AWG channel power P_{in}. The vertical black lines mark the 1 dB, 2 dB and 3 dB amplifier compression points $P_{1\,\mathrm{dB}}$, $P_{2\,\mathrm{dB}}$ and $P_{3\,\mathrm{dB}}$, respectively. The horizontal green and black lines show the results for the rectangular and the cooperatively optimized echo in the linear region for a sequence length of 1.5 µs. Up to a compression of 2 dB, the difference between the nonlinearly distorted optimal control echo and the echo in the linear regime is minimal, which renders predistortion schemes like those presented in references 103 and 105 unnecessary for all but the most demanding applications.

5.5 Summary and outlook

In summary, we have demonstrated the use of optimal control pulses for pEDMR with stripline antennas. The pulses, tailored to the specific needs of the system, show a distinct improvement over rectangular pulses and even outperform adiabatic pulses. By using cooperatively optimized pulses we were able to reduce the total sequence length of a Hahn echo sequence so that it clearly outperforms the shortest possible rectangular echo. This length makes it usable for systems with very short T_2 times e.g. for the ^{31}P-Pb_0 system without pulsed illumination [47] or in the readout echo of the ENDOR sequence as demonstrated in reference 117. Furthermore, the use of optimal control theory opens up e.g. pattern pulses [28] which could be useful for systems with a small distance between the resonances of the readout partners as e.g. in reference 9. These pulses allow for sharp transitions in ν_0 and can correct for ν_1-inhomogeneities whereas more traditional sinc pulses can create equally sharp ν_0-profiles but do not correct for ν_1-inhomogeneities.

6

EDMR imaging using magnetic field gradients

Although EDMR is widely used to characterize point defects and charge transport in inorganic and organic semiconductors [2, 4, 6–8], the spatial origin of the EDMR signal is not well understood. With the help of DEER distance measurements Suckert et al. [45] were able to pinpoint the main contribution to the EDMR signal of ^{31}P-Pb_0 spin pairs to a region between 14 nm and 20 nm below the surface of the semiconductor. However, these experiments did not provide any lateral resolution. For measurements on samples, where the current is recorded only through two contacts, as is the case for the structures c, d and e in figure 3.5, the spatial origin of the signal becomes important for the placement of the measurement structure with respect to the microwave antenna. This can be seen by the Rabi measurements on structure e (c.f. section 3.2.2.2) for voltages of 4 V and −4 V which are plotted in figure 6.1 a) and b), respectively. Despite being measured on the same sample without any changes to the measurement setup or the sample itself, both the Rabi frequency and the dephasing of the Rabi oscillations are considerably different. A fit of equation 4.1 to the data (red lines) yields values of 28 ns

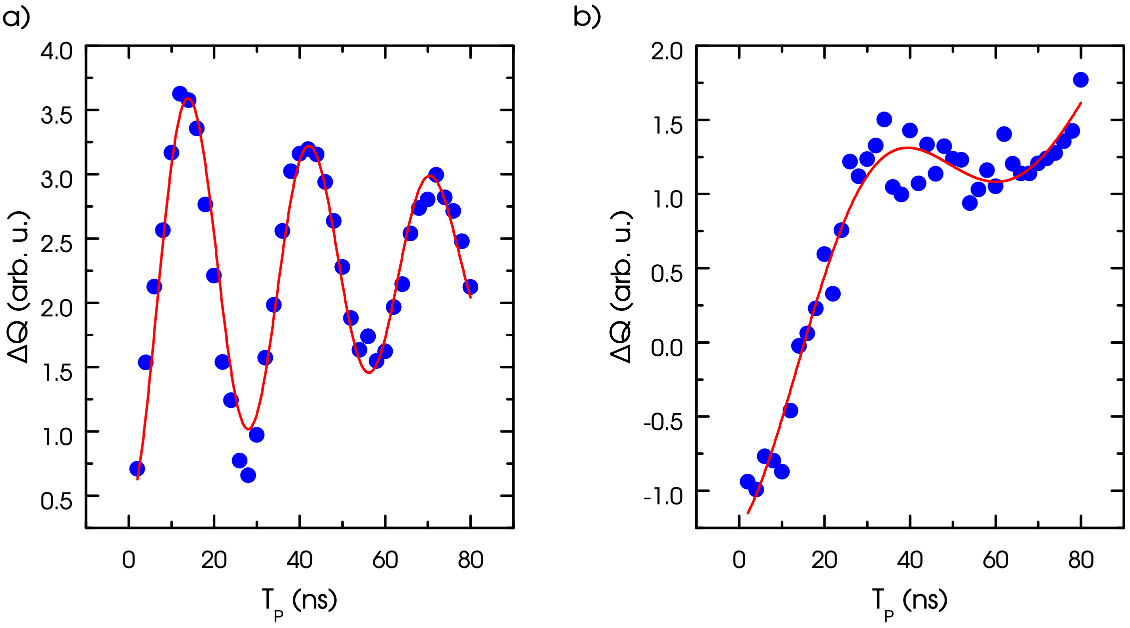

Figure 6.1: Rabi oscillations measured on structure e with a bias voltage of 4 V (panel a)) and −4 V (panel b)). The red curves are a fit of equation 4.1.

and 71 ns for the oscillation periods and dephasing times of 63 ns and 76 ns, respectively. Since these differences cannot stem from changes in the setup or the sample, the spin resonance experiment must address different ensembles which are subject to different B_1 fields depending on the bias voltage. In all likelihood, these differences are caused by spatially separated ensembles which see a different B_1 due to different distances between the ensemble and the microwave antenna.

At the moment there are three approaches for position-dependent EDMR. The method developed by Katz et al. [60] uses pulsed magnetic field gradients similar to magnetic resonance imaging to generate a Fourier transform of the spin density in the sample. The actual image is then recovered through the inverse Fourier transform (c.f. section 2.4). Klein et al. [118] contact the sample locally with conductive atomic force microscopy (cAFM) and record the spin-dependent current from the cAFM tip to a back contact. This method has the severe drawback that its current stability is limited by the quality of the contact between the sample and the cAFM tip [119], which makes it particularly unsuitable for the long term measurements required for high resolutions. Lastly, tunneling-based concepts for position-dependent EDMR are discussed [120, 121], but no measured spin-dependent signal is published up till now. Therefore, at the moment, imaging using gradients appears to be the most promising candidate for position-dependent EDMR measurements with a high spatial resolution.

In this chapter we discuss modifications to the microwave setup necessary for Fourier transform imaging (section 6.1) and the results of Fourier transform imaging experiments on the interdigit contact structure introduced in this section. We use these modifications for a first basic implementation of echo-based imaging using rectangular pulses (section 6.2). This experiment is improved by the use of a cooperatively optimized optimal control echo (section 6.3) and corrections for the B_0-nonlinearities caused by our implementation of the gradient field generation (section 6.4). Afterwards, the measurement results are interpreted using the band structure of a metal-semiconductor-metal (MSM) structure (section 6.5) and we work out the resolution of the current experiment and its theoretical limits under optimal conditions (section 6.6). Finally, we recommend changes to the typical interdigit contact structures used for pEDMR experiments based on the results obtained in this work (section 6.7).

6.1 Modifications to the measurement setup for gradient field generation

In addition to the spatially and temporally constant external magnetic field $\vec{B}_0 = B_0\vec{e}_z$ and the time-dependent but ideally spatially constant microwave magnetic field $\vec{B}_1(t) = B_1\vec{e}_y$, Fourier transform imaging introduces a temporally and spatially varying magnetic field $\vec{B}_{\text{gradient}}(\vec{x}, t) = B_{\text{gradient}}(\vec{x}, t)\,\vec{e}_z$ to encode the position of the spins in an ensemble. Ideally, this additional time- and position-dependent $\vec{B}_{\text{gradient}}(x, t)$ can be described by a spatially constant gradient $\vec{G}(t)$, so that the external magnetic field is transformed to $\vec{B}_0(x) = \left(B_0 + \left(\vec{G}(t) \cdot \vec{x}\right)\right)\vec{e}_z$.

Traditionally, magnetic gradient fields for imaging experiments are generated by coils in a Maxwell or Golay configuration [60, 122].

These coils have the advantage that their gradient field is approximately spatially constant, but they need pulse gradient drivers which are able to provide pulses with a voltage of hundreds of volts to induce a current which is high enough for imaging experiments with the desired resolution [122]. These coils dissipate significant amounts of heat so that the cooling power of the used cryostat limits the achievable resolution. Another approach, applied until now only to spatially resolved ODMR, uses microcoils [74], which are able to generate much higher gradient fields for a given current at the expense of gradient field uniformity.

6.1.1 Dissipation-limited resolution

To estimate the limits to the resolution caused by the dissipation of heat inside the gradient coils we assume that the power dissipated into the cryostat is solely given by the ohmic losses of the coils $P_{\mathrm{max}} = I^2R \cdot N$, which is determined by the resistivity R of the coils, the number of coils N and the current necessary to achieve the desired gradient fields. The current I is determined by the efficiency e of the coils, which is defined to be $e = G/I$ with G being the magnetic field gradient. Since the gradient pulse will only be active for a time T_{P} during a sequence of length t_{seq}, the maximal power during the gradient pulse can be much higher than the mean cooling power of the cryostat $P_{\mathrm{mean}} = P_{\mathrm{max}} \cdot T_{\mathrm{P}}/t_{\mathrm{seq}}$. For a given rectangular gradient and a desired resolution of Δx, we can extract the required gradient from equation 2.21

$$G = \frac{h}{2g\mu_e \Delta x T_{\mathrm{P}}}. \tag{6.1}$$

With those relations we can express the minimal resolvable feature-size in one-dimensional imaging

$$\Delta x = \frac{h}{2g\mu_e}\sqrt{\frac{RN}{P_{\mathrm{mean}}t_{\mathrm{seq}}T_{\mathrm{P}}}}\frac{1}{e}. \tag{6.2}$$

The coils used by Shtirberg et al. [122] have radii between 1.4 mm and 1.8 mm, a resistivity of $R = 0.55\,\Omega$ and efficiencies between $e = 2.7\,\mathrm{T\,m^{-1}\,A^{-1}}$ and $e = 4.66\,\mathrm{T\,m^{-1}\,A^{-1}}$. For a 1-µs-long gradient pulse, a sequence length of 1 ms and a three-dimensional ($N = 3$) acquisition of phosphorus donor electron spins in silicon, we find $\Delta x = 270\,\mathrm{nm}$ for this setup if all the cooling power of the cryostat can be used.

The g-factor g depends on the spin species and cannot be changed while the number of coils N depends on the dimensionality of the sample at hand and will be fixed for this reason, too. The resistivity R is usually given by the geometry and material of the coils and P_{mean} is determined by the cryostat. Changing the values t_{seq} and T_{P} has a small effect because of their square root dependence so that only the efficiency e remains as a viable variable to increase the resolution. As is the case with the stripline antennas for the microwave B_1-field excitation, reducing the volume of the gradient field will increase the efficiency. Through the use of gradient "microcoils", which are basically two coplanar conductors placed at a distance of 100 µm, Arai et al. [74] indeed achieve a resolution of 3 nm for pulsed gradient imaging on nitrogen vacancy centers at room temperature.

6.1.2 Efficiency of gradient microcoils

To estimate the efficiency of a microcoil arrangement, we use the magnetic field B_{gradient} generated by two infinitely long and infinitely thin parallel current carrying wires (which we will call antennas) in the plane of the antennas as a function of the position x between the antennas for a current I and an antenna-to-antenna distance d of

$$B_{\mathrm{gradient}}(x) = \frac{\mu_0 I}{2\pi}\left(\frac{1}{x} - \frac{1}{d-x}\right). \tag{6.3}$$

By differentiating equation 6.3 with respect to x, inserting $x = d/2$ and dividing by I we find the gradient efficiency e half way between both antennas to be

$$e(d/2) = \frac{4\mu_0}{\pi d^2}. \tag{6.4}$$

For the antenna-to-antenna distance of 100 µm used in reference 74 this results in an efficiency of $e = 160\,\mathrm{T\,m^{-1}\,A^{-1}}$ and therefore a resolution gain by a factor of 60 compared to the coils used by

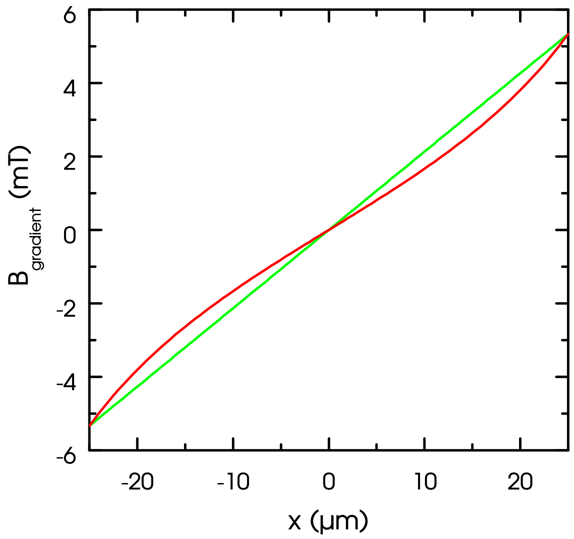

Figure 6.2: Magnetic field B_{gradient} as a function of the position x between two microcoils (positioned at $x = \pm 50\,\mu\text{m}$) for a current of 1 A, an antenna-to-antenna distance of 100 µm and a field of view of 50 µm (red line). A linear function between the extremal values of B_{gradient} is plotted in green.

Shtirberg et al. [122]. This results in a reduction of the feature-size to $\Delta x = 4.6\,\text{nm}$ if all other parameters remain roughly the same as before. Unfortunately, similar to the B_1-inhomogeneity of stripline microwave antennas, this improvement in Δx is achieved at the cost of a non-uniform gradient $G(x)$ which results in a nonlinear $B_{\text{gradient}}(x)$. Figure 6.2 plots B_{gradient} as a function of x for an antenna-to-antenna distance of 100 µm and a field of view of $f = 50\,\mu\text{m}$ (red line). As can be seen by comparing B_{gradient} with the linear function (green line)

$$l(x,f) = m(f) \cdot x \tag{6.5}$$

$$\text{with} \quad m(f) = \frac{B_{\text{gradient}}(f/2) - B_{\text{gradient}}(-f/2)}{f} \tag{6.6}$$

which is found by connecting the B_{gradient} values for $x = 25\,\mu\text{m}$ and $x = 75\,\mu\text{m}$, this B_{gradient} deviates strongly from the optimal linear behavior which is desired for phase-encoded MRI.

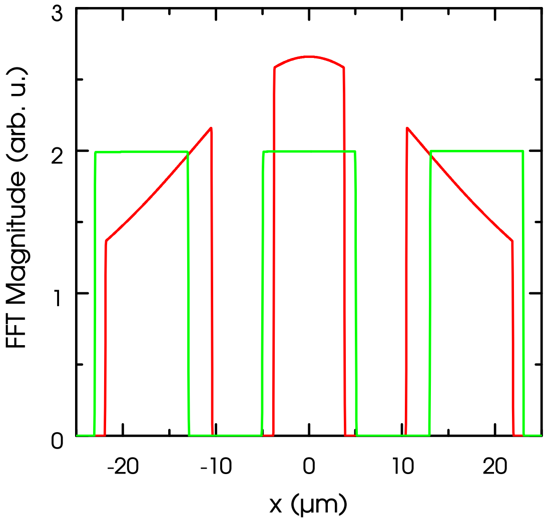

Figure 6.3: Simulated image of three 10-µm-wide patches centered at $x = -18\,\mu m$, $0\,\mu m$ and $18\,\mu m$ using the spatially non-uniform gradient described by equation 6.3 (red lines) and the same parameters as figure 6.2. For comparison, the undistorted image is plotted in green.

6.1.3 Effects of B$_0$-nonlinearities on images acquired with MRI

To estimate the effects of a nonlinear $B_{\text{gradient}}(x)$ in our samples we simulate a gradient echo for a one-dimensional MRI acquisition and describe the deviation from the linear behavior by a constant gradient G and an error function $\epsilon(x)$, which contains all the nonlinear effects, so that

$$B_{\text{gradient}}(x) = G \cdot (x + \epsilon(x)) \,. \tag{6.7}$$

For simplicity, we resort to rotations on the Bloch sphere instead of solving the time-dependent Hamiltonian. The echo sequence is implemented by a π/2- and π-rotation about the y-axis. ±π/2-pulses around the x- and y-axis form the projection pulses necessary to measure the complex gradient signal with phase cycling (c.f. section 2.4). A position-dependent rotation multiplied with the absolute gradient strength around the z-axis is inserted between the excitation and refocusing pulse for the gradient simulation. To form the MRI signal for a given value in the k-space, these steps are executed for all spins in the sample and the results are added up. To implement phase cycling, we use alternating sequences with a +π/2- and a

$-\pi/2$-projection-pulse and the difference between those experiments becomes the corresponding k-space value. This process is repeated for all k-space values to construct a k-space image. In order to reduce leakage, the k-space image is multiplied with a Blackman-Harris window and the result is Fourier-transformed using the fast Fourier transform (FFT) algorithm to obtain the image in position space.

In red, figure 6.3 plots the simulated effect of the non-linear $B_{\mathrm{gradient}}(x)$ described by equation 6.3 on the image of three 10-µm-wide patches centered at $x = -18\,\mu\mathrm{m}$, $0\,\mu\mathrm{m}$ and $18\,\mu\mathrm{m}$. For comparison, the undistorted image is plotted in green. The spatially varying gradient results in an image which is warped in x-direction by a few µm and whose amplitudes deviate strongly from the amplitudes obtained in the ideal case. These deviations are high compared to the theoretical resolution of a few nm and will render gradient microcoils unfeasible if they remain uncorrected. By reducing the field of view to smaller values such as 15 µm, which would reduce the error to less than 1 % [74], this situation can be improved. However, this approach is not viable if the size of the field of view is fixed, e.g. due to the current measurement structure, because an increased antenna-to-antenna distance, which would have the same beneficial effect as reducing the field of view, comes at the cost of a quadratically reduced gradient.

6.1.4 Correction of B_0-nonlinearities for MRI

Instead of adjusting the field of view or increasing the antenna-to-antenna distance, deviations from the linear behavior can be corrected by the method presented in this section. If the position-dependence of a nonlinear $B_{\mathrm{gradient}}(x)$ is known, the distortions to an MRI image due to these nonlinearities can be corrected by a shift and an amplitude correction [123]. We will shortly introduce this method here. All the equations are for the one-dimensional imaging performed later, but can easily be expanded to three-dimensional corrections [123]. Since we use an echo-based imaging method instead of the FID-based method in reference 123 the equations were adjusted to reflect that.

We again express

$$B_{\text{gradient}}(x) = G \cdot (x + \epsilon(x)) \tag{6.8}$$

by a constant gradient G and an error function $\epsilon(x)$. This error function transforms the Fourier transform equation 2.18 to

$$F(G) = \int C(x)\, e^{i\gamma t G(x+\epsilon(x))} \mathrm{d}x. \tag{6.9}$$

To bring this equation back to its original form as shown in equation 2.18 we introduce the coordinate transformation

$$x' = x + \epsilon(x) \tag{6.10}$$

$$\text{and} \quad \mathrm{d}x' = \left(1 + \frac{\partial \epsilon(x)}{\partial x}\right) \mathrm{d}x. \tag{6.11}$$

This transformation corresponds to a shift of the coordinates in the image so that any deviations introduced by the nonlinearity are counteracted and yields

$$F(G) = \int C'(x')\, e^{i\gamma t G x'} \mathrm{d}x' \tag{6.12}$$

if we define

$$W(x) = 1 + \frac{\partial \epsilon(x)}{\partial x} \tag{6.13}$$

$$\text{and} \quad C'(x') = \frac{C(x)}{W(x)}. \tag{6.14}$$

Therefore, a nonlinearity in $B_{\text{gradient}}(x)$ which can be expressed by a constant gradient G and the deviation from the ideal behavior $\epsilon(x)$ will result in a shifted image $C'(x')$ with amplitudes which deviate from the expected amplitudes by $W(x)$. To obtain the undistorted image from the warped image $C'(x')$, it has to be shifted according to the error function $\epsilon(x)$ (equation 6.10) and must be multiplied with the amplitude distortion function $W(x)$ (equation 6.13).

The shift (or error function) and amplitude distortion functions that are necessary to recover an undistorted image according to

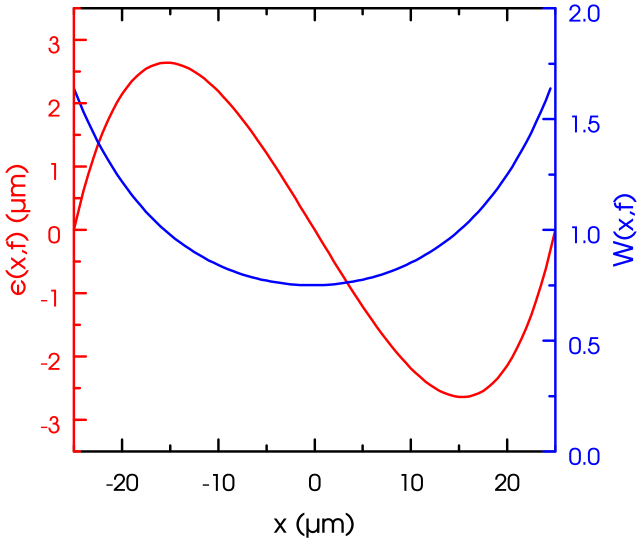

Figure 6.4: Error function $\epsilon(x, f)$ and amplitude distortion function $W(x, f)$ for the nonlinear gradient $B_{\text{gradient}}(x)$ from equation 6.3 using the parameters introduced in figure 6.2.

equations 6.10 and 6.13 are

$$\epsilon(x, f) = \frac{B_{\text{gradient}}(x) - l(x, f)}{m(f)} \tag{6.15}$$

$$\text{and} \quad W(x, f) = \frac{B'_{\text{gradient}}(x)}{m(f)}, \tag{6.16}$$

respectively. They are plotted in figure 6.4 for the nonlinear gradient introduced in equation 6.3. The shift distortion function has a maximum of 2.6 µm at $x = -15.5$ µm and at $x = 15.5$ µm, which is large compared to the theoretical resolution. In addition to the shift, the intensity of the uncorrected image varies by more than a factor of two from its minimum at $x = 0$ µm to its maximum at the edges of the field of view. By using these correction functions, the simulated, distorted image depicted by the red lines in figure 6.3 can be corrected to the undistorted image depicted by the green lines in figure 6.3.

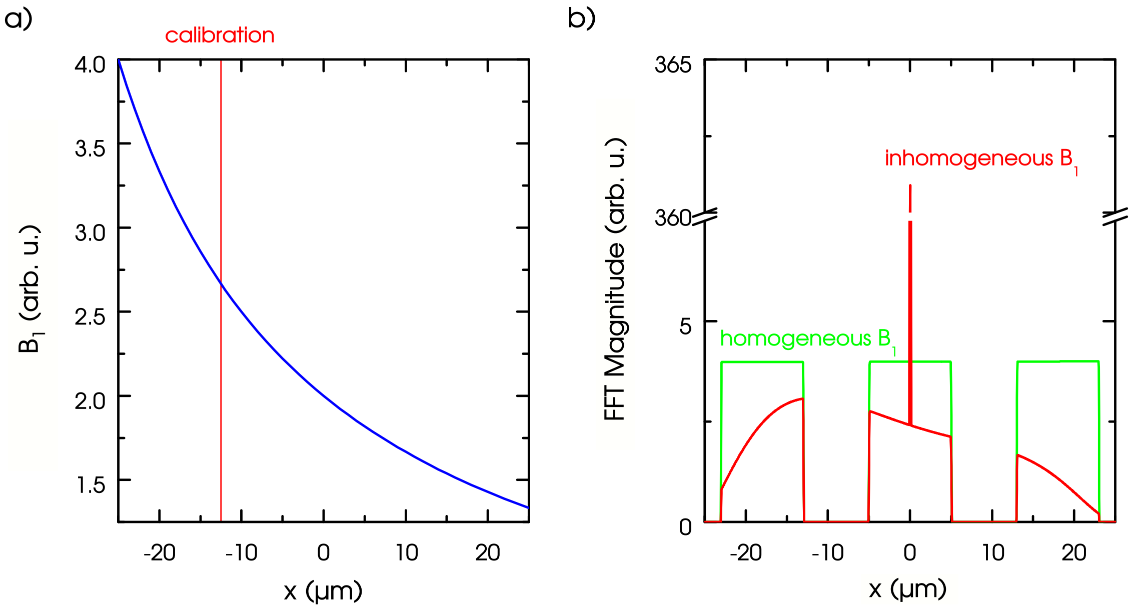

Figure 6.5: a) Magnetic field B_1 generated by one stripline antenna for a field of view of 50 µm as a function of the position x within the two stripline antennas used for gradient generation. The position used for B_1 calibration is marked with the vertical red line. b) Image of three 10-µm-wide patches centered at $x = -18$ µm, 0 µm and 18 µm with (red lines) and without (green lines) B_1-inhomogeneities.

6.1.5 Effects of B$_1$-inhomogeneities on images acquired with MRI

Since we also intend to use the gradient microcoils for the excitation of the spin signal, the spins will see a highly inhomogeneous B_1-field in addition to the B_0-nonlinearity. This B_1-inhomogeneity has an effect on the resulting image, too, because the calibration for $\pi/2$- and π-pulses only holds for a small region. To estimate the effects of B_1-inhomogeneities we again assume infinitely long current-carrying wires. Since we do not want to generate a gradient for the B_1-field, we chose to generate the B_1-field with only one wire.[1] The resulting

---

[1] Theoretically, using both stripline antennas in a Helmholtz configuration would be possible. However, this is impractical due the dimensions of the sample holder, which is greater than the wavelength of the microwave radiation and would cause significant phase deviations between the microwave signals in both stripline antennas.

B_1 as a function of the position x for a current I is known to be

$$B_1(x) = \frac{\mu_0 I}{2\pi} \frac{1}{x}. \tag{6.17}$$

Figure 6.5 a) plots $B_1(x)$ for a field of view of 50 µm as a function of the distance x from the current-carrying coil. It varies by a factor of three between its highest and its lowest value. The effects of this inhomogeneity were simulated using a gradient echo which was calibrated to the B_1-field at $x = -12.5\,\mu\text{m}$. This will yield a B_1-inhomogeneity of ±50 %. To simulate the position-dependent B_1-field we adjusted the simulation introduced in section 6.1.3 by multiplying the rotation angles induced by the microwave pulses with a factor depending on the position of the simulated spin. The resulting image is plotted in figure 6.5 b). Again, the green line shows the undistorted image and the image which is distorted due to the B_1-inhomogeneities is depicted in red. Its most prominent feature is a peak with a width of one data point at $x = 0\,\mu\text{m}$ which is not present in the undistorted image. Apart from this, the B_1-inhomogeneity does not warp the image but it has a pronounced effect on its amplitudes. This amplitude deviation could be corrected with a similar approach as for the B_0-nonlinearities, but the amplitude of the peak at $x = 0\,\mu\text{m}$ is huge compared to the other features and amplitude corrections will be at the expense of the signal-to-noise ratio. A much simpler approach to correct the B_1-inhomogeneities are adiabatic (c.f. chapter 2.5.1) or optimal control (c.f. chapter 2.5.2) pulses with a B_1-width high enough to cover the whole field of view. We will use the latter below.

6.1.6 Sample structure for electrically detected MRI

The spin system in our phosphorus-doped silicon samples is effectively two-dimensional because of the small height of 20 nm of the doping layer compared to the typical lateral feature sizes of about 10 µm. Therefore, only a two-dimensional imaging system is necessary. It can be constructed from two microcoil arrangements rotated by an angle of 90° as in reference 74. To test the applicability of the microcoils for pEDMR imaging, a one-dimensional imaging was developed. Figure 6.6 a) shows the basic structure of

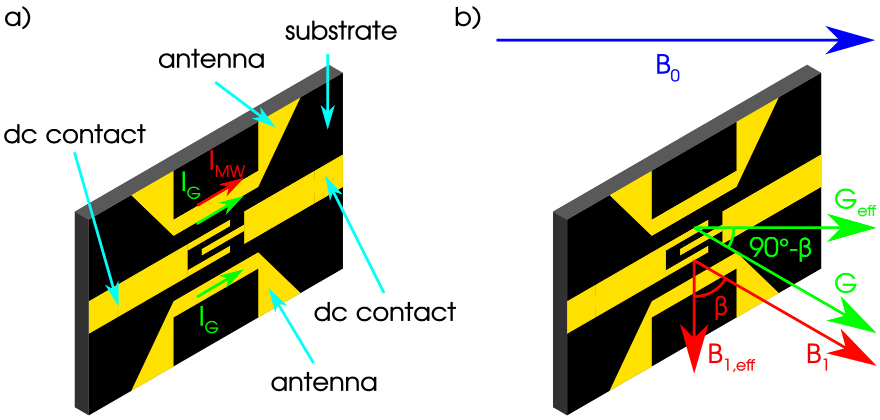

Figure 6.6: a) Sketch (not to scale) of the phosphorus-doped silicon sample used for one-dimensional imaging including the silicon semiconductor (black) and the metalizations for measurement contacts and antennas (yellow). The current I_{B_1} (red arrow), which generates the B_1-field, only flows through the upper antenna while the current I_G (green arrows), which generates the gradient field, runs through both the upper and the lower antenna. b) Microwave B_1 (red) and gradient G (green) magnetic fields with their respective effective fields G_{eff} and $B_{1,\mathrm{eff}}$ due to the angle β between the sample normal and the external magnetic field B_0 (blue).

the sample used in the imaging system. Here, the silicon sample is colored black and the metalizations for the interdigit measurement structure and microwave transmission lines are shown in a yellow color. In contrast to the structure shown in figure 3.4, a BCB layer is not necessary, because the antennas do not overlap the current measurement structure. The microwave B_1-field is generated by the current I_{B_1} flowing through the upper antenna. For the gradient field, a current I_G which runs through both the upper and the lower antenna is necessary. The electrical measurement structure consists of 3 parallel 10-µm-wide contacts with an overlap of 60 µm and a total length of 100 µm placed at a distance of 10 µm. They cover a 50-µm-wide field of view for the 10-µm-thick antennas with an antenna-to-antenna distance of 100 µm. The interdigit contacts are connected by 50-µm-wide conductors which extend to the edge of the sample where they are connected to the sample holder with wire bonds.

To excite transitions between the spin eigenstates, an oscillatory B_1-field must be orthogonal to the external magnetic field B_0. Furthermore, the gradient field G necessary for imaging has to be collinear to B_0. Since the same antennas are used to generate B_1 and G, both B_1 and G are parallel and cannot fulfill both conditions. To resolve this conflict, the sample normal is rotated by an angle $90^\circ - \beta$ with respect to B_0 as is shown in figure 6.6 b). Now, both B_1 and G have a component orthogonal and parallel to B_0, which results in an effective $B_{1,\mathrm{eff}}$ orthogonal to B_0 and an effective G_{eff} parallel to B_0. The effective fields are related to B_1 and G by $B_{1,\mathrm{eff}} = \cos(\beta)\, B_1$ and $G_{\mathrm{eff}} = \sin(\beta)\, G$, respectively. Depending on the experimental parameters, the angle β can be chosen to favor either $B_{1,\mathrm{eff}}$ or G_{eff}. For an angle of $\beta = 45^\circ$ both $B_{1,\mathrm{eff}}$ and G_{eff} are reduced by $1/\sqrt{2}$ which results in a diminished efficiency of $e = 113\,\mathrm{T\,m^{-1}\,A^{-1}}$ for an antenna-to-antenna distance of $100\,\mu\mathrm{m}$.

6.1.7 Modifications to the sample holder

For imaging experiments it is necessary to route the microwave signal I_{MW} through one of the antennas on the sample while the low-frequency gradient current I_{G} has to pass both antennas in order to generate the gradient field (c.f. section 6.3). This is achieved by two additions to the basic sample holder which are sketched in figure 6.7. Here, the path of the microwave and gradient signals are depicted with red and green lines, respectively. Firstly, a low pass filter with a cutoff frequency of 1 GHz prevents microwaves from entering the second gradient antenna while the low-frequency gradient can pass unimpeded [124]. Secondly, the DC blocks inserted in the outer part of the CPW stop all signals with a frequency of less than 2 GHz and force them into the CPS structure which guides them through the second antenna. At the microwave frequency of about 10 GHz, determined by the traveling wave tube amplifier used in our imaging experiments, a sample holder with just the outer DC block measured in a back-to-back configuration introduces about 2 dB of insertion loss [124]. The additional bond connections between the outer conductors of the CPW before and after the DC block are intended to suppress unwanted transmission modes [125].

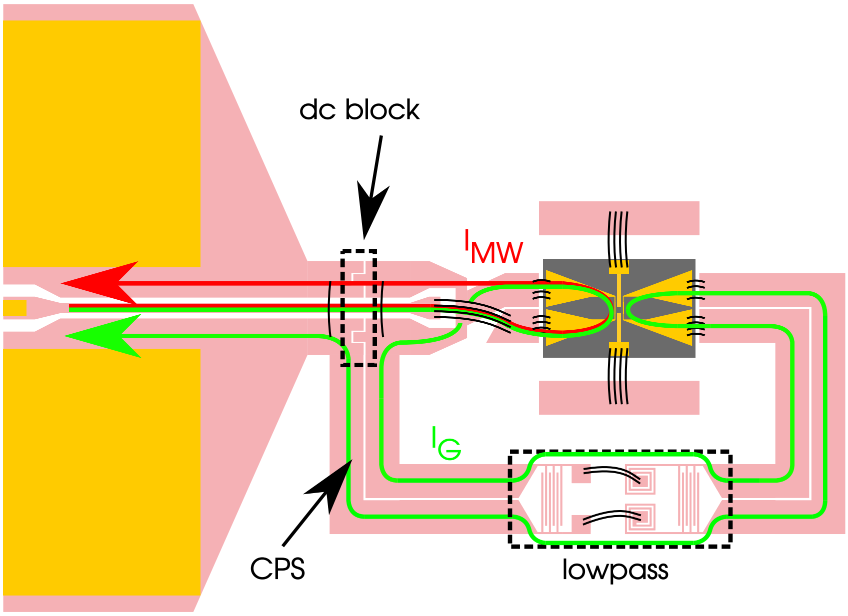

Figure 6.7: Schematic drawing of the sample holder used for imaging experiments. All transmission line traces are in a coppery color and the bond connections are shown with black lines. The microwave and gradient signals are depicted with red and green lines, respectively.

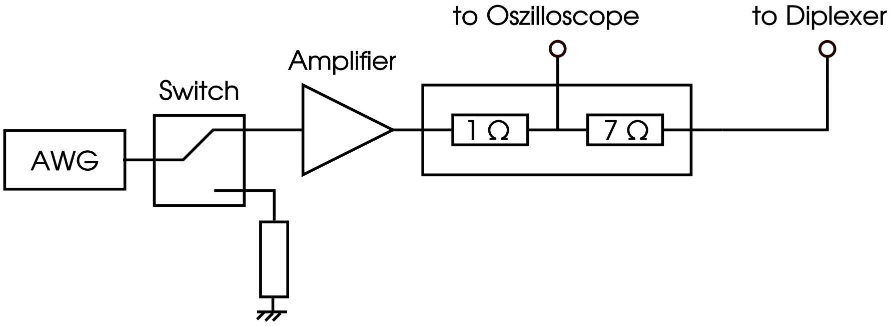

Figure 6.8: Gradient pulse setup consisting of an AWG for pulse generation, a power amplifier with low output impedance and a voltage divider for pulse measurements.

6.1.8 Modifications to the pulsing setup for gradient generation

Since our setup uses a pair of microwave antennas to generate the gradient field, which have a much better conversion factor than conventional gradient coils (c.f. section 6.1) and therefore don't need high power gradient pulse drivers, a much simpler setup than presented in reference 73 can be used. A schematic drawing of the gradient field setup is presented in figure 6.8. Similar to the RF pulse generation, an AWG (Signate PXDAC 4800) generates a gradient pulse. This pulse is attenuated to adjust its level to the maximal input power of the amplifier (Tabor A10160, output impedance 2.5 Ω, bandwidth 45 MHz, peak output voltage 34 V into 50 Ω, peak output current 1 A). The resulting pulse passes a voltage divider composed of a 1 Ω and a 7 Ω resistor, which allows for the measurement of the pulse shape with the help of an oscilloscope. Afterwards, the pulse enters the low frequency arm of the diplexer shown in figure 3.7 which routes the pulse to the sample holder.

6.2 Imaging with rectangular pulses

We start the discussion with a complex k-space image which was recorded of the sample discussed in section 6.1.6 with the gradient echo sequence shown in figure 2.8. The π/2- and π-pulse lengths were calibrated with Rabi measurements (not shown) to $\tau_{\pi/2} = 16\,\text{ns}$ and $\tau_\pi = 32\,\text{ns}$, respectively. We use a total sequence length of 1.234 µs and gradient length of 1 µs split into two 500-µs-long gradient pulses during the first and second free evolution time of the echo and sample 64 k-space values.

The real (red) and imaginary (blue) part of this complex k-space image are plotted in figure 6.9 a). The nominal abscissa values k_nominal were calculated with formulas 2.21 and 6.4 from the AWG output voltage amplitude of 0.2 V, used to generate the gradient pulses, using the fixed amplification of 10 of the gradient amplifier, an angle between the sample normal and B_0 of 45° and a total resistance of the setup of 12.5 Ω, which is caused by the voltage divider in the setup (8 Ω c.f. section 6.1.8), the internal resistance of the amplifier (2.5 Ω) and by the sample resistance of 2 Ω. Since we do not know the exact field of view of our measurement at this point, distortions due to the B_0-nonlinearity are not corrected.

Both the real and the imaginary part show oscillations which have a maximal amplitude for $k_\text{nominal} = 0\,\mu\text{m}^{-1}$ and decay completely so that there is no discernible signal for $k_\text{nominal} = 0.2\,\mu\text{m}^{-1}$. Therefore,

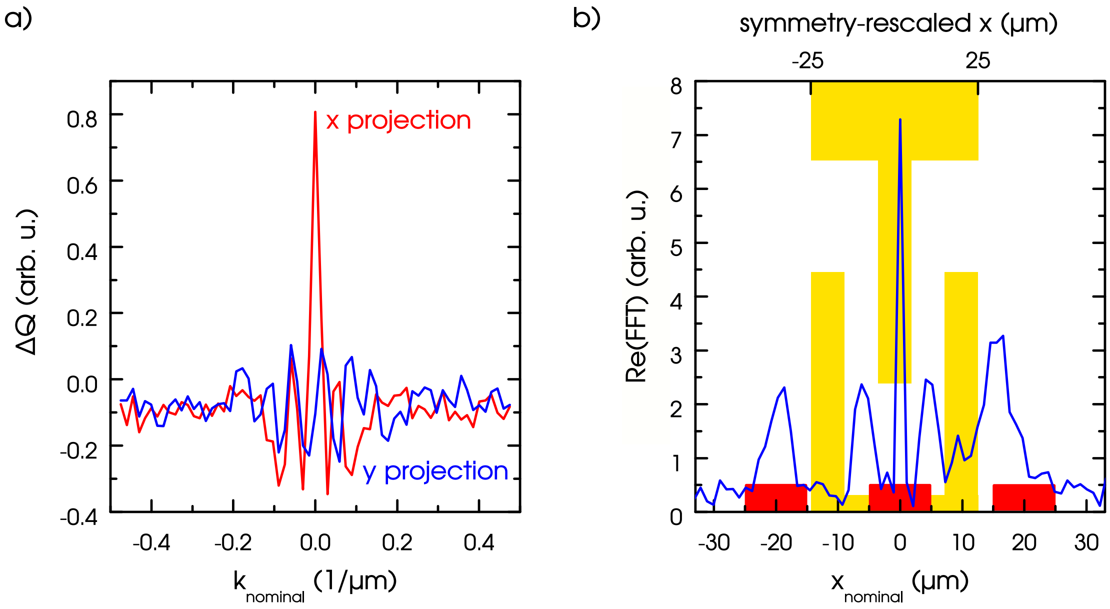

Figure 6.9: a) pEDMR signal ΔQ acquired with a gradient echo sequence using an x projection pulse (red) or a y projection pulse (blue) as a function of k_{nominal} for a bias voltage of $-0.5\,\mathrm{V}$. b) Real part of the Fourier transform of the complex valued signal shown in a). The assumed positions of the measurement contacts are depicted by the yellow sketch in the background of the plot and the positions where the contacts should be on the nominal x-scale are marked with red boxes.

a further increase of the gradient strength will not yield a higher resolution because the resolution is already limited by the waveform of the k-space image. The real and the imaginary part show a non-zero background although the gradient echo was measured using phase cycling [59]. This is probably caused by the B_1-inhomogeneity present in the sample (c.f. section 6.1.5).

A Fourier transform of this k-space image yields the position space image whose signal is completely contained in the real part of the Fourier transform which is plotted in figure 6.9 b). It has five distinct peaks at the nominal abscissa values $x_{\mathrm{nominal}} = -19\,\mu\mathrm{m}$, $-6\,\mu\mathrm{m}$, $0\,\mu\mathrm{m}$, $4.5\,\mu\mathrm{m}$ and $15.5\,\mu\mathrm{m}$. The peak at $x_{\mathrm{nominal}} = 0\,\mu\mathrm{m}$ is only one data point wide and is caused by the non-zero offset in the k-space signal.

This leaves four peaks which can be assigned to the three contacts if we assume that the signal is only generated in the space between the contacts and outside of the interdigit contact structure. We will discuss this assumption in more detail in section 6.5. To illustrate this, a two-dimensional sketch of the interdigit contact structure is drawn in yellow in the background of the plot at the positions where we expect the contacts to be. For clarity, we have added a symmetry-rescaled x-scale on top of figure 6.9 b). These symmetry-rescaled positions deviate strongly from the positions where the contacts should be on the nominal x-scale, which we have marked with red rectangles in figure 6.9 b).

There are three possible causes for this difference. Firstly, due to the B_0-nonlinearity, the measured peaks are shifted compared to their true position. Secondly, the actual gradient strength could be weaker than calculated and therefore the values on the abscissa are wrong. Thirdly, if the origin of the peaks at $-19\,\mu\text{m}$ and at $15.5\,\mu\text{m}$ is outside of the interdigit contact structure (total width $50\,\mu\text{m}$) as indicated in figure 6.9 b), the field of view has to be greater than the $50\,\mu\text{m}$ defined by the outer edges of the contacts.

6.3 Imaging with optimal control pulses

To remove the aberrations in the image caused by the B_1-inhomogeneity, a new cooperative optimal control echo (c.f. section 2.5.2) was calculated. It exhibits an increased relative ν_1-bandwidth of $\pm 50\,\%$ around a lower mean ν_1-frequency of 20 MHz compared to the pulses shown in the last chapter, while the ν_0-bandwidth of 20 MHz remains unchanged. Its simulated z-polarization is plotted in figure 6.10 as a function of $\Delta\nu_0$ and ν_1 and meets the optimization goals (horizontal and vertical green lines) very well.

Using this pulse sequence a complex k-space image (c.f. figure 6.11 a)) was recorded with the same settings as in section 6.2 with the exception of the total sequence length which was adjusted to $2.234\,\mu\text{s}$ to accommodate the length of the optimal control echo of 450 ns. Here, the background for $k_{\text{nominal}} = \pm 0.5\,\mu\text{m}^{-1}$ is much closer to zero than in figure 6.9 a) and the total amplitude of the image has increased by a factor of two.

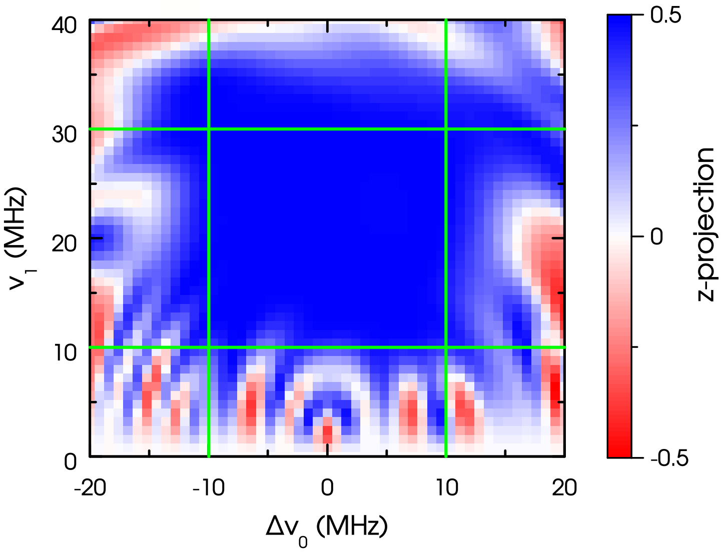

Figure 6.10: Simulated z-projection after the cooperatively optimized echo for imaging experiments as a function of $\Delta\nu_0$ and ν_1. The vertical and horizontal green lines depict the goals used during optimization.

The position space image (c.f. green plot in figure 6.11 b)) is again obtained by Fourier transforming the k-space image. Compared to the image measured in section 6.2 (c.f. blue plot in figure 6.11 b)) it has a much smaller peak at $x = 0\,\mu\text{m}$, which is possibly due to the better robustness of the optimal control pulse to B_1-inhomogeneities. That this peak does not vanish completely may either be caused by parts of the ensemble which lie outside of the 50-µm-wide field of view and therefore have an even higher inhomogeneity than assumed during the pulse optimization or by other spin-independent signals which are not completely filtered by the echo sequence. The amplitude of the inner peaks increases by a factor of two while the amplitude of the outer peaks is three times higher than those in the image captured with rectangular pulses. Therefore, for all further experiments the cooperatively optimized echo was used.

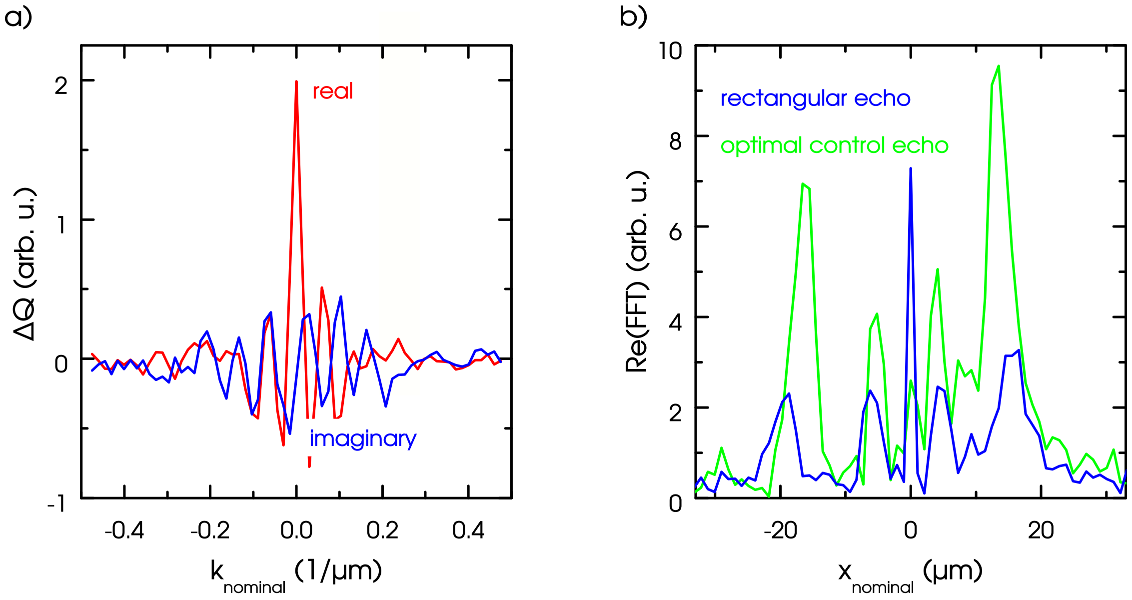

Figure 6.11: a) pEDMR signal ΔQ acquired with a gradient echo sequence using an x projection pulse (red lines) or a y projection pulse (blue) as a function of the gradient k_{nominal} for a bias voltage of −0.5 V. b) Real part of the Fourier transform of the complex valued signal obtained with an optimal control echo sequence shown in b) (green line) and that obtained by an echo sequence with rectangular pulses from figure 6.9 a) (blue line).

6.4 Correction of B_{gradient}-nonlinearities

We now turn to the correction of B_{gradient}-nonlinearities. This requires an exact knowledge of the field of view f, because the strength of the nonlinearity depends on it. In the case of the sample introduced in section 6.1.6, we use two measurements with a bias voltage of 0.5 V and −0.5 V to determine f.

Figure 6.12 shows the real part of the Fourier-transformed image for both voltages as a function of the calculated position in red and blue, respectively. Both images were measured with an increased gradient (AWG output voltage amplitude of 0.3 V, gradient length of 1.1 μs and 128 gradient points). To simplify the analysis, the amplitude of the graph for 0.5 V was reduced by a factor of two.

The positions of the two outer peaks do not depend on the bias voltage while the inner two peaks shift slightly. We will have a closer

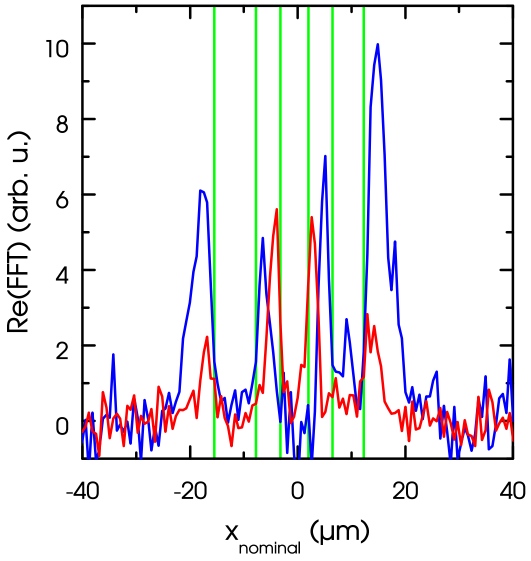

Figure 6.12: Real part of the Fourier-transformed k-space image for a bias voltage of 0.5 V (red) and −0.5 V (blue). The vertical green lines show the $x_{\text{contact, nominal}}$ used for the nonlinearity correction.

look at this behavior in section 6.5. At the moment, only the regions which do not show a signal are important, because if we continue to assume that the EDMR signal is only generated in the space between the interdigit contacts, we can use the sharp edges of the peaks (vertical green lines in figure 6.12) to find a relationship between the photolithography-defined contact positions and the positions on the nominal x-scale. The values of the photolithography-defined contact edges x_{contact} and their counterparts on the nominal x-scale $x_{\text{contact, nominal}}$ are listed in table 6.1.

x_{contact} (µm)	−25	−15	−5	5	15	25
$x_{\text{contact, nominal}}$ (µm)	−15.5	−7.8	−3.2	1.9	6.5	12.3
fit result (µm)	−15.0	−7.9	−3.1	1.2	6.0	13.1

Table 6.1: Finger edges as defined by the photolithography process x_{contact}, as measured using the nominal x scale $x_{\text{contact, nominal}}$ and as calculated from the fit of equation 6.19.

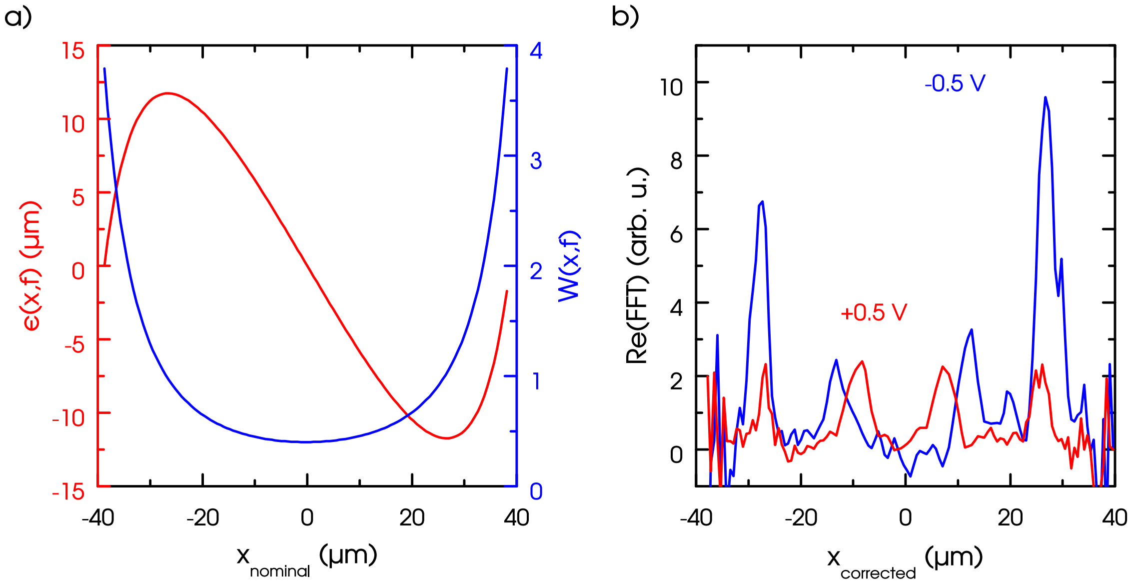

Figure 6.13: a) $\epsilon(x,f)$ (red) and $W(x,f)$ as a function of the position x. b) Shift- and amplitude-corrected version of figure 6.12 a).

To translate from the photolithography-defined positions x_{contact} to the measured positions $x_{\text{contact, nominal}}$, we use

$$x_{\text{contact, nominal}} = g\left(x_{\text{contact}}, f, d, f_{\text{m}}\right) \tag{6.18}$$

$$= \frac{f_{\text{nominal}}}{f} \cdot \left(x_{\text{contact}} + d + \epsilon\left(x_{\text{contact}} + d\right), f\right). \tag{6.19}$$

The shift d accounts for any displacement of the interdigit contacts from their intended position due to alignment errors during the manufacturing and $\epsilon(x + d, f)$ (c.f. equation 6.15) distorts the position according to the B_{gradient}-nonlinearities. To account for slight deviations in the calculated positions caused by differences between the calculated and the actual gradient, the resulting positions are stretched or compressed by the ratio of the nominal and fitted field of view f_{nominal} and f, respectively. To determine f and d we fit $g(x, f, d, f_{\text{nominal}})$ to the nominal positions $x_{\text{contact, nominal}}$ using a Levenberg-Marquardt algorithm. This results in $f = 77.4\,\mu\text{m}$ and $d = -0.9\,\mu\text{m}$ for the nominal field of view $f_{\text{nominal}} = 80\,\mu\text{m}$ which produces a nice fit to the measured positions (c.f. table 6.1). An alignment error of $-0.9\,\mu\text{m}$ is in agreement with optical microscope images which do not show a deviation between the lithography markers used for the antennas and the interdigit contact structure.

The resulting field of view agrees well with the calculated field of view and hence confirms our estimation of the magnetic field gradient. The distortion functions $\epsilon(x,f)$ and $W(x,f)$, which correspond to the shift and the amplitude-deviation of the uncorrected image, are plotted in figure 6.13 a). Due to the large field of view, the corrections with a maximal shift of 11.7 µm and amplitude variations from 0.4 to 3.8 are rather large compared to those caused by the intended field of view of 50 µm. Using these distortion functions, we can transform the positions and amplitudes of figure 6.12 a) to recover the undistorted image shown in figure 6.13 b). Here, $x_{\text{corrected}}$ is the transformed x_{nominal} obtained by the application of $\epsilon(x,f)$. The relative heights between the inner and outer peaks deviate significantly from those in figure 6.12 since the outer peaks are amplified considerably by the correction. Unfortunately, this is also true for the noise in the outer regions of the image, which increases, too. All further measurements in this section are corrected for the B_{gradient}-nonlinearity using the field of view and shift determined here.

6.5 Physical interpretation

In order to elucidate the origins of the EDMR signals, images were recorded for different bias voltages. Figure 6.14 plots B_{gradient}-nonlinearity-corrected excerpts of the real parts of Fourier-transformed k-space images for bias voltages of 1 V (blue), 0.5 V (red) and 0.25 V (green) for positive (panels a) and b)) and negative bias (panels c) and d)). To ease the comparison, all images were normalized and the figures which depict the inner peak around $x = 10\,\mu\text{m}$ (figure 6.14 a) and c)) as well as the images corresponding to the outer peak starting at $x = 25\,\mu\text{m}$ (figure 6.14 b) and d)) are plotted above each other. Since the images are symmetrical, we only display the peaks corresponding to $x \geq 0$.

For all images the width of the region which exhibits a signal increases with higher absolute bias voltages. If the bias voltage is reversed, the position of the areas with signal in figure 6.14 b) and d) do not change significantly whereas the position of the signal shifts substantially from figure 6.14 a) to figure 6.14 c).

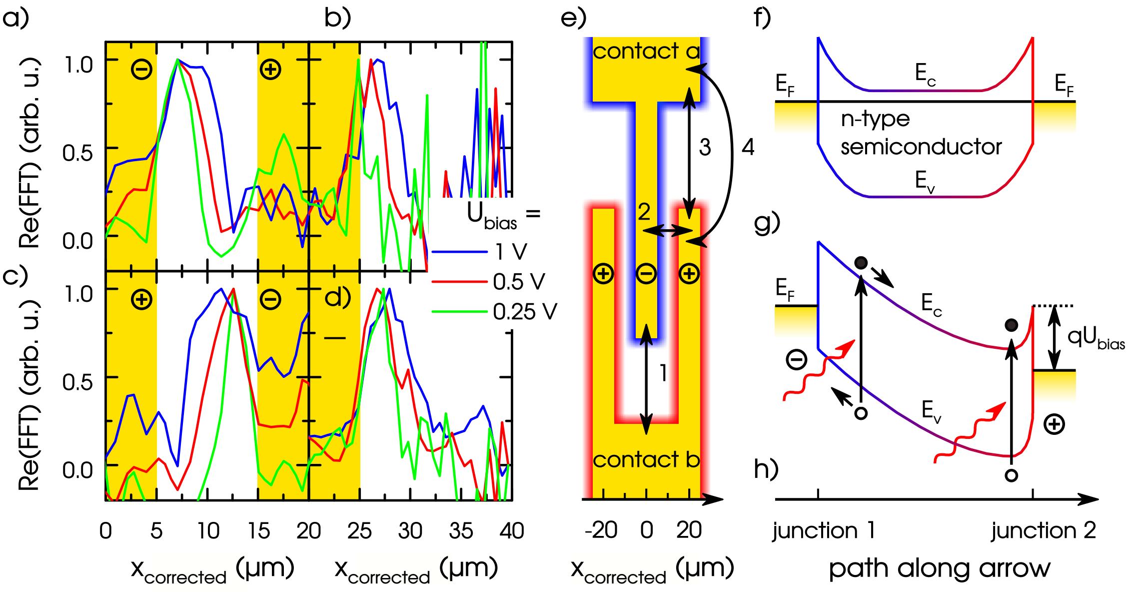

Figure 6.14: Excerpts of the real parts of Fourier-transformed k-space images for the bias voltages of 1 V (blue), 0.5 V (red) and 0.25 V (green) for positive (panels a) and b)) and negative bias (panels c) and d)). The images a) and c) display the inner peak around $x = 10\,\mu\text{m}$ whereas the images b) and d) depict the outer peak starting at $x = 25\,\mu\text{m}$. All images are normalized and the respective bias directions are depicted with the black + and – signs. e) Sketch of the interdigit contact structure including the bias applied to the contacts depicted with + and – signs and a graphical representation of the Schottky diode depletion zones around the contact in red and blue. Band diagram of a metal-semiconductor-metal structure without f) and with bias g). Electrons and holes are depicted by full and empty circles, respectively. An incident photon is shown in red. h) Location of the band diagram along one of the arrows in panel e). Panels f) and g) are adapted from [126].

At the Schottky contacts of our device, there exists a depletion zone in the region around the contact. Figure 6.14 e) shows the interdigit contact structure with a representation of this depletion zone. For clarity, the depletion zones are colored red and blue depending on the bias of the contact to which they belong and the numbered black arrows indicate possible pathways for the electrons and holes between the cathode and the anode. Along these arrows the band structure of our device is that of a metal-semiconductor-metal (MSM) photodetector [126]. In the case of no applied bias voltage (c.f. figure 6.14 f)), the Fermi levels E_F of the metal contact and the semiconductor align, which leads to an upward band bending of the conduction and the valence band at the junctions between the semiconductor and the metal. If a bias U_{bias} is introduced between the contacts (c.f. figure 6.14 g)), the energy of the anode is reduced with respect to the cathode by qU_{bias}, where q is the elementary charge of an electron. This will increase the depletion width W_{reverse} of the reverse-biased Schottky junction and decrease the width W_{forward} of the forward-biased Schottky junction.

Depending on the bias voltage and the built-in voltage of the junctions there are three distinct scenarios. If the combined width of the two Schottky junctions is smaller than the distance between the electrodes, the band structure is essentially the one of figure 6.14 f) with a superimposed slope [127]. In the regime between the reach through voltage U_{rt}, where the combined width of both depletion regions equals the distance between the electrodes (c.f. figure 6.14 g)), and the flat band voltage U_{fb}, which is the bias voltage that leads to a vanishing depletion width of the forward-biased junction, the slope of the bands at the reverse-biased junction decreases until it vanishes. Bias voltages which are even higher increase the overall slope of the bands resulting in a more or less homogeneous slope throughout the device. We can exclude this situation from the discussion, because a homogeneous slope rules out the position-dependence of the observed signal. Rather, we have to discuss the regime before the flat-band condition is reached.

The spin-dependent recombination observed in our samples involves electrons from the conduction band which are trapped at phosphorus donors. Recombination of those charge carriers is only relevant when they are not majority carriers. This is the case in the large reverse-biased depletion zone, where the charge carriers present are photoexcited. In contrast, in the flat region of the n-type doped semiconductor, electrons are the majority carriers. The same is effectively true in the forward-biased narrow depletion zone at the opposite Schottky contact. Therefore, we can immediately understand that the ^{31}P-P$_{\mathrm{b0}}$ recombination is only observed in our spatially resolved electrically detected MRI at the reverse-biased Schottky contact and that the region of spin-dependent recombination increases with increasing width of that depletion zone.

With this position dependence in mind, we turn back to the assignment of the signals to positions in our interdigit contact structure. We can exclude current paths number one and three (c.f. figure 6.14 e)), because any changes under a voltage increase or reversal will happen parallel to our antenna and should not change the image for this reason. For current path number four any changes due to a reversal of the bias voltage will be perpendicular to the imaging direction, because the depletion region changes from contact a to contact b or vice versa. Hence, it can't be responsible for the change from figure 6.14 a) to c). An increase in bias will result in a larger depletion region and should therefore result in a signal over a larger region. This fits the changes in figure 6.14 b) and d) which are therefore attributed to current path number four. Only current path number two will change the position of the depletion region under a bias reversal and can therefore be assigned to figure 6.14 a) and c). Therefore, the assumption that the signal originates from current path number two and number four made in section 6.2 is valid.

Under the assumption that the width of the signal in figure 6.14 a) and c) represents the width of the depletion region, we can estimate the amount of ionized donors N_{D}^{+} and the built-in voltage U_{bi} of the Schottky junction. To find the depletion width W_{D} as a function of the bias voltage U_{bias}, we use the Fourier-transformed k-space images of the inner peak for different bias voltages as shown in figure 6.15 a) and b). The value for W_{D} is then extracted from the onset and termination of the EDMR signal (vertical black lines in figure 6.15 a) and b)) and plotted in figure 6.15 c). The depletion width of a Schottky junction is [126]

$$W_{\mathrm{D}} = \sqrt{\frac{2\epsilon_{\mathrm{S}}}{qN_{\mathrm{D}}^{+}}\left(U_{\mathrm{bi}} - U_{\mathrm{bias}} - \frac{kT}{q}\right)} \tag{6.20}$$

with the permittivity of the material ϵ_{S}, the elementary charge q, the Boltzmann constant k and the temperature T. Since most of the voltage drop will occur over the reverse-biased junction [127],

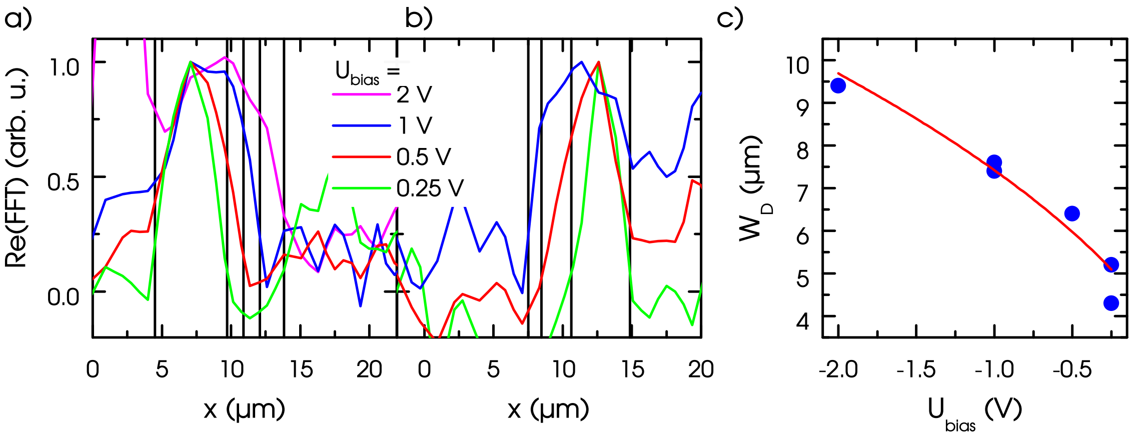

Figure 6.15: Fourier-transformed k-space images of the inner peak for the bias voltages of 2 V (pink), 1 V (blue), 0.5 V (red) and 0.25 V (green) for positive (a) and negative bias (b). The vertical black lines mark the assumed width of the depletion region for each bias voltage. c) Depletion width W_D as a function of the bias voltage U_bias. A fit of equation 6.20 is plotted in red.

we ignore the voltage drop over the forward-biased junction and assume that the bias voltage equals the voltage drop over the reverse-biased junction. A fit of this equation to W_D yields the built-in voltage U_bi and the density of ionized donors N_D^+. The result $U_\mathrm{bi} = 0.42\,\mathrm{V}$ strongly depends on the chosen values for the onset and the termination of the signal and is therefore only a rough guess. In contrast, $N_\mathrm{D}^+ = 3.3 \cdot 10^{13}\,\mathrm{cm}^{-3}$ doesn't change much under the same variations. However, this model assumes a homogeneously doped MSM device. In contrast, we investigate a system where the doping and the monitored recombination are only present in a 20-nm-thick surface layer. It is therefore not surprising that the quantitative results obtained are difficult to interpret.

6.6 Determination of the imaging resolution

Due to the high nonlinearity of the gradient field, the resolution of the gradient image cannot be extracted from the discretization Δx of the Fourier transform in figure 6.13 c) because of the rather drastic warping of the image. To estimate the achievable resolution, we

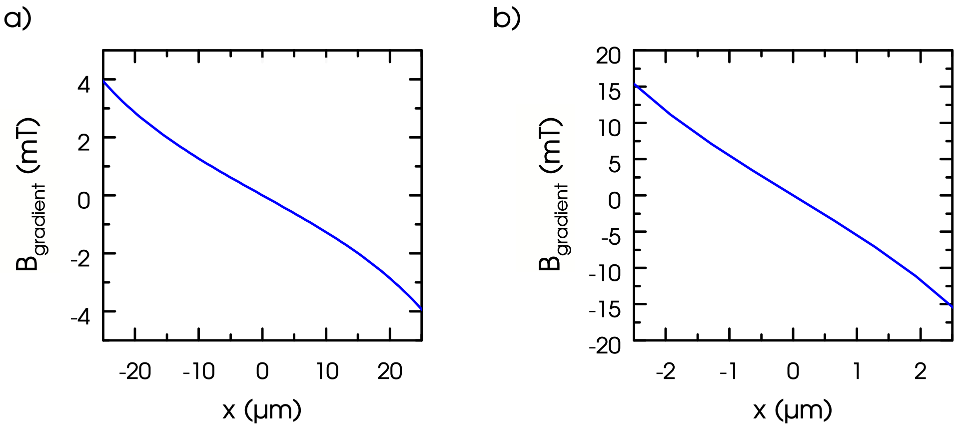

Figure 6.16: Simulation of the magnetic field B_0 as a function of the position between the gradient antennas for an antenna width of 10 µm and an antenna height of 0.5 µm. The antenna-to-antenna distance is 100 µm for panel a) and 10 µm for panel b).

calculate the gradient at $x = 0\,\mu\mathrm{m}$, which is the smallest gradient in the image. From the amplitude correction function (c.f. equation 6.16) we find that the deviation of the true gradient from the linear gradient is $W(x = 0\,\mu\mathrm{m}, f = 77.4\,\mu\mathrm{m}) = 0.4$ in our structure so that we overestimate $G(x = 0\,\mu\mathrm{m})$ by a factor of 2.5 and the true resolution at the center of the image is 1.54 µm instead of the resolution of the Fourier transform discretization $\Delta x = 0.614\,\mu\mathrm{m}$. The resulting efficiency is $e = 47.5\,\mathrm{T\,m^{-1}\,A^{-1}}$ for a current of 222 mA and at a sample angle of 45° (c.f. section 6.1.6). This is 42 % of the expected efficiency (c.f. section 6.1).

The sample in the sample holder has a resistance of $R = 2\,\Omega$, which will yield a maximal resolution of $\Delta x = 17\,\mathrm{nm}$ for this efficiency using equation 6.2 ($P_{\mathrm{mean}} = 1\,\mathrm{W}$, $t = 1\,\mu\mathrm{s}$, $t_{\mathrm{seq}} = 1\,\mathrm{ms}$, $N = 1$). To achieve this resolution, a current of 8.4 A would be necessary. For comparison, our single stripline antennas can survive microwave pulses with a power of 200 W for a duration of 10 µs at a repetition rate of 2 ms, which corresponds to a mean current of 2 A through a 1 Ω antenna as calculated with the Thevenin theorem [128]. The gradient pulse necessary for these resolutions delivers about 17 times the power but for a tenth of the duration of the microwave pulse, so that an antenna might survive this, but barely.

If we stay within the limits of this setup, a maximal current of $I = 1.0\,\mathrm{A}$ obtainable with the power amplifier yields a resolution of $\Delta x = 0.34\,\mu\mathrm{m}$ for the same gradient pulse lengths of $1.1\,\mu\mathrm{s}$ as used in the experiment. A lower antenna-to-antenna distance of e.g. $10\,\mu\mathrm{m}$ should result in an increased efficiency and hence a resolution which is higher by a factor of 100 if infinitely thin and infinitely long wires are assumed. This approximation will only hold if the dimensions of the antenna are scaled proportional to the antenna-to-antenna distance, which will partially diminish the resolution gains due to a higher antenna resistance.

However, electrostatic simulations with the software package COMSOL show that it is not necessary to change the dimensions of the antenna when the antenna-to-antenna distance is reduced. For the dimensions of the antenna structure used in these experiments, the simulated magnetic field (c.f. figure 6.16 a)) has an efficiency of $87\,\mathrm{T\,m^{-1}\,A^{-1}}$ at an angle of 45°. This value is slightly smaller than the efficiency of $113\,\mathrm{T\,m^{-1}\,A^{-1}}$ predicted by the calculation assuming infinitely long wires. If we compare these values to the measured efficiency in this section, we find that our setup reaches 55 % of the simulated value. For a reduced antenna-to-antenna distance of $10\,\mu\mathrm{m}$ the magnetic field simulations (c.f. figure 6.16 b)) show that the efficiency increases to $3.8\,\mathrm{kT\,m^{-1}\,A^{-1}}$ if the dimensions of the single antennas remain the same. If we factor in that our setup's efficiency reaches 55 % of the simulated value, this should result in a resolution of 7.8 nm for a current of 1 A and a gradient pulse length of $1.1\,\mu\mathrm{s}$ without any negative effects on the gradient linearity compared to the higher antenna-to-antenna distance. Since these parameters result in a mean dissipated power of about 1 mW (for a sequence length of $T_{\mathrm{seq}} = 2.234\,\mathrm{ms}$ and a total antenna resistance of $2\,\Omega$), the thermal budget of 1 W is not used and the resolution will improve linearly with the gradient length. A sample with a longer coherence time (e.g. [8, 11]) should allow for gradient pulses with a length of up to $500\,\mu\mathrm{s}$ (limited by the T_2-time of the sample) and a resolution of $0.16\,\text{Å}$ ($P_{\mathrm{mean}} = 1\,\mathrm{W}$, $T_{\mathrm{seq}} = 2.234\,\mathrm{ms}$). This resolution is a factor of 200 higher than the resolution demonstrated in reference 74.

Such a high resolution will require a sensitivity close to single shot-single spin readout to keep the measurement time within realistic limits. For phosphorus donors in silicon, reference 129 achieves this goal with a single electron transistor (SET). This transistor has read-out fidelities higher than 90 %, but requires temperatures around $T = 200\,\mathrm{mK}$, which are generated in a dilution fridge. Dilution fridges reach a cooling power of up to 500 µW (Oxford Triton Cryofree). Since the cooling power cannot be used completely to counter the effects of the gradient coils, we estimate that a possible imaging system would have a thermal budget of 10 µW for the dissipation by the gradient coils. The resistivity of one aluminum microwave antenna with a cross section of $100\,\mathrm{nm}^2$ and a length of 500 nm is about 1 Ω [18][2], if we assume that the cryogenic conductivity of aluminum is lowered by a factor of 3.5 compared to its room temperature value [18]. We choose an antenna-to-antenna distance of 1 µm, which is large enough to place the SET and its connections within the antennas [18]. With a gradient length of $t = 1\,\mu\mathrm{s}$ and a sequence length of $t = 1\,\mathrm{ms}$ this will result in a resolution of $\Delta x = 4.6\,\text{Å}$. Even if the conditions are tightened so that the thermal power has to stay below 10 µW throughout the gradient sequence, a gradient pulse with a length of $t = 293\,\mu\mathrm{s}$ will yield a resolution of 0.5 Å, which is about a tenth of the silicon lattice constant and should allow to map the EDMR signal with atomic precision. It requires 3.24 million acquisitions to cover an area of interest of about 90 nm times 90 nm [129] with this resolution. Assuming 100 acquisitions at each k-space value and a sequence time of 1 ms this will require a total acquisition time of 90 h, which appears experimentally feasible.

6.7 Improvements to the current measurement interdigit structures

With the results from section 6.5 we can optimize the dimensions of the interdigit current measurement structures used to contact the sample for future experiments. Firstly, since the area beneath the contact doesn't exhibit much signal, it should be reduced as far as possible. A contact width of about 1 µm can be reliably

---

[2] Aluminum should be superconducting at these temperatures, but the current densities used in our experiments are well above the critical current densities for this material.

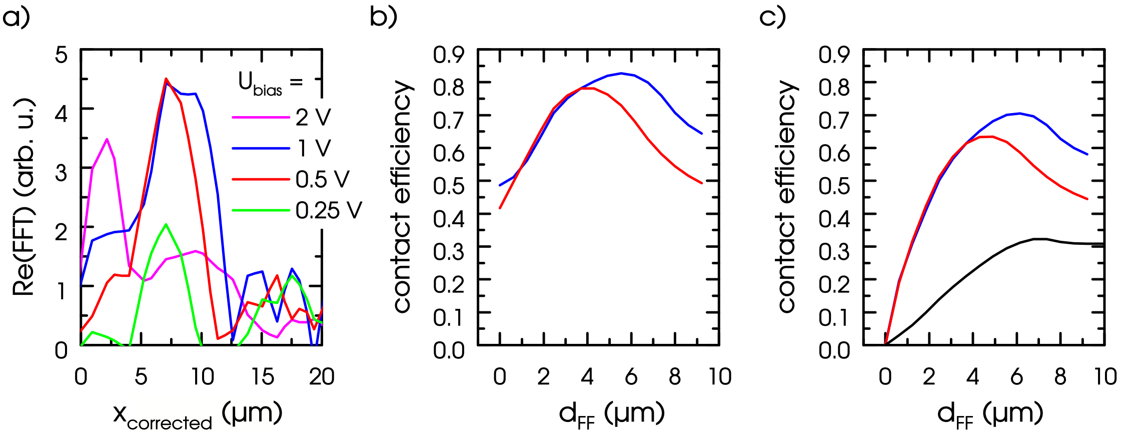

Figure 6.17: a) Normalized Fourier-transformed k-space images of the inner peak for bias voltages of 2 V (pink), 1 V (blue), 0.5 V (red) and 0.25 V (green) using positive bias. b) Mean contact efficiency as a function of the finger-to-finger distance d_{FF} for the bias voltages of 1 V (blue line) and 0.5 V. c) Mean contact efficiency including the shading effect of 1-µm-wide contact fingers as a function of d_{FF}. For comparison, the effect of a 10-µm-wide contact at a bias voltage of 1 V is plotted in black.

fabricated with UV lithography [130] so that this is the optimal width if electron beam lithography is not available or desired. The intensity of the EDMR signal is maximal for bias voltages of 0.5 V and 1 V (c.f. figure 6.17 a) so that the experiment should run within these parameters. Secondly, to optimize the distance d between interdigit contacts, we estimate the efficiency of the contact as follows: First, the plots in figure 6.17 a) are normalized to their shared maximum at $x \approx 6\,\mu m$, because we assume this is the maximal achievable signal intensity. We assign a local efficiency of 1 to this position. Afterwards we calculate the mean “contact efficiency by integrating from $x = 5\,\mu m$ up to a theoretical contact-to-contact distance d_{FF}. The resulting dependency of the contact efficiency on d_{FF} are plotted in figure 6.17 b) for the bias voltages of 1 V and 0.5 V. They show distinct maxima for $d_{FF} = 3.5\,\mu m$ and $d_{FF} = 6\,\mu m$, respectively. Since no signal is generated beneath the contacts, we have to take the non-zero width of the contacts into account and multiply this efficiency by the geometric efficiency $g = \frac{d_{FF}}{d_{FF}+1\,\mu m}$ of the contacts.

This slightly changes the total efficiency (c.f. figure 6.17 c) and the respective maxima for a bias of 0.5 V and 1.0 V shift to $d_{\mathrm{FF}} = 4\,\mu\mathrm{m}$ and $d_{\mathrm{FF}} = 6\,\mu\mathrm{m}$, respectively. Therefore, the optimal contact-to-contact distance lies in this region and should increase the signal by about a factor of 2 when compared to the typical configuration with 10-µm-wide fingers at a distance of 10 µm (black line in figure 6.17).

6.8 Summary and outlook

In summary, we have demonstrated the use of planar gradient “coils” for position-dependent EDMR measurements inside a cryostat with a sample-limited resolution of 1.54 µm, which could be increased to 0.34 µm without changes to our setup if a sample requires this resolution. Effects due to gradient nonlinearity and B_1-inhomogeneity were effectively removed by analytical corrections to the measured data and the use of an optimal control echo for detection. This has allowed us to measure the position-dependent EDMR signal for the interdigit contact structures typically used in EDMR experiments and to construct a model which explains these features with the band structure of an MSM photodetector. Based on these results, we propose a new geometry for interdigit contact structures with a contact width of 1 µm and a contact-to-contact-distance of 5 µm which should double the signal compared to the contact structures used up to now. Single spin detection via electrical measurements has been reached by Morello et al. [129]. Using the approach investigated here, mapping the EDMR signal in their sample geometry seems feasible, and should therefore allow to measure the phosphorus donor electron wave function with a resolution of 0.5 Å.

7

EDMR of nitrogen vacancy centers in diamond

With its long coherence time [131] and optical fluorescence detection [132], the nitrogen vacancy center NV^- in diamond is a promising candidate for quantum applications. These features have enabled its use, e.g. as a quantum sensor for magnetic fields [133, 134] and temperature [135], for scanning-probe spin imaging [136] and structure determination [137]. However, the spin readout, which has been optical until now, has drawbacks: it is highly inefficient, requiring several 100 repetitions for a single spin readout, and cumbersome, because it requires the use of a confocal microscope in combination with an avalanche photodetector. Electric spin readout appears attractive to surmount these limitations. It could enable access to NV^- centers in dense arrays, with a spacing limited by the few-nm-small feature size of electron beam lithography [138] rather than the optical wavelength. It might, moreover, provide a way to read out other spin defects [139–141], potentially including optically inactive ones. Two methods for electric readout of NV^- centers have been demonstrated, based on non-radiative energy transfer to graphene [142] and direct photoionization of the NV^- centers in the diamond host crystal (photocurrent detection of magnetic resonance, PDMR) [143]. Both methods, however, have until now only been used with cw spin manipulation and have therefore remained limited to NV^- detection. Here, we introduce a scheme based on both pulsed spin manipulation and pulsed photoionization to truly read out the spin state of NV^- centers electrically after coherent control and demonstrate it on small ensembles. We employ this scheme to establish a quantitative model of photoionization, simulate the readout efficiency and predict that under optimized conditions pulsed electric readout could outperform optical fluorescence detection. This chapter is based on reference 144[1].

7.1 The NV center

The NV center is a point defect in the diamond lattice where a substitutional nitrogen atom and a vacancy are neighbors [145, 146]. In its uncharged state NV^0 it consists of five electrons of which three can be attributed to the dangling-bonds of the silicon vacancy and two correspond to two of the five valence electrons of the nitrogen atom, which are not in a covalent bond to surrounding carbon atoms. Of these five electrons, only one electron remains unpaired resulting in a total spin of $S = \frac{1}{2}$. This spin should be detectable using ESR, but only an excited state of the NV^0 has been measured using ESR to our knowledge [147]. However, the negatively charged NV^- center, which consists of six electrons in total [148, 149], can be detected using ESR. Depending on the Fermi level, the NV center is in either of those two charge states [150, 151] and can be switched from NV^- to NV^0 using green illumination [152–154]. In NV^- the additional electron forms a spin triplet state with the formerly unpaired electron resulting in a total spin of $S = 1$. Its Hamiltonian

$$\mathcal{H} = g_\mathrm{e}\mu_\mathrm{e}\vec{S}\vec{B}_0 + D\left(S_z^2 - \frac{1}{3}S(S+1)\right) + \vec{S}\hat{A}\vec{I} \tag{7.1}$$

contains a Zeeman interaction, a zero-field splitting due to fine-structure effects and a hyperfine coupling to surrounding nuclei. D is the zero-field splitting parameter, $\hat{A}$ is the hyperfine tensor

---

[1] © 2017 American Physical Society.

and the quantization axis z is aligned along the NV^- center's axis. Effects due to electric fields and strain are ignored in this description because they are not studied within the scope of this work. The zero-field splitting leads to different energies for the eigenstates corresponding to $m_\mathrm{S} = 0$ and $m_\mathrm{S} = \pm 1$ if no magnetic field is present. Under the influence of an external magnetic field $\vec{B}_0$ the energy levels for $m_\mathrm{S} = \pm 1$ will split up. For low magnetic fields, where we can assume the quantization axis to still lie along the NV^- center's axis, this additional splitting depends on the projection of $\vec{B}_0$ onto the NV^- center's axis and hence results in different shifts according to the NV^- center's four possible orientations within the diamond lattice.

In addition to these spin states which we subsume as the optical ground state $^3\mathrm{A}_2$, there exists an optically excited triplet state $^3\mathrm{E}$. Optical transitions between these states are spin conserving. However, a decay from the $^3\mathrm{E}$ to the $^3\mathrm{A}_2$ state is also possible through a non-radiative additional state $^1\mathrm{A}$ [148, 149]. This non-radiative decay is also called inter-system crossing (ISC) and is not spin conserving. It is this ISC which enables the optical and electrical readout of the NV^- center which we will discuss in the next section.

7.2 Spin-dependent photoionization

The spin-dependent photoionization cycle can be understood as two two-photon processes, whose spin dependence relies on the NV^-'s inter-system crossing (ISC) which is also key to the classic optical readout (figure 7.1 a) to e)) [143]. A first photon (green arrows) triggers shelving (black arrow) of NV^- centers in spin state $|2\rangle$ (corresponding to the $m_\mathrm{S} = \pm 1$ spin quantum numbers of NV^-) into the long-lived metastable singlet state $|5\rangle$ by this ISC. Since shelving protects this state from further laser excitation, absorption of a second photon preferentially ionizes NV^- centers prepared in spin state $|1\rangle$ (corresponding to $m_\mathrm{S} = 0$) into the conduction band (CB), creating a spin-dependent photocurrent (blue arrow) proportional to the population of the $m_\mathrm{S} = 0$ state. Microwave pulses (red arrow) increasing the $m_\mathrm{S} = \pm 1$ population will then lead to a resonant reduction of the photocurrent. Two further photons re-charge the NV^0 center

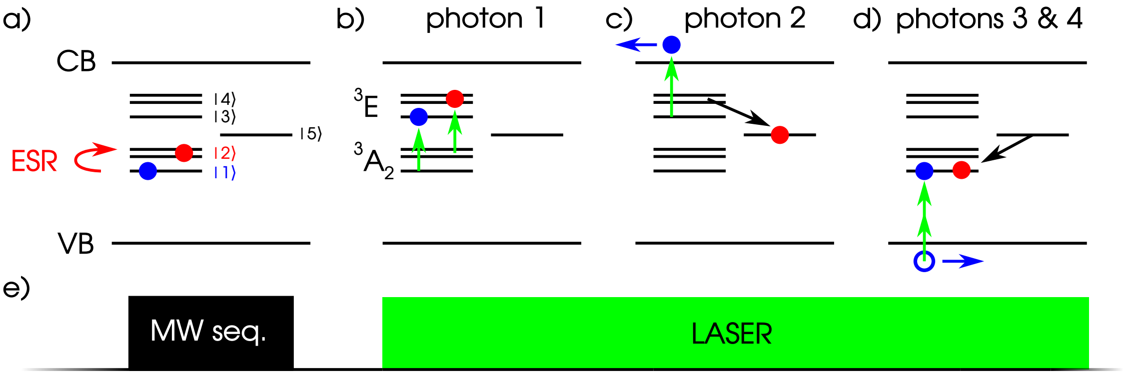

Figure 7.1: Spin-dependent photoionization of NV⁻ centers used for the electrical readout of its spin state. In panels a) to d) the horizontal black lines represent the NV⁻ center's states and the energy levels of the conduction (CB) and valence band (VB). The blue and red dots represent electrons (filled dots) and holes (empty dots). Transitions between energy levels are depicted by arrows. They are color-coded in green, red, blue and black for optical excitation, microwave excitation, drift in an electric field or non-radiative decay, respectively. e) Pulse sequence used for the spin-dependent photoionization. The microwave and light pulse are depicted by the black and green boxes, respectively. A microwave pulse switches the NV⁻ center from state |1⟩ to state |2⟩ or vice versa (panel a)). During the light pulse, a first photon excites the NV⁻ center from $^3A_2$ to ^3E (panel b)). A second incident photon ionizes the NV⁻ center if it has not decayed back to $^3A_2$ or into |5⟩ (panel c)). The spin-dependent readout is enabled by the fact that NV⁻ centers in state |4⟩ have a higher probability to decay into state |5⟩ than those in state |3⟩, which leads to a higher ionization probability for state |3⟩. After ionization, the NV^0 center is re-charged to the NV⁻ center by a two-photon process (panel d)).

into its negative charge state by excitation of the NV^0 (photon 3) and capture of an electron (photon 4) from the valence band (VB) [152]. For further discussion we will use the label $^3A_2$ for the optical ground state consisting of states |1⟩ and |2⟩ and ^3E for the optically excited states |3⟩ and |4⟩.

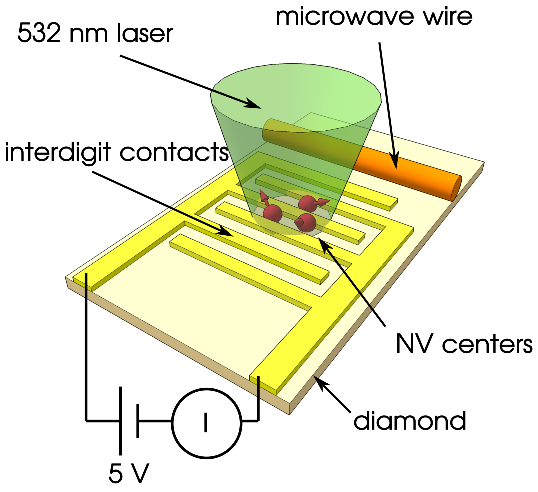

Figure 7.2: Schematic drawing of the sample and the measurement setup. A focused 532 nm laser photoionizes NV$^-$ centers inside of a N-doped diamond. To measure a current through the sample a bias voltage is applied to the Ti/Au interdigit contacts situated on top of the diamond. A nearby wire excites transitions between the NV$^-$ center's states if a resonant microwave current runs through the wire.

7.3 Sample geometry

Our spin readout experiments are performed in a photoconductor (figure 7.2). We illuminate a N-doped diamond (Element 6, grown by chemical vapor deposition, $[N] < 1$ ppm, $[NV] \approx 10$ ppb) with a green laser (wavelength 532 nm) pulse generated by a Nd:YAG laser and an acousto-optic modulator (AOM) and observe the resulting photocurrent between two interdigit Schottky contacts, biased with 5 V. The contacts (finger width 5 µm, finger-to-finger distance 10 µm) consist of a 10-nm-thick titanium and a 80-nm-thick gold layer, deposited on the diamond surface after cleaning it in a H_2SO_4/H_2O_2 mixture and an oxygen plasma treatment. The photocurrent through the sample is measured by using a transimpedance amplifier (amplification $1\,\mathrm{GVA}^{-1}$, bandwidth 10 Hz). Depending on the measurement we use a 5x, a 10x or a 100x objective, with numeric apertures of 0.15, 0.30 and 0.80 and diffraction limited NV$^-$ ensemble sizes of 100000, 6500 and 130, respectively. The microwave with frequency ν_{MW} is delivered to the sample using a wire next to the contacts.

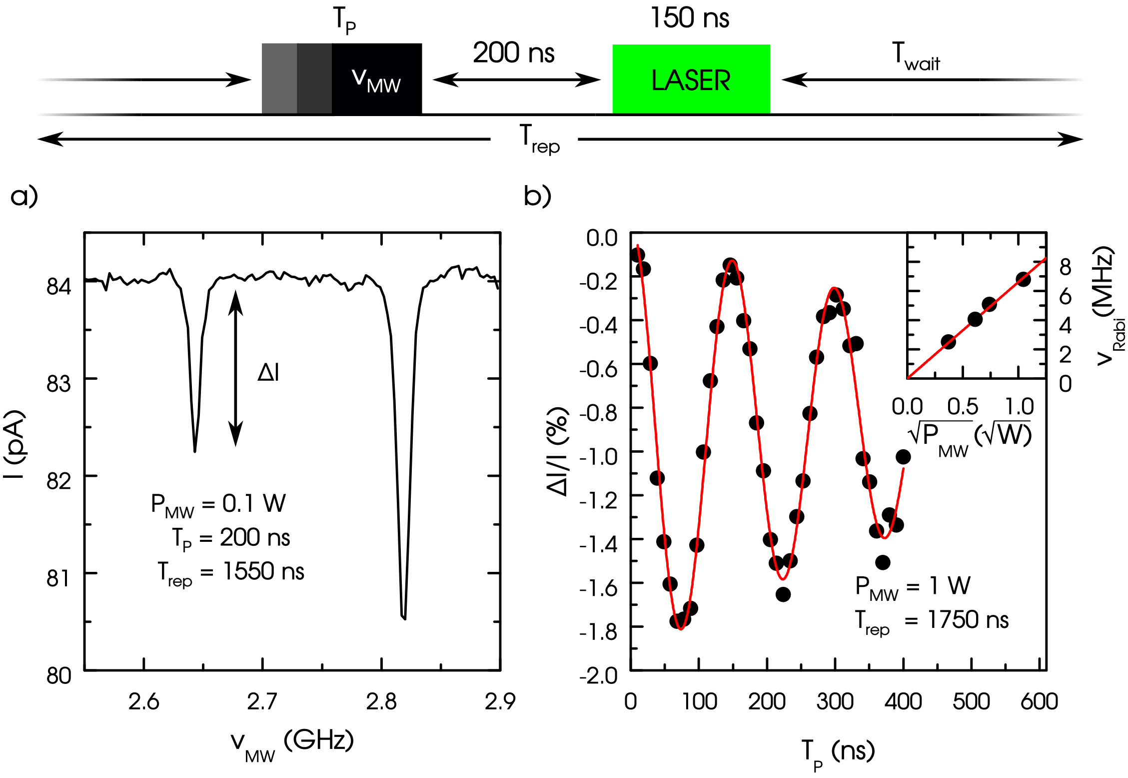

Figure 7.3: a) Pulsed electrically detected magnetic resonance spectrum for $B_0 \parallel \langle 111 \rangle$. b) Rabi oscillations in the contrast $\Delta I/I$ (symbols) with fit of an exponentially decaying cosine (line). The inset shows the frequency of Rabi oscillations (symbols) measured at different microwave powers and a linear fit (line). The pulse sequence used for the measurements is shown on top.

7.4 Pulsed EDMR experiments

We first demonstrate that coherent control can be detected electrically. To excite ESR transitions, the pulse sequence starts with a microwave pulse with power P_{MW} and varying duration T_{P} (top of figure 7.3 a) and b)). This initializes the spin of the NV$^-$ $^3A_2$ ground state. After a brief delay, an optical excitation pulse follows (10x objective, light power of 210 mW). Furthermore, an external magnetic field of $B_0 = 8.1\,\mathrm{mT}$ is applied to the sample parallel to one of the $\{1\,1\,1\}$ axes via a permanent magnet so that only one crystallographic NV$^-$ direction can be addressed.

Figure 7.3 a) shows the pEDMR spectrum obtained under these conditions, monitoring the DC current through the interdigit contact structure. In contrast to previous pEDMR experiments, where the spin dependence of comparatively slow recombination or hopping processes is monitored via a boxcar integration of the current transients [5, 9, 49, 155, 156] (c.f. chapter 2), the much faster pulse sequence repetition possible due to the fast photoionization and spin state initialization allows this vastly simpler approach. On a background photocurrent level of $I = 84\,\mathrm{pA}$ resonant decreases of the photocurrent are observed at $\upsilon_{\mathrm{MW}} = 2.643\,\mathrm{GHz}$ and $2.818\,\mathrm{GHz}$, corresponding to one $\{1\ 1\ 1\}$ orientation parallel to the B_0 field and three off-axis $\{1\ 1\ 1\}$ orientations, respectively. The resonant change of the current of $\Delta I = -1.5\,\mathrm{pA}$ at $2.643\,\mathrm{GHz}$ corresponds to a relative spin-dependent current change (contrast) of $\Delta I/I = -1.8\,\%$.

Rabi oscillations are observed in $\Delta I/I$ when the length T_{P} of the microwave pulse is changed, adjusting the waiting time T_{wait} to keep the repetition time T_{rep} constant (figure 7.3 b)). That Rabi oscillations are indeed obtained is demonstrated by the inset of figure 7.3 b), where the characteristic linear dependence of the oscillation frequency υ_{Rabi} on $\sqrt{P_{\mathrm{MW}}}$ and, therefore, on the microwave magnetic field B_1 is observed. The Rabi oscillations exhibit an effective dephasing time of 600 ns, in accordance with other results on diamond with natural isotope composition [157, 158]. In all experiments represented in figure 7.3 b) to d) $\Delta I/I$ was determined by cycling the microwave frequency between the resonant $\upsilon_{\mathrm{MW}} = 2.643\,\mathrm{GHz}$ and two non-resonant frequencies 2.61 GHz and 2.68 GHz [59].

The pulsed electrical detection scheme developed here allows to detect spin echoes, e.g. by using the pulse sequence depicted on top of figure 7.4 a) and b). As in the case of optically detected magnetic resonance (ODMR) [62, 63] and other pEDMR [47] experiments, the corresponding Hahn echo sequence needs to be extended by a final $\pi/2$-pulse, which projects the coherence echo to a polarization accessible to electrical readout.

Figure 7.4 a) shows the echo in $\Delta I/I$ as a function of the evolution time τ_2 for a fixed evolution time τ_1. At $\tau_1 = \tau_2$ the total microwave pulse applied equals a nutation of 2π, so that the contrast is minimal, in full agreement with figure 7.3 b). For τ_2 significantly smaller or longer than τ_1, no coherence echo is formed and the final $\pi/2$-projection pulse leads to an equal distribution of spin states which do or do not favor photoionization [47, 159]. Indeed, a maximum

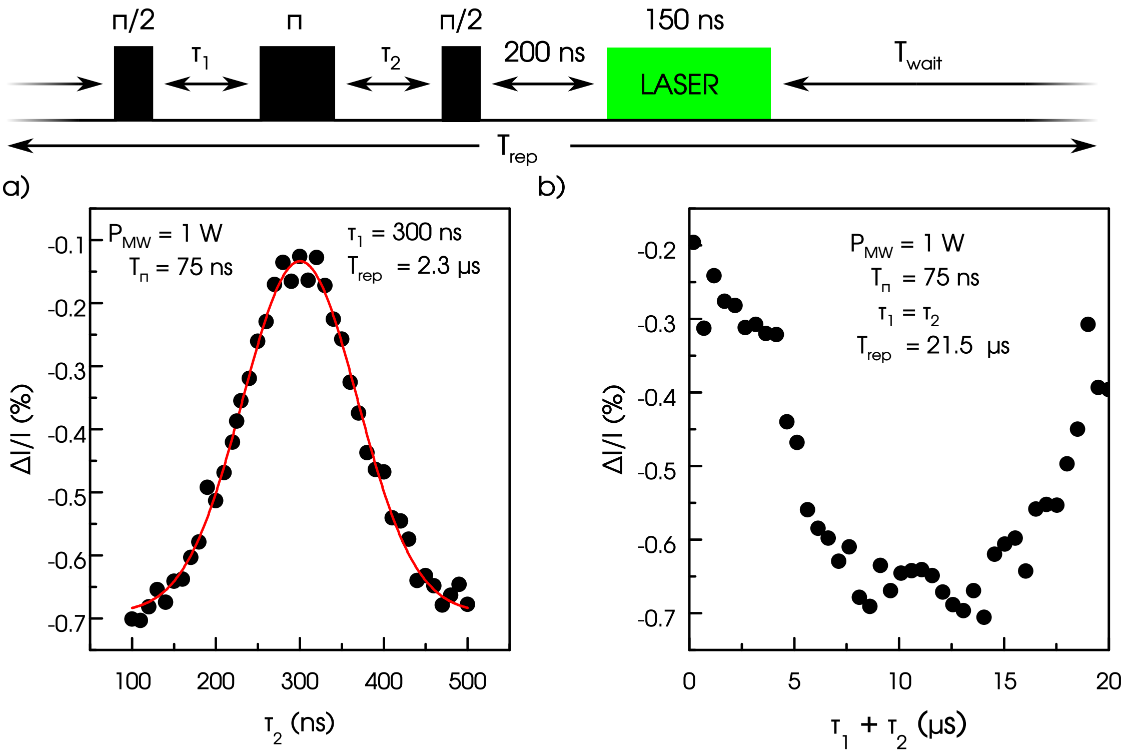

Figure 7.4: a) Spin echo measurement (symbols) with fit of a Gaussian (line). b) Echo decay measurement showing the first ESEEM oscillation. The pulse sequence used for the measurements is shown on top. T_π is the length of a π-pulse.

$\Delta I/I$ of $-0.7\,\%$ is observed for $\tau_1 \ll \tau_2$ or $\tau_1 \gg \tau_2$, in reasonable agreement with the contrast for π/2-pulses found in the Rabi oscillation experiment.

Finally, these echo experiments can also be performed as a function of total evolution time $\tau_1 + \tau_2$ with $\tau_1 = \tau_2$, giving access, e.g. to decoherence and to weak hyperfine interaction via electron spin echo envelope modulation (ESEEM). Figure 7.4 b) shows an echo decay experiment on the 2.643 GHz resonance where the oscillation is caused by ESEEM [65].

Summing up, the experiments shown in figure 7.3 and figure 7.4 clearly demonstrate that all fundamental coherent experiments can be performed on the NV$^-$ center with the electrical readout scheme developed here.

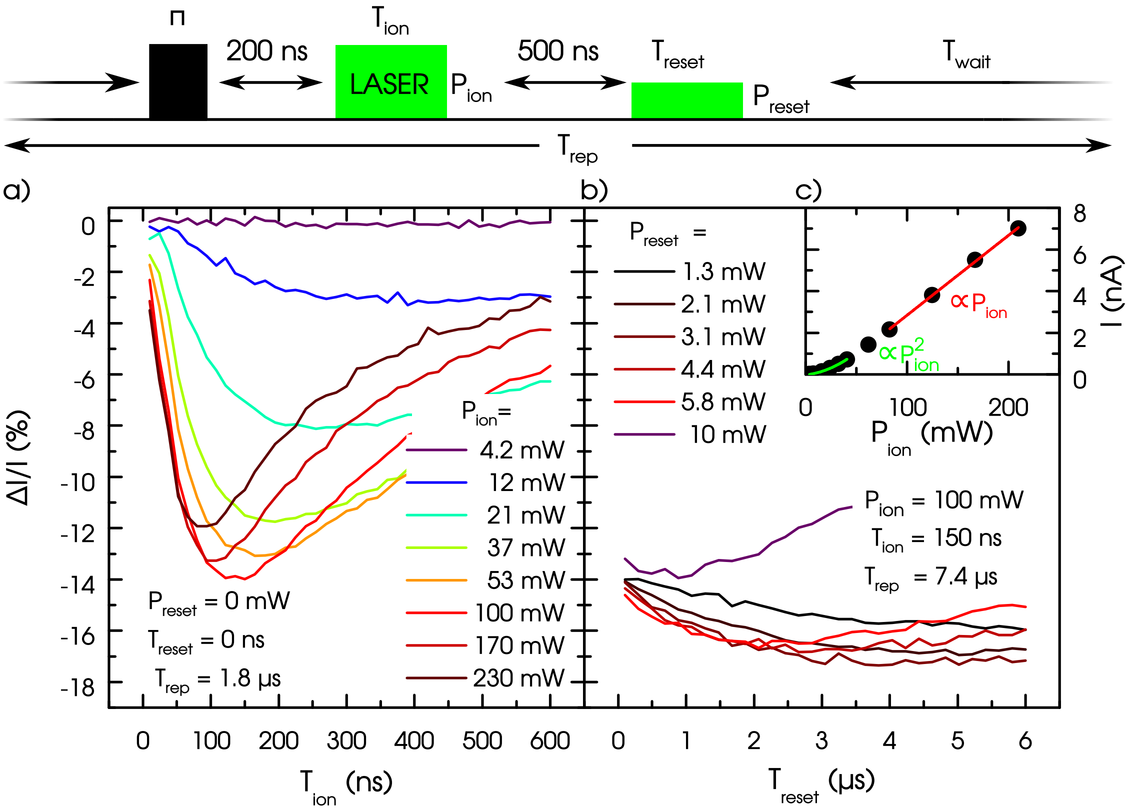

Figure 7.5: a) Contrast $\Delta I/I$ for a π-pulse as a function of the pulse length T_{ion} of the ionization pulse for different ionization pulse powers P_{ion}. b) $\Delta I/I$ as a function of the pulse length T_{reset} of an additional reset pulse for different reset pulse powers P_{reset}. The pulse sequence used is shown on top of the figure. c) Photocurrent through the sample as a function of the laser power. The green line is a fit of a polynomial of degree two, the red line is a fit of a linear function.

7.5 Pulse sequence optimization

We now turn to study the contrast that can be obtained by pulsed electric readout. We therefore place ourselves at $B_0 = 0$, where all four NV$^-$ orientations merge into a single resonance at $\upsilon_{\mathrm{MW}} = 2.87\,\mathrm{GHz}$, and where we can essentially flip NV$^-$ with all orientations into state $|2\rangle$ by a microwave π-pulse. Under these conditions we study the readout contrast as a function of both the duration T_{ion} and intensity P_{ion} of the readout light pulse (figure 7.5 top), keeping the illumination as homogeneous as possible by widening the laser beam with the 5x objective (figure 7.5 a)). For each power we find an optimum pulse length between a regime of too short pulses, where the ionization of NV⁻ mostly takes place on a timescale faster than the shelving process, and too long pulses, where mostly NV⁻ contribute to the current which have lost their spin information by a decay through the ISC or by a preceding ionization. Optimizing P_{ion} and T_{ion} for the sample studied, we reach an optimum contrast of $-14\,\%$ for $P_{\mathrm{ion}} = 100\,\mathrm{mW}$. As will be discussed below, this value is probably limited by ionization of background substitutional nitrogen donors $\mathrm{N_s^0}$ [143, 160].

The pulse powers and lengths optimal for readout may not be optimal for NV⁻ initialization and conversion of $\mathrm{NV^0}$ to NV⁻. Therefore in figure 7.5 b), we introduce a second laser pulse to separate the ionization process from the NV⁻ initialization. Here $\Delta I/I$ is plotted against the reset pulse length T_{reset} for different reset pulse powers P_{reset}. Small P_{reset} improve $\Delta I/I$ for increasing T_{reset}. The optimal $P_{\mathrm{reset}} = 3.1\,\mathrm{mW}$ leads to a maximal $\Delta I/I$ of $-17\,\%$ which is reached for $T_{\mathrm{reset}} \geq 3\,\mu\mathrm{s}$. For higher P_{reset} the reset pulse itself starts to ionize the NV⁻ centers, which decreases $\Delta I/I$.

7.6 Monte-Carlo simulation

We can quantitatively reproduce these observations by a Monte-Carlo model of the NV⁻ center's optical cycle together with photoionization and recharging of the $\mathrm{NV^0}$ (figure 7.6 a)) using the partial lifetimes of reference 161. The excitation time t from the $^3\mathrm{A}_2$ ground state of the NV⁻ to its $^3\mathrm{E}$ excited state, the characteristic time $a \cdot t$ of the ionization process and the lifetime of the ionized state $t_{\mathrm{NV^0}}$ are used as parameters in the simulation.

Following reference 162 the photocurrent through the diamond sample is $I = eGg$, with the elemental charge e, the charge carrier generation rate G and the photoconductive gain g. Since the charge carrier generation rate is not constant throughout the measurement, we replace G by its mean

$$\overline{G} = \frac{1}{T_{\mathrm{ion}}} \int_0^{T_{\mathrm{ion}}} G\,(t)\,\mathrm{d}t = \frac{N}{T_{\mathrm{ion}}}, \tag{7.2}$$

with N the number of charge carriers generated during T_{ion}. To account for a background current I_{b}, originating from the ionization of $\mathrm{N}_{\mathrm{s}}^{0}$, we add a generation of further electrons with a rate $G_{\mathrm{N}_{\mathrm{s}}^{0}} = b/t$. Microwave pulse imperfections yielding a mixture between $|1\rangle$ and $|2\rangle$ at the start of the experiment are described by a parameter p multiplied with the contrast curve. The contrast then becomes

$$\frac{\Delta I}{I} = p\frac{I_{|2\rangle} - I_{|1\rangle}}{I_{|1\rangle} + I_{\mathrm{b}}} = p\frac{\overline{G}_{|2\rangle} - \overline{G}_{|1\rangle}}{\overline{G}_{|1\rangle} + G_{\mathrm{N}_{\mathrm{s}}^{0}}} = p\frac{N_{|2\rangle} - N_{|1\rangle}}{N_{|1\rangle} + \frac{bT_{\mathrm{ion}}}{t}}, \tag{7.3}$$

where the subscripts $|1\rangle$ and $|2\rangle$ denote the value for the initial states $|1\rangle$ and $|2\rangle$, respectively.

The values for $N_{|1\rangle}$ and $N_{|2\rangle}$ are calculated by a Monte-Carlo simulation using the algorithm sketched in figure 7.6 b). At the start, the time t is set to zero and the state of the NV$^-$ is initialized either to $|1\rangle$ or $|2\rangle$. Then, we set the auxiliary variable Δt, which keeps track of the time until a transition happens, to zero and calculate a random number $r \in [0, 1)$. This number is compared with the probability p_{d} for a decay during the time of a simulation step t_{step}.

To find p_{d} we start with the definition of an exponential decay of a quantity M with the lifetime τ and the decay rate κ

$$\frac{\mathrm{d}M}{\mathrm{d}t} = -\kappa M = -\frac{1}{\tau}M, \tag{7.4}$$

which can be reordered to yield

$$\frac{-\mathrm{d}M}{M} = \frac{\mathrm{d}t}{\tau} = p_{\mathrm{d}}. \tag{7.5}$$

$\frac{-\mathrm{d}M}{M}$ can be interpreted as the ratio of centers, which decay in the time $\mathrm{d}t$, or the probability p_{d} for a single specimen to decay in $\mathrm{d}t$. Since the simulation progresses in discrete steps t_{step}, $\mathrm{d}t$ is replaced with t_{step} for all calculations. If $r > p_{\mathrm{d}}$, Δt is increased by t_{step} and a new random number r is generated. This process continues until $r \leq p_{\mathrm{d}}$, at which point a new state for the NV is chosen with the help of another random number $r \in [0, 1)$ according to the probability $p_{\mathrm{new\ state}}$ to end up in a specific decay channel from the current state. This probability is calculated by comparing the partial decay rate

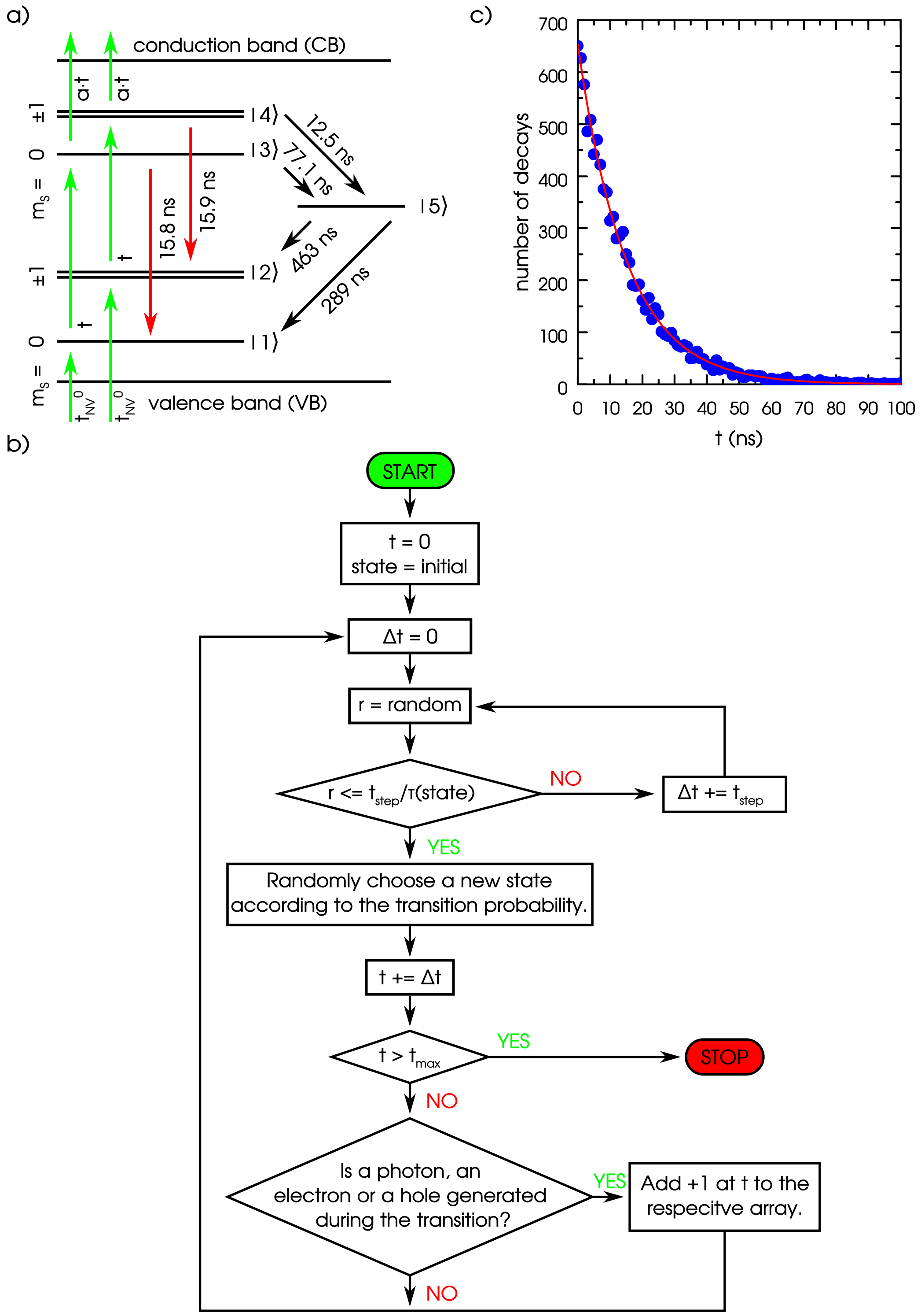

Figure 7.6: a) Level scheme and transition times [161] used for the Monte-Carlo simulation. b) Flow chart of the numerical simulation. c) Test of the Monte-Carlo simulation for a single decay channel with a decay constant of $\tau = 15\,\text{ns}$. The red curve is a fit of equation 7.8.

$\kappa_{\text{new state}}$ into this state with the total decay rate κ_{total}

$$p_{\text{new state}} = \frac{\kappa_{\text{new state}}}{\kappa_{\text{total}}}. \tag{7.6}$$

Afterwards, the time t is increased by Δt. If t is greater than the maximal runtime of the simulation t_{max}, the simulation ends. Otherwise, the simulation checks if the transition from the initial state to the new state excites a photon, electron or hole and adds one count in the respective photon, electron or hole array at the position t if applicable and jumps back to the instruction where Δt is set to zero. Since this is a statistical process, the simulation is repeated up to t_{max} several times. To find $N_{|i\rangle}$ we take the sum over the electron and hole arrays e_i and h_i corresponding to the initial state i according to

$$N_{|i\rangle}(t) = \sum_{j=0}^{t} \frac{1}{2} \left(e_i[j] + h_i[j]\right). \tag{7.7}$$

The factor $\frac{1}{2}$ accounts for the fact that blocking contacts will only generate a current corresponding to the elemental charge if an electron and a hole are generated and leave the device [162].

In order to verify this algorithm, we tested it on a decay of one species with only one decay channel and no excitation pathways. This should result in the well-known exponential decay. We chose a lifetime of $\tau = 15\,\text{ns}$ and the simulation was repeated 1000 times. Figure 7.6 c) plots the number of decays during one step t_{step} as a function of the time t. Since the number of decays is proportional to the amount of non-decayed centers, it should follow an exponential curve, too. The red line is a fit of

$$y(t) = A \cdot e^{-\frac{t}{\tau}} \tag{7.8}$$

to the simulation and yields $\tau = 14.9\,\text{ns}$, which is in very good agreement with the intended lifetime and therefore confirms the validity of the algorithm.

We now use this algorithm inside of a Nelder-Mead simplex fitting algorithm to fit the simulated contrast to the data presented in figure 7.5 for the three laser powers of 53 mW, 100 mW and 230 mW.

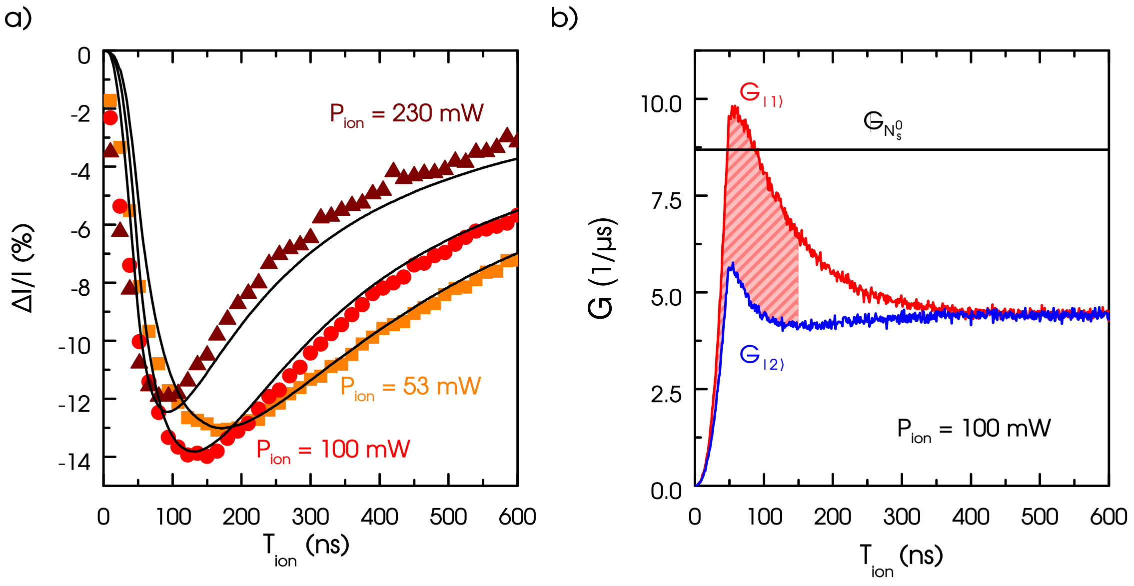

Figure 7.7: a) Contrast $\Delta I/I$ as a function of the length of the ionization pulse T_{ion} for three pulse powers taken from figure 7.5 and simultaneous fit of the Monte-Carlo simulation (black lines). b) Simulated charge carrier generation rates $G_{|1\rangle}$ and $G_{|2\rangle}$ plotted as a function of the time during the ionization pulse T_{ion} for the initial states $|1\rangle$ and $|2\rangle$, respectively. The black line depicts a constant background charge carrier generation rate $G_{\mathrm{N}_\mathrm{s}^0}$ originating from substitutional nitrogen donors.

Wherever possible, we use the lifetimes published by Robledo et al. [161] (c.f. figure 7.6a). This leaves us with the fit parameters a, b, p, t_{NV^0} and t_{fit} of which a, b, p and t_{NV^0} are used globally for all fits, while $t = t_{\mathrm{fit}} \cdot 100\,\mathrm{mW}/P_{\mathrm{ion}}$ is scaled according to the laser powers P_{ion}. The turn-on-time of the AOM is simulated by linearly increasing P_{ion} during the first 50 ns of the pulse. To keep the complexity of the simulation down we use only one t_{NV^0} for all three fits, which overestimates the generated photocurrent for small laser powers and vice versa.

Figure 7.7 a) compares $\Delta I/I$ and the fit of the Monte-Carlo simulation, which are in very good agreement. We find $t_{\mathrm{fit}} = 22\,\mathrm{ns}$, $a = 1.1$, $b = 0.19$, $p = 0.75$ and $t_{\mathrm{NV}^0} = 10\,\mathrm{ns}$. A t in the range of tens of ns is in agreement with the onset of a saturation in the cw photocurrent at $P_{\mathrm{ion}} = 100\,\mathrm{mW}$ (c.f. figure 7.5 c)) which we expect to happen at the point where the excitation time from $^3\mathrm{A}_2$ to $^3\mathrm{E}$ reaches the partial

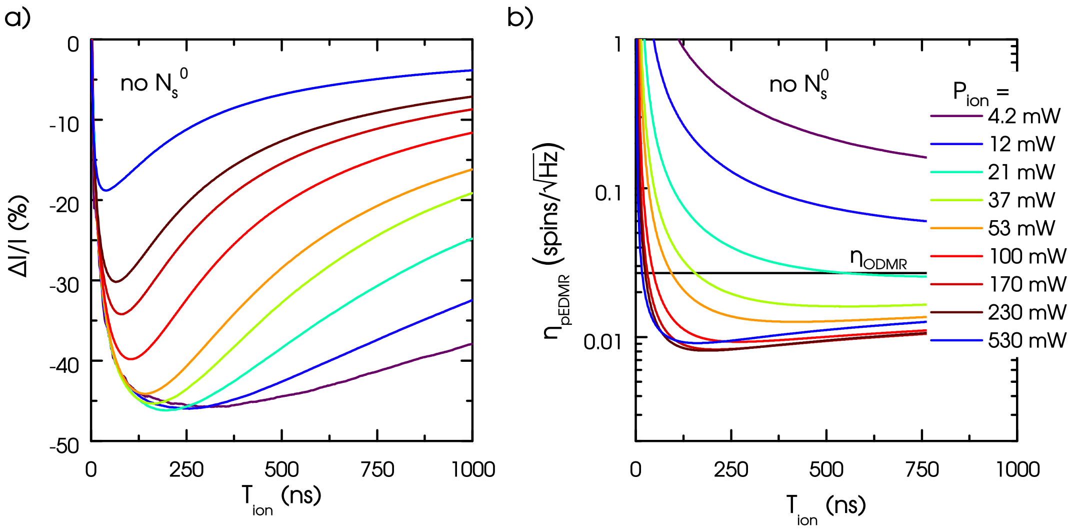

Figure 7.8: a) Simulated $\Delta I/I$ as function of T_{ion} for different P_{ion} under optimal conditions. b) Sensitivity η_{pEDMR} as a function of T_{ion} for different P_{ion} under optimal conditions. η_{ODMR} marks the typical ODMR sensitivity.

lifetime for the transition from ^{3}E to ^{3}A$_2$. $p < 1$ is probably caused by the limited pulse fidelity at $B_0 = 0$, since differently oriented NV$^-$ centers have different Rabi frequencies.

The model and the parameters determined allow us to simulate the charge carrier generation dynamics in our sample during a laser pulse. Figure 7.7 b) shows the charge carrier generation rate $G_{|1\rangle}(t)$ and $G_{|2\rangle}(t)$ for $P_{\mathrm{ion}} = 100\,\mathrm{mW}$. The horizontal line depicts a background current originating from $\mathrm{N_s^0}$ at $G_{\mathrm{N_s^0}} = 8.6\,\mu\mathrm{s}^{-1}$. For times longer than 400 ns all spin-dependent signal is lost and the system is in a steady state with $\widetilde{G}_{|1\rangle} = \widetilde{G}_{|2\rangle} = 4.5\,\mu\mathrm{s}^{-1}$, each at about 1/2 the charge carrier generation rate originating from $\mathrm{N_s^0}$. For $T_{\mathrm{ion}} = 150\,\mathrm{ns}$ we find $N_{|1\rangle} = 1.0$, $N_{|2\rangle} = 0.6$ and a $\mathrm{N_s^0}$ background of 1.3 by integration over the curves, again indicating that the contrast is limited by $\mathrm{N_s^0}$ ionization.

7.7 Possible sensitivity

In order to explore the sensitivity of the electrical detection of NV$^-$ we simulate $\Delta I/I$ without a background current I_b, with instantaneous AOM turn-on, and assuming a flawless pulse fidelity $p = 1$. Figure

7.8 a) plots $\Delta I/I$ simulated under these conditions versus T_{ion}. Again, $\Delta I/I$ has an optimal T_{ion} for each P_{ion}. The most notable difference is the maximal $\Delta I/I$ of $-46\,\%$ which is predicted for $P_{\mathrm{ion}} = 21\,\mathrm{mW}$.

However, we expect maximum sensitivity to be obtained for rather different optical pulse conditions. A sensitivity η is usually defined by

$$\eta = \frac{1}{\mathrm{SNR}} \cdot \frac{N}{\sqrt{\Delta f}}, \tag{7.9}$$

with the signal-to-noise ratio SNR, the number of spins N and the detection bandwidth Δf of the particular experiment [163]. For ODMR we find the SNR using Poissonian statistics, where the difference in photoluminescence (PL) counts $\Delta cts = cts_{|1\rangle} - cts_{|2\rangle}$ for the different initial states is divided by the shot noise generated by the number of counts $\sqrt{cts_{|1\rangle}}$ of the bright initial state $|1\rangle$. For pEDMR we use the difference in the current ΔI divided by the sum of the shot noise generated by the total current $\sqrt{2eI\Delta f}$ [164] and the amplifier input noise $\delta I_{\mathrm{amp}} \cdot \sqrt{\Delta f}$. Thus we find

$$\eta_{\mathrm{ODMR}} = \frac{\sqrt{N}}{c\sqrt{cts_{\mathrm{single}}\Delta f}} = \frac{\sqrt{N}}{c\sqrt{rate_{\mathrm{single}}}} \quad \text{and} \tag{7.10}$$

$$\eta_{\mathrm{pEDMR}} = \frac{\sqrt{2eI_{\mathrm{single}}N} + \delta I_{\mathrm{amp}}}{cI_{\mathrm{single}}}, \tag{7.11}$$

where the subscript single denotes the corresponding value for a single NV$^-$ center, c is the contrast of the respective measurement and $rate_{\mathrm{single}}$ is the effective count rate of the measurement.

Figure 7.8 b) plots the simulated sensitivity η_{pEDMR} at a sequence repetition rate of 500 kHz and for $\delta I_{\mathrm{amp}} = 0.2\,\mathrm{fA}\,\sqrt{\mathrm{Hz}}^{-1}$ versus T_{ion}. For each P_{ion} the sensitivity decreases (i.e. improves) with longer T_{ion} because of the increased I_{single} and c for longer T_{ion}. After reaching an optimal value η_{pEDMR} increases again since the decrease in c cancels the effects of the higher currents. The expected optimal sensitivity of 0.008 spins $\sqrt{\mathrm{Hz}}^{-1}$ for pEDMR is not reached for the P_{ion} corresponding to the maximum contrast but rather for $170\,\mathrm{mW} < P_{\mathrm{ion}} < 230\,\mathrm{mW}$ and $T_{\mathrm{ion}} \approx 200\,\mathrm{ns}$.

For comparison we estimate the sensitivity for a typical ODMR experiment on a single NV$^-$ center with a count rate of 100 kcts/s

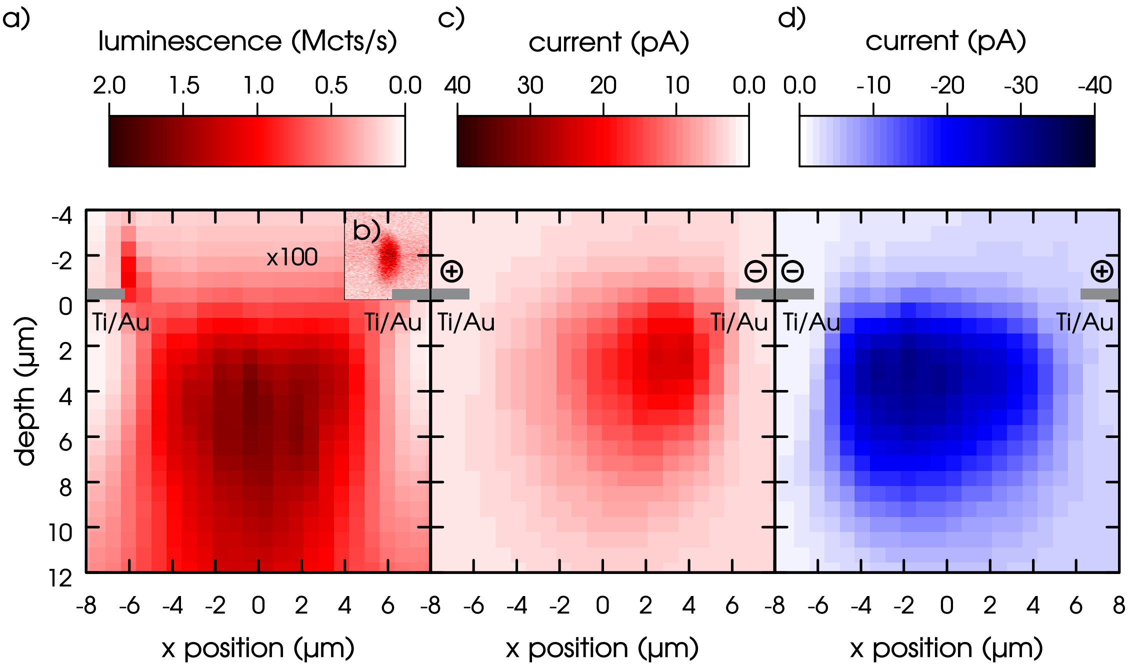

Figure 7.9: a) NV⁻ photoluminescence intensity map. b) Photoluminescence intensity map for a single NV⁻ using the same spatial dimensions as panel a) and multiplied by 100 to fit into the color coding of a). c) Current map for a bias voltage of 5 V. d) Current map for a bias voltage of −5 V. The position of the finger structure in a) and c) is depicted in gray.

and a contrast of 30 %. With a typical integration time over the fluorescence of 300 ns and a shot repetition time of 1 / (500 kHz) = 2000 ns, the effective count rate becomes 15 kcts/s. Therefore $\eta_{\mathrm{ODMR}} = 0.027\frac{\mathrm{spins}}{\sqrt{\mathrm{Hz}}}$, which is marked by the black horizontal line in figure 7.8 b). This value is a factor of 3 worse than the simulated sensitivity of the electrical detection. Hence, replacing the optical detection with electrical detection should not come at a reduced sensitivity.

7.8 Position-dependent current

Finally, to gain insight on the spatial origin of the photocurrent, simultaneous photoluminescence intensity and photocurrent measurements were performed. Figure 7.9 a) depicts the color-coded

NV^- photoluminescence intensity map of the diamond sample using a 100x objective and continuous illumination with a laser power of 1.2 mW (corresponding to 30 mW with the 5x objective). The approximate location of the contacts is indicated. A maximum PL intensity of 1.6 Mcts/s is observed. It originates from approximately 130 NV^- centers, as demonstrated via PL measurements on a single NV^- (confirmed via a Hanbury Brown-Twiss experiment) using the same optics and laser power which yields a count rate of 12 kcts/s as shown in the inset of figure 7.9 b).

Figure 7.9 c) shows the simultaneously measured photocurrent map. The generation of photocurrent in our metal-semiconductor-metal (MSM) photoconductor occurs only near to one contact and is limited to a depth of 10 µm below the sample. This limitation to ensembles which are at most 10 µm below the surface is probably caused by the distance between the electrodes of 10 µm, which leads to a nearly vanishing electric field 10 µm below the surface (simulation data not shown). The position dependence of the photocurrent along the lateral x-axis is caused by the MSM contacts in a similar way as in our position-dependent pEDMR experiments in section 6.5. Notably, the position of optimal photocurrent generation changes to the opposite metal contact when the bias voltage is reversed (c.f. figure 7.9 d)) as we would expect from the results in section 6.5.

We can use these measurements to put the sensitivity found in section 7.6 in absolute numbers: Using a 100x objective and $P_{\mathrm{ion}} = 1.2\,\mathrm{mW}$, a CW photocurrent of $I = 32\,\mathrm{pA}$ is generated in our sample. With our estimation of 130 NV^- in the focal volume, a single NV^- appears to generate a current of $I_{\mathrm{single}} = 240\,\mathrm{fA}$ under these illumination conditions. Simulations under the corresponding power of 30 mW for the 5x objective predict $I_{\mathrm{single}} = 580\,\mathrm{fA}$ so that the photoconductive gain in our samples is $g = 0.35 < 1$, as expected for a metal-semiconductor-metal photodetector. Under the optimized conditions given above ($P_{\mathrm{ion}} = 170\,\mathrm{mW}$, 5x objective, 500 kHz repetition rate, $g = 0.35$, $T_{\mathrm{ion}} = 200\,\mathrm{ns}$, $I_{\mathrm{b}} = 0$, $p = 1$), a single NV^- should exhibit a $\Delta I = 54\,\mathrm{fA}$ for $I_{\mathrm{single}} = 190\,\mathrm{fA}$, which should be easily measurable.

7.9 Summary and outlook

In summary, using a combination of pulsed photoionization and pulsed spin manipulation, we have demonstrated electrical readout of the coherent control of an ensemble of NV^- centers. With the help of a Monte-Carlo simulation we have improved our understanding of the photoionization dynamics and find that single-spin (multi-shot) detection should be feasible electrically, possibly with a higher sensitivity than optically. These results motivate a range of further studies, in particular into the relative benefits of photoconductors with ohmic or Schottky contacts and into more advanced photoionization schemes using different photon energies [154, 160, 165]. Furthermore, EDMR based on photoionization should be transferable to other defects and other host materials such as SiC [139–141], which might allow even easier integration of electrical spin readout, e.g. with bipolar device structures.

8

Summary

The main goal of this thesis was the examination of shaped pulses for pulsed electrically detected magnetic resonance. In order to achieve this goal a spectrometer capable of broadband shaped microwave (tested for frequencies ranging from 2 GHz to 18 GHz), radio frequency (tested around 4 MHz) and gradient pulse excitation (tested from DC to about 2 MHz) was built. To make full use of this setup broadband microwave structures were designed, which work very satisfactorily over at least this frequency range. Both the setup and the microwave structures were tested over their whole frequency range using shaped microwave pulses and show a good signal-to-noise ratio as well as high enough conversion factors so that all standard pEDMR experiments, including demanding ENDOR experiments, can easily be performed.

The functionality of adiabatic and optimal control pulses depends on their specific amplitude and phase functions during the pulse. To ensure that the shape of the pulse as seen by the spins is as intended, the setup was calibrated. This includes the characterization and elimination of IQ mixer imperfections as well as the determination of the system's nonlinearities mostly caused by the broadband amplifier. Due to the high conversion factor of our stripline antennas, we were able to reduce the microwave power of the pulses to about

100 mW, which lies well within the linear region of our 10 W amplifier. This allowed us to use linear system theory and measure the impulse response, which has a bandwidth of about 2 GHz. Since the pulses used in this work have at most a bandwidth of 100 MHz, the impulse response can be neglected, which simplifies the calculation of optimal control pulses.

With this knowledge, we implemented and compared adiabatic and optimal control pulses using pulse trains, which concatenate N universal rotation pulses. Depending on the B_1-inhomogeneity of the sample, a single adiabatic BIR-4 pulse improves the EDMR signal intensity of a π-pulse by a factor of up to 1.7 compared to a rectangular pulse. For samples with a high B_1-homogeneity improvements are found only for high rotation angles. Here, in pulse train experiments, adiabatic and optimal control pulses show EDMR signals for rotation angles of at least 16π, whereas the signal generated by rectangular pulses is completely gone after an 8π rotation. At these rotation angles, the optimal control pulses outperform the adiabatic pulses due to their shorter length by 29 % and 18 % for π/2- and π-pulses, respectively.

To evaluate the usefulness of adiabatic and optimal control pulses for pulse sequences, an echo sequence was implemented using those pulses. Due to its total sequence length, the adiabatic echo performs worse than the rectangular echo for experiments where a short echo is required, but has a 23 % higher amplitude in echo decay experiments. An echo sequence built from optimal control universal rotation pulses shows roughly the same improvement in decay experiments and is slightly better than rectangular pulses if a short echo is required due to the shorter length of the individual pulses compared to adiabatic ones. Using cooperatively optimized optimal control pulses, which allow to shorten the pulse lengths of each individual pulse in an echo sequence by at least a factor of two, we were able to improve the amplitude in decay experiments by 38 % with respect to the rectangular echo. For a sample with a higher B_1-inhomogeneity this value was increased to 50 %. To conclude, depending on the B_1-inhomogeneity of the samples, adiabatic and optimal control pulses can improve the signal by a factor of up to 1.7 in experiments with single pulses and also in more sophisticated sequences.

Taking into account the results of the antenna optimization and the successful implementation of adiabatic and optimal control pulses we modified our setup and microwave structures to enable magnetic resonance imaging. Using MRI, we determine the spatial origin of the pEDMR signal in the Au/Cr finger structures typically used in our experiments with a resolution of at least 1.5 µm. We use this information to identify the physical processes which contribute to the signal formation in the framework of a metal-semiconductor-metal structure and suggest improvements to the finger structure, which could increase the measured signal by a factor of two. For samples with finer details, our setup should be able to resolve features as small as 0.34 µm and promises resolutions of up to 0.5 Å for isotopically purified samples in combination with single-shot and single-spin EDMR detection via a single electron transistor.

In a short digression, the electrical spin readout of NV^- centers is demonstrated. Combining pulsed photoionization with a continuous current measurement we are able to detect coherent spin motions of ensemble sizes down to 130 NV^- centers. We optimized the parameters of the readout and simulated the NV^- center's dynamics during a light pulse with a Monte-Carlo simulation. These simulations suggest that the electrical detection should be able to read out a single NV^- center and even outperform the conventional optical detection, which makes it a suitable candidate for the use in NV^--center-based metrology applications where an optical readout using a confocal microscope is cumbersome.

Bibliography

[1] J. Schmidt and I. Solomon, Comptes rendus hebdomadaires des séances de L’Académie des Sciences **B263**, 169 (1966).

[2] H. Dersch, L. Schweitzer, and J. Stuke, Physical Review B **28**, 4678 (1983).

[3] F. Hoehne, H. Huebl, B. Galler, M. Stutzmann, and M. S. Brandt, Physical Review Letters **104**, 046402 (2010).

[4] A. Schnegg, J. Behrends, M. Fehr, and K. Lips, Physical Chemistry Chemical Physics **14**, 14418 (2012).

[5] F. Hoehne, L. Dreher, M. Suckert, D. P. Franke, M. Stutzmann, and M. S. Brandt, Physical Review B **88**, 155301 (2013).

[6] C. J. Cochrane and P. M. Lenahan, Applied Physics Letters **104**, 093503 (2014).

[7] H. Malissa, M. Kavand, D. P. Waters, K. J. v. Schooten, P. L. Burn, Z. V. Vardeny, B. Saam, J. M. Lupton, and C. Boehme, Science **345**, 1487 (2014).

[8] C. C. Lo, M. Urdampilleta, P. Ross, M. F. Gonzalez-Zalba, J. Mansir, S. A. Lyon, M. L. W. Thewalt, and J. J. L. Morton, Nature Materials **14**, 490 (2015).

[9] A. J. Kupijai, K. M. Behringer, F. G. Schaeble, N. E. Galfe, M. Corazza, S. A. Gevorgyan, F. C. Krebs, M. Stutzmann, and M. S. Brandt, Physical Review B **92**, 245203 (2015).

[10] D. R. McCamey, H. Huebl, M. S. Brandt, W. D. Hutchison, J. C. McCallum, R. G. Clark, and A. R. Hamilton, Applied Physics Letters **89**, 182115 (2006).

[11] J. T. Muhonen, J. P. Dehollain, A. Laucht, F. E. Hudson, R. Kalra, T. Sekiguchi, K. M. Itoh, D. N. Jamieson, J. C. McCallum, A. S. Dzurak, and A. Morello, Nature Nanotechnology **9**, 986 (2014).

[12] A. Stesmans and V. V. Afanasev, Journal of Applied Physics **83**, 2449 (1998).

[13] G. Feher, Physical Review **114**, 1219 (1959).

[14] L. H. W. v. Beveren, H. Huebl, D. R. McCamey, T. Duty, A. J. Ferguson, R. G. Clark, and M. S. Brandt, Applied Physics Letters **93**, 072102 (2008).

[15] L. Dreher, T. A. Hilker, A. Brandlmaier, S. T. B. Goennenwein, H. Huebl, M. Stutzmann, and M. S. Brandt, Physical Review Letters **106**, 037601 (2011).

[16] F. Klotz, H. Huebl, D. Heiss, K. Klein, J. J. Finley, and M. S. Brandt, Review of Scientific Instruments **82**, 074707 (2011).

[17] F. H. L. Koppens, C. Buizert, K. J. Tielrooij, I. T. Vink, K. C. Nowack, T. Meunier, L. P. Kouwenhoven, and L. M. K. Vandersypen, Nature **442**, 766 (2006).

[18] J. P. Dehollain, J. J. Pla, E. Siew, K. Y. Tan, A. S. Dzurak, and A. Morello, Nanotechnology **24**, 015202 (2013).

[19] M. R. Bendall and D. T. Pegg, Journal of Magnetic Resonance **67**, 376 (1986).

[20] K. Ugurbil, M. Garwood, and M. R. Bendall, Journal of Magnetic Resonance **72**, 177 (1987).

[21] M. Garwood, K. Ugurbil, A. R. Rath, M. R. Bendall, B. D. Ross, S. L. Mitchell, and H. Merkle, Magnetic Resonance in Medicine **9**, 25 (1989).

[22] R. S. Staewen, A. J. Johnson, B. D. Ross, T. Parrish, H. Merkle, and M. Garwood, Investigative Radiology **25**, 559 (1990).

[23] A. J. Sigillito, H. Malissa, A. M. Tyryshkin, H. Riemann, N. V. Abrosimov, P. Becker, H.-J. Pohl, M. L. W. Thewalt, K. M. Itoh, J. J. L. Morton, A. A. Houck, D. I. Schuster, and S. A. Lyon, Applied Physics Letters **104**, 222407 (2014).

[24] M. Suckert, *Studies on decoherence and recombination at the Si:P/SiO_2-Interface*, Diplomarbeit (Technische Universität München, 2011).

[25] T. E. Skinner, T. O. Reiss, B. Luy, N. Khaneja, and S. J. Glaser, Journal of Magnetic Resonance **163**, 8 (2003).

[26] T. E. Skinner, T. O. Reiss, B. Luy, N. Khaneja, and S. J. Glaser, Journal of Magnetic Resonance **167**, 68 (2004).

[27] N. Khaneja, T. Reiss, C. Kehlet, T. Schulte-Herbrüggen, and S. J. Glaser, Journal of Magnetic Resonance **172**, 296 (2005).

[28] K. Kobzar, B. Luy, N. Khaneja, and S. J. Glaser, Journal of Magnetic Resonance **173**, 229 (2005).

[29] B. Luy, K. Kobzar, T. E. Skinner, N. Khaneja, and S. J. Glaser, Journal of Magnetic Resonance **176**, 179 (2005).

[30] J. L. Neves, B. Heitmann, N. Khaneja, and S. J. Glaser, Journal of Magnetic Resonance **201**, 7 (2009).

[31] M. Braun and S. J. Glaser, Journal of Magnetic Resonance **207**, 114 (2010).

[32] M. A. Janich, R. F. Schulte, M. Schwaiger, and S. J. Glaser, Journal of Magnetic Resonance **213**, 126 (2011).

[33] T. E. Skinner, M. Braun, K. Woelk, N. I. Gershenzon, and S. J. Glaser, Journal of Magnetic Resonance **209**, 282 (2011).

[34] K. Kobzar, S. Ehni, T. E. Skinner, S. J. Glaser, and B. Luy, Journal of Magnetic Resonance **225**, 142 (2012).

[35] P. E. Spindler, Y. Zhang, B. Endeward, N. I. Gershernzon, T. E. Skinner, S. J. Glaser, and T. F. Prisner, Journal of Magnetic Resonance **218**, 49 (2012).

[36] T. Häberle, D. Schmid-Lorch, K. Karrai, F. Reinhard, and J. Wrachtrup, Physical Review Letters **111**, 170801 (2013).

[37] M. Braun and S. J. Glaser, New Journal of Physics **16**, 115002 (2014).

[38] J. Scheuer, X. Kong, R. S. Said, J. Chen, A. Kurz, L. Marseglia, J. Du, P. R. Hemmer, S. Montangero, T. Calarco, B. Naydenov, and F. Jelezko, New Journal of Physics **16**, 093022 (2014).

[39] F. Dolde, V. Bergholm, Y. Wang, I. Jakobi, B. Naydenov, S. Pezzagna, J. Meijer, F. Jelezko, P. Neumann, T. Schulte-Herbrüggen, J. Biamonte, and J. Wrachtrup, Nature Communications **5**, 3371 (2014).

[40] T. Nöbauer, A. Angerer, B. Bartels, M. Trupke, S. Rotter, J. Schmiedmayer, F. Mintert, and J. Majer, Physical Review Letters **115**, 190801 (2015).

[41] T. E. Skinner, N. I. Gershenzon, M. Nimbalkar, W. Bermel, B. Luy, and S. J. Glaser, Journal of Magnetic Resonance **216**, 78 (2012).

[42] C. Poole, *Electron spin resonance* (John Wiley & Sons, Hoboken, 1967).

[43] N. J. Stone, Atomic Data and Nuclear Data Tables **90**, 75 (2005).

[44] M. Steger, T. Sekiguchi, A. Yang, K. Saeedi, M. E. Hayden, M. L. W. Thewalt, K. M. Itoh, H. Riemann, N. V. Abrosimov, P. Becker, and H.-J. Pohl, Journal of Applied Physics **109**, 102411 (2011).

[45] M. Suckert, F. Hoehne, L. Dreher, M. Kuenzl, H. Huebl, M. Stutzmann, and M. S. Brandt, Molecular Physics **111**, 2690 (2013).

[46] E. B. Hale and R. L. Mieher, Physical Review **184**, 739 (1969).

[47] H. Huebl, F. Hoehne, B. Grolik, A. R. Stegner, M. Stutzmann, and M. S. Brandt, Physical Review Letters **100**, 177602 (2008).

[48] P. R. Cullis and J. R. Marko, Physical Review B **11**, 4184 (1975).

[49] C. Boehme and K. Lips, Physical Review B **68**, 245105 (2003).

[50] D. J. Griffiths, *Introduction to quantum mechanics* (Pearson Prentice Hall, Upper Saddle River, 2005).

[51] F. Bloch, Physical Review **70**, 460 (1946).

[52] M. A. Bernstein, K. F. King, and K. J. Zhou, *Handbook of MRI pulse sequences* (Elsevier Academic Press, London, 2004).

[53] W. B. Heard, *Rigid body mechanics: mathematics, physics and applications.* (WILEY-VCH, Weinheim, 2006).

[54] J. J. Henderson, C. M. Ramsey, H. M. Quddusi, and E. del Barco, Review of Scientific Instruments **79**, 074704 (2008).

[55] M. Mrazek, J. Mlynarczyk, D. S. Rudnicki, and W. Gawlik, Applied Physics Letters **107**, 013505 (2015).

[56] I. Kan, Y. Soeno, T. Roppongi, and Y. Nozaki, Applied Physics Letters **110**, 202404 (2017).

[57] F. Bloch and A. Siegert, Physical Review **57**, 522 (1940).

[58] J. Lu, F. Hoehne, A. R. Stegner, L. Dreher, M. Stutzmann, M. S. Brandt, and H. Huebl, Physical Review B **83**, 235201 (2011).

[59] F. Hoehne, L. Dreher, J. Behrends, M. Fehr, H. Huebl, K. Lips, A. Schnegg, M. Suckert, M. Stutzmann, and M. S. Brandt, Review of Scientific Instruments **83**, 043907 (2012).

[60] I. Katz, M. Fehr, A. Schnegg, K. Lips, and A. Blank, Journal of Magnetic Resonance **251**, 26 (2015).

[61] M. J. Duer, *Introduction to solid-state NMR spectroscopy* (Wiley-Blackwell, Oxford, 2004).

[62] W. G. Breiland, C. B. Harris, and A. Pines, Physical Review Letters **30**, 158 (1973).

[63] L. Childress, M. V. G. Dutt, J. M. Taylor, A. S. Zibrov, F. Jelezko, J. Wrachtrup, P. R. Hemmer, and M. D. Lukin, Science **314**, 281 (2006).

[64] E. L. Hahn, Physical Review **80**, 580 (1950).

[65] P. L. Stanwix, L. M. Pham, J. R. Maze, D. Le Sage, T. K. Yeung, P. Cappellaro, P. R. Hemmer, A. Yacoby, M. D. Lukin, and R. L. Walsworth, Physical Review B **82**, 201201 (2010).

[66] E. R. Davies, Physics Letters A **47**, 1 (1974).

[67] J. J. L. Morton, A. M. Tyryshkin, R. M. Brown, S. Shankar, B. W. Lovett, A. Ardavan, T. Schenkel, E. E. Haller, J. W. Ager, and S. A. Lyon, Nature **455**, 1085 (2008).

[68] P. C. Lauterbur, Nature **242**, 190 (1973).

[69] A. N. Garroway, P. K. Grannell, and P. Mansfield, Journal of Physics C: Solid State Physics **7**, L457 (1974).

[70] F. Schneider and G. R. Fink, eds., *Funktionelle MRT in psychiatrie und neurologie* (Springer, Berlin, 2007).

[71] V. Hombach, *Kardiovaskuläre magnetresonanztomographie* (Schattauer, Stuttgart, 2009).

[72] G. G. Maresch, M. Mehring, and S. Emid, Physica B+C **138**, 261 (1986).

[73] A. Blank, C. R. Dunnam, P. P. Borbat, and J. H. Freed, Journal of Magnetic Resonance **165**, 116 (2003).

[74] K. Arai, C. Belthangady, H. Zhang, N. Bar-Gill, S. J. DeVience, P. Cappellaro, A. Yacoby, and R. L. Walsworth, Nature Nanotechnology **10**, 859 (2015).

[75] A. Blank, G. Shapiro, R. Fischer, P. London, and D. Gershoni, Applied Physics Letters **106**, 034102 (2015).

[76] A. V. Oppenheim and R. W. Schafer, *Discrete-time signal processing* (Prentice Hall, Upper Saddle River, 1989).

[77] M. H. Levitt, Progress in Nuclear Magnetic Resonance Spectroscopy **18**, 61 (1986).

[78] M. Garwood and L. DelaBarre, Journal of Magnetic Resonance **153**, 155 (2001).

[79] K. Ugurbil, M. Garwood, A. R. Rath, and M. R. Bendall, Journal of Magnetic Resonance (1969) **78**, 472 (1988).

[80] A. P. Sage and C. C. White, *Optimum system control* (Prentice Hall, Englewood Cliffs, 1977).

[81] U. Madhow, *Fundamentals of Digital Communication* (Cambridge University Press, Cambridge, 2008).

[82] J. J. de Witt, *Modelling, estimation and compensation of imbalances in quadrature transceivers*, PhD thesis (Stellenbosch University, 2011).

[83] J. G. Baldwin and D. F. Dubbert, *Quadrature Mixer LO Leakage Suppression Through Quadrature DC Bias*, (Sandia National Labs., Albuquerque, NM, and Sandia National Labs., Livermore, CA, May 2002).

[84] T. Frey and M. Bossert, *Signal- und Systemtheorie* (Vieweg + Teubner Verlag, Wiesbaden, 2009).

[85] M. R. Schroeder, The Journal of the Acoustical Society of America **66**, 497 (1979).

[86] C. Dunn and M. J. Hawksford, Journal of the Audio Engineering Society **41**, 314 (1993).

[87] A. Farina, in Audio engineering society convention 108 (Feb. 2000).

[88] T. Kaufmann, T. J. Keller, J. M. Franck, R. P. Barnes, S. J. Glaser, J. M. Martinis, and S. Han, Journal of Magnetic Resonance **235**, 95 (2013).

[89] A. Farina, in Audio engineering society convention 122 (May 2007).

[90] D. D. Rife and J. Vanderkooy, Journal of the Audio Engineering Society **37**, 419 (1989).

[91] A. Doll and G. Jeschke, Journal of Magnetic Resonance **246**, 18 (2014).

[92] J. Arndt, *Matters Computational - Ideas, Algorithms, Source Code* (Springer, Berlin, 2011).

[93] U. Meyer-Baese, *Digital Signal Processing with Field Programmable Gate Arrays* (Springer, Berlin, 2007).

[94] M. Cohn and A. Lempel, IEEE Transactions on Information Theory **23**, 135 (1977).

[95] M. Baldi, F. Chiaraluce, N. Boujnah, and R. Garello, IEEE Transactions on Signal Processing **58**, 6284 (2010).

[96] F. M. Hrubesch, G. Braunbeck, A. Voss, M. Stutzmann, and M. S. Brandt, Journal of Magnetic Resonance **254**, 62 (2015).

[97] F. M. Hrubesch, *Breitbandige gepulste elektrisch detektierte magnetische resonanz*, Master's Thesis (Technische Universität München, 2012).

[98] A. Voss, *Spin-dependent recombination in arsenic-doped silicon*, Master's Thesis (Technische Universität München, 2014).

[99] D. G. Swanson, IEEE Microwave Magazine **2**, 72 (2001).

[100] S. Kim, S. Jeong, Y.-T. Lee, D. Kim, J.-S. Lim, K.-S. Seo, and S. Nam, Electronics Letters **38**, 622 (2002).

[101] J. Chammilliard, *On an electron spin resonance spectrometer for quantum information processing*, Master's Thesis (University of Waterloo, 2011).

[102] A. Doll, S. Pribitzer, R. Tschaggelar, and G. Jeschke, Journal of Magnetic Resonance **230**, 27 (2013).

[103] J. Kim and K. Konstantinou, Electronics Letters **37**, 1417 (2001).

[104] R. Raich, H. Qian, and G. T. Zhou, in IEEE International Conference on Acoustics, Speech, and Signal Processing, Vol. 6 (Apr. 2003).

[105] D. Morgan, Z. Ma, J. Kim, M. Zierdt, and J. Pastalan, IEEE Transactions on Signal Processing **54**, 3852 (2006).

[106] C. Bauer, R. Freeman, T. Frenkiel, J. Keeler, and A. J. Shaka, Journal of Magnetic Resonance **58**, 442 (1984).

[107] L. Dreher, F. Hoehne, M. Stutzmann, and M. S. Brandt, Physical Review Letters **108**, 027602 (2012).

[108] F. Hoehne, L. Dreher, D. P. Franke, M. Stutzmann, L. S. Vlasenko, K. M. Itoh, and M. S. Brandt, Physical Review Letters **114**, 117602 (2015).

[109] P. E. Spindler, S. J. Glaser, T. E. Skinner, and T. F. Prisner, Angewandte Chemie International Edition **52**, 3425 (2013).

[110] A. Doll, M. Qi, S. Pribitzer, N. Wili, M. Yulikov, A. Godt, and G. Jeschke, Physical Chemistry Chemical Physics **17**, 7334 (2015).

[111] P. Schöps, P. E. Spindler, A. Marko, and T. F. Prisner, Journal of Magnetic Resonance **250**, 55 (2015).

[112] G. Jeschke, S. Pribitzer, and A. Doll, The Journal of Physical Chemistry B **119**, 13570 (2015).

[113] T. F. Segawa, A. Doll, S. Pribitzer, and G. Jeschke, The Journal of Chemical Physics **143**, 044201 (2015).

[114] C. F. Young, E. H. Poindexter, G. J. Gerardi, W. L. Warren, and D. J. Keeble, Physical Review B **55**, 16245 (1997).

[115] D. Jérome and J. Winter, Phys. Rev. **134**, A1001 (1964).

[116] H. Morishita, E. Abe, W. Akhtar, L. S. Vlasenko, A. Fujimoto, K. Sawano, Y. Shiraki, L. Dreher, H. Riemann, N. V. Abrosimov, P. Becker, H.-J. Pohl, M. L. W. Thewalt, M. S. Brandt, and K. M. Itoh, Applied Physics Express **4**, 021302 (2011).

[117] L. J. Stelzer, *Broadband electrically detected magnetic resonance using optimal control*, Master's Thesis (Technische Universität München, 2017).

[118] K. Klein, B. Hauer, B. Stoib, M. Trautwein, S. Matich, H. Huebl, O. Astakhov, F. Finger, R. Bittl, M. Stutzmann, and M. S. Brandt, Review of Scientific Instruments **84**, 103911 (2013).

[119] K. Klein, *The EDMR microscope: combining conductive atomic force microscopy with electrically detected magnetic resonance*, PhD thesis (Technische Universität München, 2014).

[120] A. Payne, K. Ambal, C. Boehme, and C. C. Williams, Physical Review B **91**, 195433 (2015).

[121] K. Ambal, P. Rahe, A. Payne, J. Slinkman, C. C. Williams, and C. Boehme, Scientific Reports **6**, 18531 (2016).

[122] L. Shtirberg, Y. Twig, E. Dikarov, R. Halevy, M. Levit, and A. Blank, Review of Scientific Instruments **82**, 043708 (2011).

[123] K. Sekihara, M. Kuroda, and H. Kohno, Physics in Medicine and Biology **29**, 15 (1984).

[124] S. J. Simeth, *EDMR microscopy with pulsed field gradients*, Master's Thesis (Technische Universität München, 2017).

[125] R. N. Simons, *Coplanar waveguide circuits, components, and systems* (John Wiley & Sons, Hoboken, 2001).

[126] S. M. Sze and K. K. Ng, *Physics of semiconductor devices*, Third Edition (John Wiley & Sons, Hoboken, 2007).

[127] S. M. Sze, D. J. Coleman, and A. Loya, Solid-State Electronics **14**, 1209 (1971).

[128] P. Horowitz and W. Hill, *The art of electronics* (Cambridge University Press, Cambridge, 2015).

[129] A. Morello, J. J. Pla, F. A. Zwanenburg, K. W. Chan, K. Y. Tan, H. Huebl, M. Möttönen, C. D. Nugroho, C. Yang, J. A. van Donkelaar, A. D. C. Alves, D. N. Jamieson, C. C. Escott, L. C. L. Hollenberg, R. G. Clark, and A. S. Dzurak, Nature **467**, 687 (2010).

[130] *Microposit s1800 series photoresists.*

[131] N. Bar-Gill, L. M. Pham, A. Jarmola, D. Budker, and R. L. Walsworth, Nature Communications **4**, 1743 (2013).

[132] A. Gruber, A. Dräbenstedt, C. Tietz, L. Fleury, J. Wrachtrup, and C. v. Borczyskowski, Science **276**, 2012 (1997).

[133] J. M. Taylor, P. Cappellaro, L. Childress, L. Jiang, D. Budker, P. R. Hemmer, A. Yacoby, R. Walsworth, and M. D. Lukin, Nature Physics **4**, 810 (2008).

[134] T. Wolf, P. Neumann, K. Nakamura, H. Sumiya, T. Ohshima, J. Isoya, and J. Wrachtrup, Physical Review X **5**, 041001 (2015).

[135] V. M. Acosta, E. Bauch, M. P. Ledbetter, A. Waxman, L.-S. Bouchard, and D. Budker, Physical Review Letters **104**, 070801 (2010).

[136] P. Maletinsky, S. S. Hong, M. Grinolds, B. Hausmann, M. D. Lukin, R. L. Walsworth, M. Loncar, and A. Yacoby, Nature Nanotechnology **7**, 320 (2012).

[137] F. Shi, Q. Zhang, P. Wang, H. Sun, J. Wang, X. Rong, M. Chen, C. Ju, F. Reinhard, H. Chen, J. Wrachtrup, J. Wang, and J. Du, Science **347**, 1135 (2015).

[138] V. R. Manfrinato, L. Zhang, D. Su, H. Duan, R. G. Hobbs, E. A. Stach, and K. K. Berggren, Nano Letters **13**, 1555 (2013).

[139] N. R. Jungwirth, Y. Y. Pai, H. S. Chang, E. R. MacQuarrie, K. X. Nguyen, and G. D. Fuchs, Journal of Applied Physics **116**, 043509 (2014).

[140] D. J. Christle, A. L. Falk, P. Andrich, P. V. Klimov, J. U. Hassan, N. T. Son, E. Janzén, T. Ohshima, and D. D. Awschalom, Nature Materials **14**, 160 (2015).

[141] M. Widmann, S.-Y. Lee, T. Rendler, N. T. Son, H. Fedder, S. Paik, L.-P. Yang, N. Zhao, S. Yang, I. Booker, A. Denisenko, M. Jamali, S. A. Momenzadeh, I. Gerhardt, T. Ohshima, A. Gali, E. Janzén, and J. Wrachtrup, Nature Materials **14**, 164 (2015).

[142] A. Brenneis, L. Gaudreau, M. Seifert, H. Karl, M. S. Brandt, H. Huebl, J. A. Garrido, F. H. L. Koppens, and A. W. Holleitner, Nature Nanotechnology **10**, 135 (2015).

[143] E. Bourgeois, A. Jarmola, P. Siyushev, M. Gulka, J. Hruby, F. Jelezko, D. Budker, and M. Nesladek, Nature Communications **6**, 8577 (2015).

[144] F. M. Hrubesch, G. Braunbeck, M. Stutzmann, F. Reinhard, and M. S. Brandt, Physical Review Letters **118**, 037601 (2017).

[145] G. Davies and M. F. Hamer, Proceedings of the Royal Society of London A **348**, 285 (1976).

[146] J. H. N. Loubser and J. A. v. Wyk, Reports on Progress in Physics **41**, 1201 (1978).

[147] S. Felton, A. M. Edmonds, M. E. Newton, P. M. Martineau, D. Fisher, and D. J. Twitchen, Physical Review B **77**, 081201 (2008).

[148] A. Lenef and S. C. Rand, Physical Review B **53**, 13441 (1996).

[149] N. B. Manson, J. P. Harrison, and M. J. Sellars, Physical Review B **74**, 104303 (2006).

[150] L. Rondin, G. Dantelle, A. Slablab, F. Grosshans, F. Treussart, P. Bergonzo, S. Perruchas, T. Gacoin, M. Chaigneau, H.-C. Chang, V. Jacques, and J.-F. Roch, Physical Review B **82**, 115449 (2010).

[151] M. V. Hauf, B. Grotz, B. Naydenov, M. Dankerl, S. Pezzagna, J. Meijer, F. Jelezko, J. Wrachtrup, M. Stutzmann, F. Reinhard, and J. A. Garrido, Physical Review B **83**, 081304 (2011).

[152] P. Siyushev, H. Pinto, M. Vörös, A. Gali, F. Jelezko, and J. Wrachtrup, Physical Review Letters **110**, 167402 (2013).

[153] N. Aslam, G. Waldherr, P. Neumann, F. Jelezko, and J. Wrachtrup, New Journal of Physics **15**, 013064 (2013).

[154] B. J. Shields, Q. P. Unterreithmeier, N. P. de Leon, H. Park, and M. D. Lukin, Physical Review Letters **114**, 136402 (2015).

[155] A. R. Stegner, C. Boehme, H. Huebl, M. Stutzmann, K. Lips, and M. S. Brandt, Nature Physics **2**, 835 (2006).

[156] W. Harneit, C. Boehme, S. Schaefer, K. Huebener, K. Fostiropoulos, and K. Lips, Physical Review Letters **98**, 216601 (2007).

[157] A. J. Parker, H.-J. Wang, Y. Li, A. Pines, and J. P. King, arXiv:1506.05484 (2015).

[158] N. Mizuochi, P. Neumann, F. Rempp, J. Beck, V. Jacques, P. Siyushev, K. Nakamura, D. J. Twitchen, H. Watanabe, S. Yamasaki, F. Jelezko, and J. Wrachtrup, Physical Review B **80**, 041201 (2009).

[159] D. P. Franke, F. Hoehne, L. S. Vlasenko, K. M. Itoh, and M. S. Brandt, Physical Review B **89**, 195207 (2014).

[160] E. Bourgeois, E. Londero, K. Buczak, J. Hruby, M. Gulka, Y. Balasubramaniam, G. Wachter, J. Stursa, K. Dobes, F. Aumayr, M. Trupke, A. Gali, and M. Nesladek, Physical Review B **95**, 041402 (2017).

[161] L. Robledo, H. Bernien, T. v. d. Sar, and R. Hanson, New Journal of Physics **13**, 025013 (2011).

[162] A. Rose, *Concepts in photoconductivity and allied problems* (Interscience Publishers, New York, 1963).

[163] G. Boero, M. Bouterfas, C. Massin, F. Vincent, P.-A. Besse, R. S. Popovic, and A. Schweiger, Review of Scientific Instruments **74**, 4794 (2003).

[164] R. Müller, *Rauschen* (Springer, Berlin, 1990).

[165] D. A. Hopper, R. R. Grote, A. L. Exarhos, and L. C. Bassett, Physical Review B **94**, 241201 (2016).

[166] D. P. Franke, F. M. Hrubesch, M. Künzl, H.-W. Becker, K. M. Itoh, M. Stutzmann, F. Hoehne, L. Dreher, and M. S. Brandt, Physical Review Letters **115**, 057601 (2015).

[167] D. P. Franke, M. Szech, F. M. Hrubesch, H. Riemann, N. V. Abrosimov, P. Becker, H.-J. Pohl, K. M. Itoh, M. L. W. Thewalt, and M. S. Brandt, Physical Review B **94**, 235201 (2016).

[168] R. Schönmann, *Broadband microwave antennae for magnetic resonance*, Bachelor's Thesis (Technische Universität München, 2013).

[169] G. Braunbeck, *Shaped microwave pulses for broadband electrically detected magnetic resonance*, Master's Thesis (Technische Universität München, 2015).

[170] M. Künzl, *Nuclear quadrupole interaction in arsenic-doped silicon*, Master's Thesis (Technische Universität München, 2013).

[171] L. J. Stelzer, *Spin-dependent recombination in amorphous silicon*, Bachelor's Thesis (Technische Universität München, 2015).

[172] F. N. Hartz, *Electrical readout of NV^- centers in diamond*, Master's Thesis (Technische Universität München, 2017).

Danksagung

Am Schluss dieser Arbeit möchte ich mich bei all denen bedanken, die zu deren Gelingen beigetragen haben:

- Meinen Bachelor-, Werk- und Masterstudenten **Markus Künzel**, **Andrej Voss**, **Rudolf Schönman**, **Georg Braunbeck**, **Sebastian Simeth**, **Felix Hartz** und **Lukas Stelzer** für die großartige Zusammenarbeit und den Spaß im Labor.

- **Martin Brandt** für die Betreuung meiner Dissertation und das sorgfältige Korrekturlesen.

- **Wolfgang Kallies** für das Rechnen der hier verwendeten oc Pulse und den fruchtbaren Austausch bei deren Optimierung für unser System.

- **Lukas Dreher** für die Betreuung in meiner Diplomarbeit und die Mitwirkung bei den Messungen an den ionisierten Donatoren.

- **Felix Höhne** für die Hilfe bei meinen ersten ENDOR-Messungen.

- **Steffen Glaser** für die Diskussionen rund um die Themenbereiche der optimalen Reglung und des Pulsdesigns.

- **Friedemann Reinhardt**, **Georg Braunbeck** und **Alexander Kleinkauf** für die großzügige Bereitstellung ihres Messaufbaus, die Kooperation bei den Messungen und bei der Auswertung der Experimente zur elektrischen Auslese des Spinzustands von Stickstoff-Fehlstellen-Komplexen in Diamant.

- **Martin Stutzmann** für die Diskussionen zu Metall-Halbleiter-Metall-Strukturen.
- Den technischen Mitarbeitern **Michi Fischer**, **Claudia Paulus**, **Hubert Riedl**, **Wolfgang Bendak** und **Bernhard Kratzer** sowie dem Team der Feinmechanik und der Zentralwerkstatt für ihre Ratschläge und Mitarbeit bei allen (prozess-)technischen Dingen.
- **Ralf Meyer**, **Linda Mora** und **Anna Köninger** für die Tips und Tricks bei der Einführung des BCB-Prozesses.
- **Joana Figueiredo** für die immer freundliche Hilfe bei allen verwaltungstechnischen Fragen.
- Meinen Kollegen im Büro **Andreas Reitinger**, **Andreas Zeidler**, **Benno Blaschke**, **Roberta Caterino** und **Réka Csiki** für die tolle Stimmung.
- Meinen Mitdoktoranden in der Gruppe **Anton Greppmaier**, **Alexander Kupijai**, **Benedikt Stoib**, **David Franke**, **Konrad Klein**, **Max Suckert** und **Patrick Altmann** sowie allen anderen Doktoranden im WSI für die kollegiale Atmosphäre.
- Meiner Mutter **Kriemhilde Kilian** für die Unterstützung während des Studiums und das Korrekturlesen dieser Arbeit.
- **Ines Alker** für ihre Liebe und die Nachsicht während der Fertigstellung meiner Dissertation.

Besonderer Dank gebürt der DFG, die diese Arbeit finanziell im Rahmen des Schwerpunktprogramms 1601 (Grant No. BR 1585/8-2), der Forschergruppe 1493 (Grant No. STU 139/11-2), des Sonderforschungsbereichs 631 (project C3) und des Emmy Noether Grants No. RE 3606/1-1 unterstützt hat.

Publications

Articles published in the framework of this thesis

- F. M. Hrubesch, G. Braunbeck, A. Voss, M. Stutzmann, and M. S. Brandt, Journal of Magnetic Resonance **254**, 62 (2015)
- F. M. Hrubesch, G. Braunbeck, M. Stutzmann, F. Reinhard, and M. S. Brandt, Physical Review Letters **118**, 037601 (2017)

Other articles

- D. P. Franke, F. M. Hrubesch, M. Künzl, H.-W. Becker, K. M. Itoh, M. Stutzmann, F. Hoehne, L. Dreher, and M. S. Brandt, Physical Review Letters **115**, 057601 (2015)
- D. P. Franke, M. Szech, F. M. Hrubesch, H. Riemann, N. V. Abrosimov, P. Becker, H.-J. Pohl, K. M. Itoh, M. L. W. Thewalt, and M. S. Brandt, Physical Review B **94**, 235201 (2016)

Supervised Bachelor's and Master's theses which contributed to this thesis

- R. Schönmann, *Broadband microwave antennae for magnetic resonance*, Bachelor's Thesis (Technische Universität München, 2013)
- A. Voss, *Spin-dependent recombination in arsenic-doped silicon*, Master's Thesis (Technische Universität München, 2014)

- G. Braunbeck, *Shaped microwave pulses for broadband electrically detected magnetic resonance*, Master's Thesis (Technische Universität München, 2015)
- S. J. Simeth, *EDMR microscopy with pulsed field gradients*, Master's Thesis (Technische Universität München, 2017)
- L. J. Stelzer, *Broadband electrically detected magnetic resonance using optimal control*, Master's Thesis (Technische Universität München, 2017)

Other supervised Bachelor's and Master's theses

- M. Künzl, *Nuclear quadrupole interaction in arsenic-doped silicon*, Master's Thesis (Technische Universität München, 2013)
- L. J. Stelzer, *Spin-dependent recombination in amorphous silicon*, Bachelor's Thesis (Technische Universität München, 2015)
- F. N. Hartz, *Electrical readout of NV^- centers in diamond*, Master's Thesis (Technische Universität München, 2017)